Experimentelle Physik

Calibration and Alignment of ALICE TRD Super Modules Using Cosmic Ray Data

Diplomarbeit

von

Henriette Gatz

Westfälische Wilhelms-Universität Münster
Institut für Kernphysik

— September 2010 —

Contents

Introduction

One of the largest man-built machines, the Large Hadron Collider (LHC) at CERN[1], created a large interest by the media when resuming operation in November 2009. The particle accelerator is designed to collide pairs of ions from protons up to heavy nuclei, e.g. lead ions. It thereby intends to look into the origin and properties of matter.
Under normal conditions, the constituents of nuclear matter, which are quarks and gluons, only occur in bound states, the hadrons. Nevertheless, they are expected to become deconfined under high temperature, as shortly after the big bang, or pressure, as in the core of neutron stars. Thereby, they enter a state called Quark-Gluon Plasma (QGP). One of the experiments installed at the LHC is ALICE ("A Large Ion Collider Experiment"). Its purpose is the investigation of this state of matter.
ALICE consists of several detectors, one of them being the Transition Radiation Detector (TRD). One of the main tasks of the TRD is the discrimination of electrons and pions. For this, a combination of calculations based on the particles energy loss and transition radiation measurements is used. A precise knowledge about the gas gain is obligatory. Moreover, the TRD serves as tracking device, which requires a good position resolution. This resolution is influenced by various parameters, which are used during the conversion of detector signals into spatial positions. These parameters are, for example, the drift velocity and the positions of detector components. The deviations of ideal and actual positions are derived by an alignment procedure.
The TRD is comprised of 18 super modules, which undergo final assembly at the institute of nuclear physics in Münster. As part of this, a first alignment and calibration of the previously mentioned parameters can be carried out by use of cosmic-ray data. For this purpose programs provided by the official AliRoot framework can be used. As this being the main part of this thesis, an overall calibration and alignment procedure for data recorded in Münster was set up. This calibration and alignment data serves as a starting point for calibration at CERN. It provides reconstructed data, for subsequent analyses. The procedure can now be used for all super modules, which are about to be assembled. Moreover, the procedure was performed for four super modules, which have been already

[1] CERN is the European Organization for Nuclear Research.

shipped to CERN.

The following chapter gives a short overview of the theoretical background of high energy physics. Chapter 2 outlines the different experiments at the LHC, as well as the detectors which comprise ALICE. The construction and functionality of the ALICE TRD are presented in Chapter 3. In the fourth chapter, the setup for the recording of cosmic ray data in Münster is explained. The topics of Chapter 5 are the methods used for the alignment and calibration procedure. Chapter 6 explains how the calibration and alignment procedure can be executed. The final results of the calibrations of four super modules are presented in Chapter 7.

1. Theoretical Background

1.1 The Standard Model of Particle Physics

The Standard Model of particle physics is a theory that describes properties and interactions of all currently known particles.

1.1.1 Elementary Particles and their Fundamental Interactions

A particle is called elementary if it has no further substructure. Currently, twelve elementary particles are known, they will be discussed in detail below. The elementary particles are grouped pair wise into families. For each particle exists a corresponding antiparticle, which carries the same mass and spin as the particle, but opposite additive quantum numbers.
Apart from gravitation three fundamental interactions, which take place between elementary particles, are known: the electromagnetic, the strong, and the weak interaction. The fundamental forces are mediated by the exchange of gauge bosons between the particles (see Table 1.1).
The fundamental forces couple to associated charges, which are the electromagnetic charge for the electromagnetic force, the weak isospin for the weak interaction, and the color charge for the strong interaction.

Forces	Relative Strength	Gauge Bosons	Acts on
Strong Force	1	Gluons	Quarks, Gluons
Electromagnetic Force	1/137	Photons	All Charged Particles
Weak Force	10^{-7}	$W^{\pm}$, Z^0	Quarks, Leptons

Table 1.1: *Overview of the fundamental forces and their gauge bosons [Per00].*

Quarks and leptons are fermions (carry half-integer spin) and therefore obey the Pauli principle. This implies that two identical elementary particles can never occupy the same quantum state.
The color charge carrying elementary particles are called quarks (q) and their antiparticles antiquarks ($\overline{q}$), respectively. They are classified by the so-called flavor quantum number in three different generations that consist of two different quarks each: up (u) and down (d), charm (c) and strange (s), top (t) and bottom (b). Since all of them carry electric

charge and weak isospin, they all, in addition to the strong interaction, interact electromagnetically and weakly. The mass of the quarks varies between a few MeV/c^2 and several GeV/c^2 (see Table 1.2).
The fact, that no free quarks have been observed to date leads to the postulate that quarks only form color neutral objects. This means, the additive color mixture of the quarks consists of either a color and its anticolor, or three different colors respectively anticolors. These color neutral objects are called hadrons and are either mesons, consisting of a quark and an antiquark, or (anti-)baryons, consisting of three different (anti-)quarks. The strong interaction is mediated by gluons. The different types of gluons are distinguished by the color charge they carry, which consists of color and anticolor. Thereby eight[1] different gluons exist. The gluons couple to color charge, thus they interact with quarks as well as with other gluons. This influence of the strong interaction on its own gauge bosons leads to the short range which usually lies within the size of a hadron (fm), but can be larger. The strong dependence of the potential V on the distance r between two quarks can be parameterized with Equation 1.1:

$$V(r) = -\frac{4}{3}\frac{\alpha_s}{r} + kr. \tag{1.1}$$

The factor $\frac{4}{3}$ comes from the three possible quark colors. As a result of the interaction between gluons, the field between two quarks has the shape of a string, with k representing the string tension. α_s denotes the strong coupling constant, which depends on the momentum transfer Q^2:

$$\alpha_\mathrm{s}(Q^2) = \frac{12\pi}{(32 - 2n_\mathrm{f}) \cdot \ln \frac{Q^2}{\Lambda^2}}. \tag{1.2}$$

In this equation n_f indicates the number of involved quark flavors. The scale parameter Λ can be determined experimentally by a fit to $\alpha_\mathrm{s}(Q^2)$. According to Equation 1.2, the coupling constant rises with decreasing momentum transfer, leading to a strong coupling of the quarks. Therefore, they do not occur as free particles, a phenomenon called confinement. Due to the presence of the strong interaction, particles like protons and neutrons are formed.
The six elementary particles that do not carry color charge are called leptons. They are also classified in three generations of two components each: the electron (e^-) and the electron neutrino (ν_e), the muon (μ) and the the muon neutrino (ν_μ), the tau (τ) and the tau neutrino (ν_τ). All six interact weakly. Except for the neutrinos, which do not carry electric charge, they also interact electromagnetically. The mass of the leptons varies over a large range (see Table 1.2).

The electromagnetic interaction is mediated via photons (γ). A photon can couple to all charged particles and binds the electrons with the atomic nuclei inside an atom. Since

[1] Mathematically nine different gluons exist, but one is colorless, hence does not exist.

	Quarks			Leptons		
Generation	Name	Charge	Mass	Name	Charge	Mass
1	up	2/3 e	1.5 - 3.3 MeV/c^2	e^-	-e	0.511 MeV/c^2
	down	-1/3 e	3.5 - 6 MeV/c^2	ν_e	0	$\leq$ 2 eV/c^2
2	charm	2/3 e	1.16 - 1.34 GeV/c^2	μ	-e	105 MeV/c^2
	strange	-1/3 e	70 - 130 MeV/c^2	ν_μ	0	$\leq$ 0.19 MeV/c^2
3	top	2/3 e	171.3 $\pm$ 3.2 GeV/c^2	τ	-e	1776 MeV/c^2
	bottom	-1/3 e	4.13 - 4.37 GeV/c^2	ν_τ	0	$\leq$ 18.2 MeV/c^2

Table 1.2: *Overview of the elementary particles, their charges and masses [A+09].*

photons have no charge, do not interact with each other, and also have zero rest mass, the range of the electromagnetic force is infinite.
The massive gauge bosons $W^\pm$ and Z^0 mediate the weak interaction. This leads to the force's short range of about 1 fm. The weak interaction is, beside the gravitation, the only force that couples to neutrinos. It also is the only force capable of flavor changing, which can be seen for example in the β-decay in which a d quark is transformed into a u quark [WW07].

1.2 The Quark-Gluon Plasma

As mentioned above, quarks do not appear as free particles, but are bound inside hadrons. The more the quarks of a hadron are separated from one another, the stronger they are pulled towards each other by the strong nuclear force. This phenomenon is called confinement. When force is applied to a hadron, this energy is stored in a field between the quarks of the hadrons. In case a sufficient force is applied, a part of this stored energy forms new quarks between the previous existing quarks. This procedure, in which new hadrons instead of free quarks are created, is called fragmentation.
Nevertheless, lattice **Q**uantum **C**hromo**D**ynamics (lattice QCD)[2] predicts a phase transition of nuclear matter at high temperatures and/or high baryon densities. The quarks and gluons can become deconfined and enter the state of quark-gluon plasma.
A medium with high temperatures and low density is expected to undergo a crossover transition. Different lattice QCD calculations exist. In the approach of Fodor and Katz a critical point for increasing baryon density and decreasing temperature is determined [FK04].

[2]Lattice **Q**uantum **C**hromo**D**ynamics (lattice QCD) is a theory which allows to numerically solve the equations of the strong interaction on a lattice of points in space and time.

At densities below this point, a phase transition might occur, in which hadrons and deconfined quarks coexist. At densities above the critical point, the transition is of first order. This means, the energy density exhibits a discontinuity due to the fact that the system absorbs energy without an increase of temperature. The phase diagram in Figure 1.1 shows these transitions.

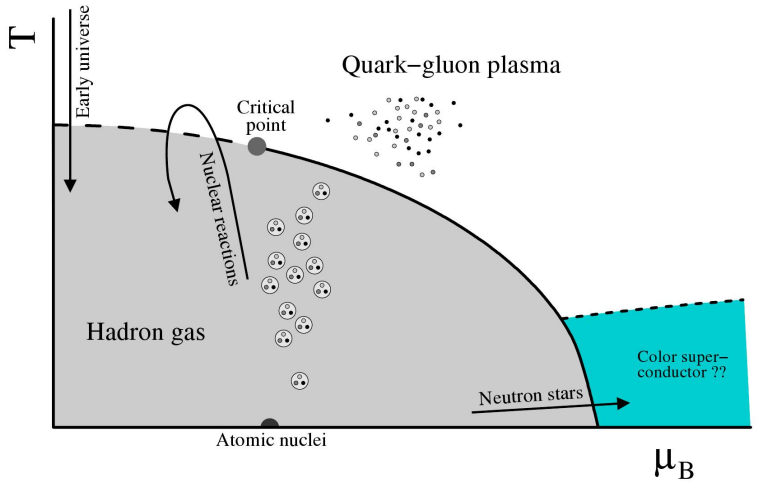

Figure 1.1: *Phase diagram of strongly interacting matter depicting the temperature T and the baryochemical potential μ_B. The baryochemical potential is a measure for the net baryon density which is the difference between baryon and anti-baryon number of a system. A phase transition of first order (solid line), crossover phase transition (dashed line at low baryon density), and phase transition which might appear into a color superconducting phase (dashed line at higher baryon densities) are displayed [KB04].*

It is presumed that a QGP has existed shortly after the big bang. It is also expected to be created in heavy ion collisions with a center of mass energy for each nucleon-nucleon pair of $\sqrt{s_{NN}} \geq 10$ GeV.

1.2.1 Generating a Quark-Gluon Plasma in the Laboratory

Experimentally, one tries to create a quark-gluon plasma via ultra-relativistic heavy ion collisions.
Figure 1.2 shows such a collision of two gold nuclei moving at nearly the speed of light. In the middle of Figure 1.2 partons[3], which are created during the primary collision, are shown. A high pressure gradient is built up and causes an expansion of the system which subsequently cools down. After a certain temperature is reached, a phase transition from

[3]Parton is a generic term for quarks and gluons.

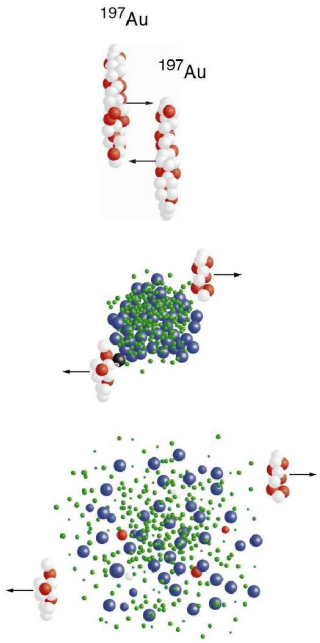

Figure 1.2: *Ultra-relativistic heavy ion collision of two gold nuclei. Due to Lorentz contraction the nuclei appear as thin discs in the lab frame. Top: nuclei approaching each other. Middle: spectators (white and red) leave the reaction zone unmodified, whereas the participants produce partons (blue and green). Bottom: hadronization is reached and new hadrons are created [rhi09].*

QGP to a hot hadron gas takes place. During this so-called hadronization, hadrons are formed again. Thereby, the total energy of the partons will be converted into the newly created hadrons and their kinetic energy.
Figure 1.3 depicts a schema of the space-time evolution after such an ultra-relativistic heavy ion collision. The origin of this graph indicates the nucleon's initial interaction. As explained above, the created medium, which is shown inside the light-cone around the t-axis, will expand. In case the energy and density produced in the collision is high enough, a short-lived fireball in pre-equilibrium phase will be created. In subsequent collisions between the partons in the medium, the system gets thermalized and a QGP is created. Subsequently two stages of freeze-out will take place. First the chemical freeze-out occurs, which fixes the compositions of the hadrons. Thereafter, no inelastic scattering will occur. After that the thermal freeze-out will take place, where, due to the small density of the system, the hadrons do not interact with each other by elastic collisions anymore. Free streaming hadrons are left behind.
Experiments which contribute currently to the study of a possible QGP are located at the **R**elativistic **H**eavy **I**on **C**ollider (RHIC) at the **B**rookhaven **N**ational **L**aboratory (BNL).

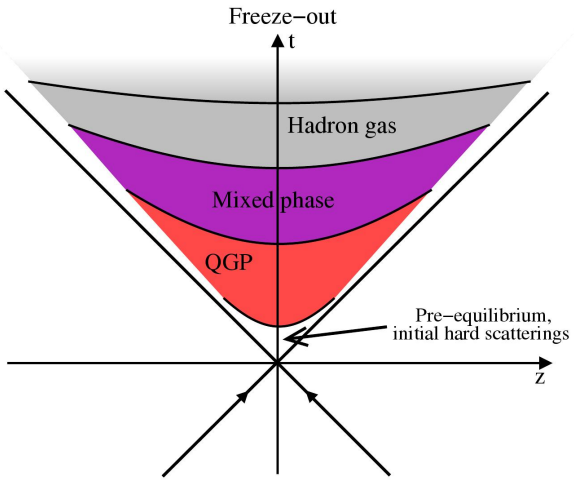

Figure 1.3: *Schema of a space(z)-time(t) evolution of a nucleus-nucleus collision [KB04].*

In the near future, the **L**arge **H**adron **C**ollider (LHC) at CERN will enter the quest for a QGP.

1.2.2 Signatures of the Quark-Gluon Plasma

The quark-gluon plasma cannot be detected directly, as there is no un-ambiguous observable known. The difficulties to identify if a QGP was created during the collision or not, originate from the fact that evidence for its existence has to be found in the final hadronic state, after hadronization. Only the combination of several signatures points to the creation of a QGP.

J/Ψ Suppression and Enhancement

The J/Ψ particle consists of a charm and an anti-charm quark. The mass of c quarks is around 1.5 GeV. Therefore, they can only be produced in the hard parton interactions during the early stage of the collision. This makes heavy quarks a very interesting observable to study the evolution of the heavy ion collision and the properties of the fireball.
During a heavy ion collision, pairs of charm and anti-charm quarks are produced. In the QGP phase, these c and $\overline{c}$ quarks are screened by the color charge of the surrounding medium and cannot form a bound state, e.g. a J/Ψ particle. During hadronization the c and $\overline{c}$ quarks form either a bound $c\overline{c}$ state or combine with the more abundant light quarks.
In heavy ion collisions, more c and $\overline{c}$ quarks are produced compared to proton-proton (p-p) collisions. In order to compare p-p and heavy ion collisions, the number of produced J/Ψ in p-p collisions are scaled with the number of nucleus-nucleus collisions within the heavy

ion collision. At the **S**uper **P**roton **S**ynchrotron (SPS) at the European Organization for Nuclear Research (CERN) it was found, that the production of J/Ψ is suppressed compared to scaled p-p collisions. This suppression has been suggested as one of the signatures for the creation of the QGP. As mentioned above, the c and $\overline{c}$ quarks, that could form a bound state, are screened during the QGP phase. At hadronization, those c and $\overline{c}$ quarks are more likely to form D mesons[4] with any other two quarks. At p-p collisions, the produced c and $\overline{c}$ quarks are not screened and have a higher chance to form a J/Ψ. Therefore, even though more c an $\overline{c}$ quarks are produced during the heavy ion collisions at RHIC, less J/Ψ were created compared to scaled p-p collisions. A supression of the J/Ψ production did occur.

At the LHC, higher collision energy than at RHIC will be reached. Hence, more c and $\overline{c}$ quarks will be produced. The charm quarks will again be screened by the medium during the QGP phase. Nevertheless, as many of the charm quarks will be present, the chance of them to find a second charm quark and form a J/Ψ should be higher than in a p-p collision. This can lead to a more numerous production of J/Ψ compared to scaled p-p collisions, the J/Ψ production would be enhanced [SPR90], [BMS07], [Tan09]. Figure 1.4 gives a schematic overview of these two scenarios.

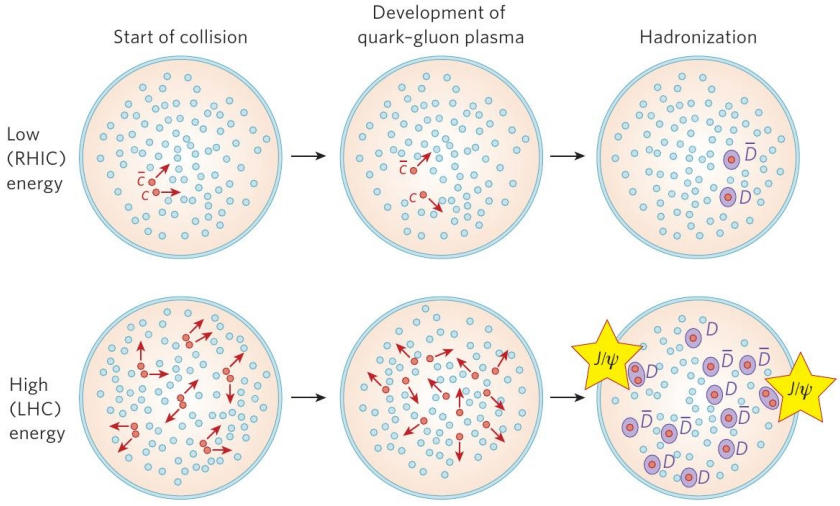

Figure 1.4: *Schema of heavy ion collisions at different energies leading to a QGP followed by hadronization. Light partons produced during the interaction are indicated by blue dots, the produced c and $\overline{c}$ by red dots. Top panel: Low collision energies; the few c and $\overline{c}$ build D mesons with any other two quarks (u, d, s), resulting in a suppressed production of J/Ψ. Bottom panel: High collision energies; the numerous production of c and $\overline{c}$ leads to an enhanced production of J/Ψ [BMS07].*

[4] A D meson is meson which contains two quarks, one of them being either a charm or an anti-charm quark.

Direct Photons

Photons which are created during the collision, and not originate from decays, are called direct photons. Contrary to quarks or hadrons, photons do not interact strongly and may escape the collision region without further interaction. Therefore, they carry unaltered information about the medium, which makes them an interesting observable.
Direct photons can be subdivided into prompt and thermal photons. Prompt photons are emitted in inital hard scatterings. Thermal photons are emitted during the equilibrium phase. In the measured photon spectra, prompt photons dominate the high p_{T} region, whereas thermal photons are more abundant at lower p_{T} [ALI04], [van09].

Jet Quenching

During the early stage of a heavy ion collision, high p_{T} partons are created in primary parton-parton collisions. These new partons fragment into hadrons during hadronization. Thus, the parton's energy is converted into new particles and their kinetic energy. These particles are emitted in a narrow cone, the so-called jet. The larger the overall energy of the parton, the more hadrons are produced during fragmentation.
Partons produced during the collision have a momentum leading them away from the reaction vertex. Thus, they traverse the created medium. In case a QGP is created, the medium has a high temperature and energy density. This leads to a certain probability of parton-parton interactions between the created partons and the medium. These interactions result in an energy loss of the partons, compared to a scenario of partons at high p_{T} without the presence of a hot and dense matter. This would lead to a supprssion of high p_{T} hadrons, as it was observed at RHIC. Moreover, the jet structure is modified. The occurrence of those two behaviors is called jet quenching. The observation of jet quenching and a modification of jets in general can be used to study the properties of the medium.
When studying the modifications of jet properties, it is important to map out the depencence on the path length. This behavior is depicted in Figure 1.5. Here, the parton which created the upper jet has not interacted with the medium before fragmentation. The parton which fragmented into the lower jet has lost some of its energy in the medium, hence its jet is quenched [d'E09], [Lac09].

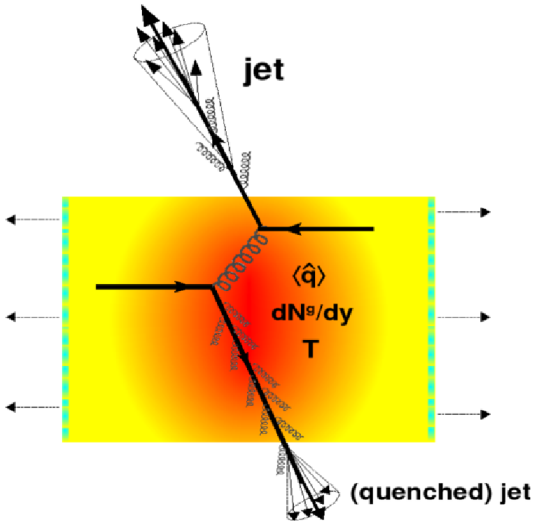

Figure 1.5: *Illustration of jet quenching in dependence of the distance traversed in the medium.* $\langle \hat{q} \rangle$ *represents the mediums transport coefficient, which is dependent on the particle multiplicity* dN^g/dy *and the temperature* T *[d'E09].*

2. Experimental Setup

2.1 The Large Hadron Collider - LHC

The **L**arge **H**adron **Co**llider (LHC) is a circular hadron accelerator located at the European Organization for Nuclear Research (CERN) near Geneva. Its purpose is to look into some of the most fundamental questions of physics, such as the study of the hypothesized Higgs boson[1] and the examination of the quark-gluon plasma.
With a circumference of nearly 27 km, the LHC is the world's largest and highest-energy particle accelerator. It is installed in an underground tunnel that crosses the Franco-Swiss border. In two beam pipes, protons, or ions up to lead, are circulated in opposite directions. They can be collided at four interaction points where the two pipes intersect. The design value of the luminosity is 10^{27} $cm^{-2}s^{-1}$ with a center of mass energy of 1150 TeV (5.5 TeV per nucleon pair) for collisions of lead ions and 10^{34} $cm^{-2}s^{-1}$ at 14 TeV per proton pair. The final kinetic energy reached by protons is 7 TeV at a velocity 0.999999991% of the speed of light.
To keep the particles in a circular motion, 9539 superconducting magnets are used: 1232 dipole magnets with a length of 15 m, 392 quadrupole magnets with a length of about 3 m, and 6000 correction magnets. A magnetic field of 8.3 T is created by a current of 11700 A, while operating the magnets with superfluid helium at 1.9 K.
As the LHC is operated as synchrotron, it can not continuously accelerate particles. Therefore, they are accelerated in groups of the so-called bunches. The LHC has 3500 possible bunch positions, however 2800 bunches, each consisting of about 10^{11} protons, will circulate at most. The minimum distance between those bunches is 7 m at full luminosity. About 20 *p-p* collisions take place at a single bunch crossing. This results in about $3{\cdot}10^7$ crossings per second on average, with a rate of nearly $6{\cdot}10^8$ particle collisions per second [CER08].

2.1.1 Experiments at the LHC

At the LHC six experiments are installed at four intersection points:
The four main experiments are **A** **L**arge **I**on **C**ollider **E**xperiment (ALICE), **A** **T**oroidal **L**HC **A**pparatu**S** (ATLAS), the **C**ompact **M**uon **S**olenoid (CMS) and the **L**arge **H**adron **C**ollider **b**eauty (LHCb) experiment. They are installed around the collision points in underground caverns, as can be seen in Figure 2.1. Moreover two additional experiments will be installed: the **L**arge **H**adron **C**ollider **f**orward (LHCf) experiment close to ATLAS

[1] The Higgs boson is a hypothetical massive scalar elementary particle, whose existence is predicted by the Standard Model.

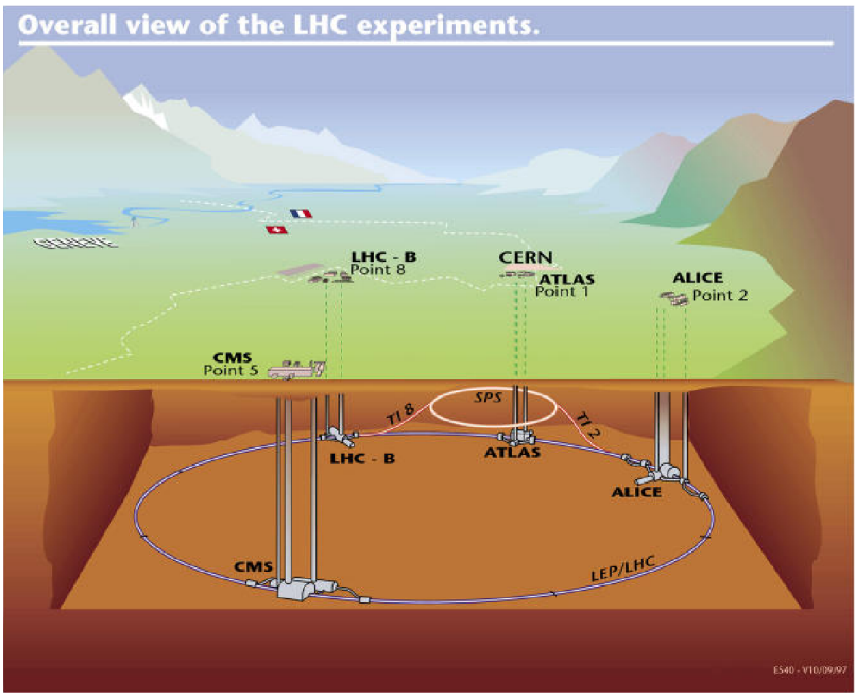

Figure 2.1: *The LHC and its four main experiments [CER09].*

and the **TOT**al **E**lastic and diffractive cross section **M**easurement (TOTEM) experiment near CMS, both sharing an intersection point with the main experiments.

ALICE - A Large Ion Collider Experiment

The ALICE experiment explores the properties of quark-gluon plasma using heavy ion collisions. The experiment will be described in more detail in Section 2.2.

ATLAS - A Toroidal LHC ApparatuS

ATLAS covers the widest possible range of physics at the LHC. Its purpose is the search for the Higgs boson as well as extra dimensions. In addition, it investigates whether leptons or quarks have further substructure. Its enormous cylindrically arranged magnet system makes it the most voluminous collider-detector ever constructed. This magnet system consists of eight 25 m long superconducting magnet coils creating a field of 6 T.

CMS - Compact Muon Solenoid

The CMS detector looks into the same questions as ATLAS using a different physical approach. Its center is a huge solenoid made of a cylindrical coil of superconducting cables. ATLAS and CMS are located at opposite sides of the LHC.

LHCb - Large Hadron Collider beauty

The study of CP violation in the interaction of hadrons containing beauty quarks is the subject of the LHCb experiment. Its vertex locater surrounds the entire collision point. Its other subdetectors are arranged one after another over a range of 20 m, as its main focus lies on detecting particles in the forward direction.

LHCf - Large Hadron Collider forward

The LHCf experiment will asses the particles produced in the forward region during proton-proton collisions. Moreover, it will test models which describe the primary energy of ultra-high energetic cosmic rays. LHCf shares an intersection point with the ATLAS experiment and consists of two detectors installed 140 m on both sides of the collision point.

TOTEM - TOTal Elastic and diffractive cross section Measurement

Elastic scattering, diffractive processes, and the cross section of proton-proton collisions will be measured by the TOTEM detector. It will also provide information about the luminosity of the collider, by detecting particles produced close to the beam pipe. The TOTEM experiment shares an intersection point with CMS [CER08].

2.2 A Large Ion Collider Experiment - ALICE

ALICE is dedicated to heavy ion collisions. Its purpose is to gain more knowledge about the QCD phase diagram and in particular about the QGP phase. The ALICE detector system is able to measure and identify mid-rapidity photons, leptons, and hadrons produced by the collision.
Figure 2.1 shows its location at the intersection **P**oint **2** (P2) experimental area in St. Genis-Pouilly in France. The ALICE project is an international collaboration, consisting of 104 institutes in 31 countries with over 1500 members in total [CER08].

2.2.1 The ALICE Experimental Program

The properties of soft physics will be explored by the ALICE experiment. Moreover, charm and beauty production and hard processes in general will be investigated. This will give new insight into strongly interacting matter at energy densities about 1000 GeVfm^{-3}. Confinement in dense nuclear matter will also be looked into. One of the main goals is to gain deeper understanding of the QGP phase.
The creation of a QGP will be studied at lead ion collisions with center of mass energies up to 5.5 TeV in the intersection point of ALICE. Proton-proton collisions will also be studied in detail [ALI04].

2.2.2 Setup of ALICE

The ALICE setup, as shown in Figure 2.2, consists of several subdetectors, two absorbers, a dipole and the L3 magnet. The total length of its detector system is about 25 m with a height of 16 m and an overall weight of 10000 t.
The subdetectors are arranged in three groups: the muon spectrometer, the forward detectors, and the detectors in the central barrel. To shield the muon spectrometer, an absorber is placed close to the vertex. An iron wall placed after the muon spectrometer serves as an absorber for remaining hadrons.
The L3 magnet, which was originally constructed for the L3 experiment at the **L**arge **E**lectron - **P**ositron Collider (LEP)[2], surrounds the central part of the detector. With a diameter of 10 m and a length of 12 m, it is the largest dipole magnet ever build. The maximum possible field is about 0.5 T.
The central barrel detectors, which are the detectors at central pseudo-rapidity[3], are arranged cylindrically around the intersection point. By this geometry, they cover a pseudo-rapidity of $|\eta| \leq 0.9$ over the full azimuth. The subdetectors are described from the interaction point to the outside in the following:

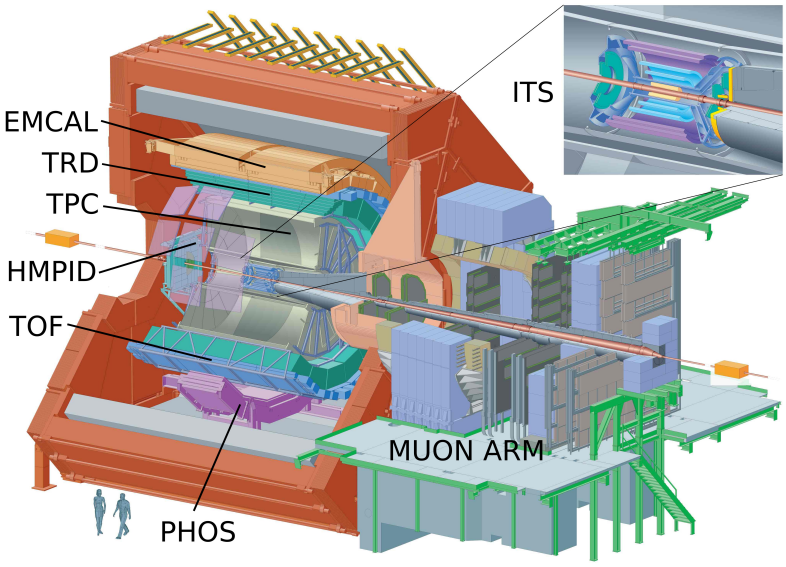

Figure 2.2: *Schematic view of the ALICE detector [Wul09], based on [ALI04].*

[2]The **L**arge **E**lectron - **P**ositron Collider (LEP) is a former collider at CERN used from 1989 until 2000 [MP90].

[3]Pseudo-rapidity is a spatial coordinate which describes the angle of a particle with respect to the beam axis. It is defined as $\eta = \ln\left[\tan\left(\frac{\Theta}{2}\right)\right]$, where Θ denotes the angle between the beam axis and the particle momentum.

Inner Tracking System - ITS

The **I**nner **T**racking **S**ystem is made of six layers of high-resolution silicon detectors: Two silicon pixel, two silicon drift, and two silicon strip detectors. It covers a pseudo-rapidity range of $| \eta | \leq 0.9$ and is optimized for a high resolution and a precise track finding. Thus, the inner radius of the ITS of 5 cm is the same as the outer radius of the beam pipe and its outer radius is adjusted to the TPC.
Its main purpose is primary vertex detection, which can be achieved with a resolution of < 100 µm and measuring particles at low momentum. Also secondary vertices will be reconstructed with ITS.

Time Projection Chamber - TPC

The **T**ime **P**rojection **C**hamber consists of a large cylindrical field cage, which is read out by multi-wire proportional chambers. Being the main tracking device of ALICE, it provides a good particle identification, location of the vertex, and two-track resolution. The TPC covers a pseudo-rapidity range of $| \eta | \leq 0.9$. Having full azimuthal coverage, the TPC makes a global analysis of events possible, i.e. the event plane can be determined.
A good track matching with the ITS detector allows for secondary vertex reconstruction. For tracks with momentum larger than 1 GeV/c a comparison with other detectors also leads to an improved momentum resolution compared to the TPC standalone tracking [ALI04].

Transition Radiation Detector - TRD

The **T**ransition **R**adiation **D**etector comprises 522 detector modules, each consisting of a radiator, drift region, and multi-wire proportional chamber. Its main task is electron identification at a momentum above 2 GeV and fast triggering on high p_{T} (> 3 GeV/c) particles. The TRD also serves as tracking device. Like the rest of the central barrel detectors, it covers a pseudo-rapidity range of $| \eta | \leq 0.9$. A more detailed description of the TRD is given in Chapter 3 [ALI01], [ALI04].

Time Of Flight - TOF

The **T**ime **O**f **F**light is based on a **M**ulti-gap **R**esistive **P**late **C**hamber (MRPC) detector. TOF serves as a particle identification array with a pseudo-rapidity of $| \eta | \leq 0.9$ in a momentum range of 0.3 GeV/c - 3.5 GeV/c. Since most charged particles are emitted within this range, a precise TOF is crucial for ALICE. In combination with ITS and TPC, an event by event identification of kaons (K), protons, and pions (π) is achieved.

High Momentum Particle Identification Detector - HMPID

The identification of high momentum particles is performed by an array of ring imaging Cherenkov detectors, that build the **H**igh **M**omentum **P**article **I**dentification **D**etector. The HMPID covers a rapidity of $| \eta | \leq 0.6$ with an azimuthal coverage of 57.6°.
The single-arm array detector is installed at the 2 o'clock position. A π/K and K/p discrimination can be performed up to 3 GeV/c and 5 GeV/c, respectively.

PHOton Spectrometer - PHOS

The **PHO**ton **S**pectrometer is a high-resolution electromagnetic spectrometer with high granularity. A charged-particle veto detector and an electromagnetic calorimeter, consisting of arrays of high-density crystals, comprise PHOS. It covers an azimuthal range of 100° at a rapidity of $| \eta | \leq 0.12$. Thus, it provides detection of charged particles within a limited central rapidity acceptance, identification of electrons, neutral mesons, and photons. The π^0 spectrum at high p_{T} is measured via photon decay. Furthermore, the initial phase of the collision is examined by measuring the spectra of direct single-photons and diphotons as well as Bose-Einstein correlations of direct photons [ALI04].

ElectroMagnetic CALorimeter - EMCAL

The **E**lectro**M**agnetic **CAL**orimeter is a layered lead-scintillator sampling calorimeter with an azimuthal acceptance of 110° and a rapidity range of $| \eta | \leq 0.7$. It improves the jet quenching measurements by providing a unbiased fast trigger (L0/1) on high energy jets and reducing the measurement bias of jet quenching. Also rare electromagnetic probes like high energy photons and high p_{T} electrons can be detected [CER10], [ALI06].

3. The ALICE Transition Radiation Detector

3.1 Tasks of the TRD

The ALICE Transition Radiation Detector is a gaseous detector, which was introduced into ALICE mainly to identify electrons and to act as a fast trigger on electrons with high transverse momentum.
With the possibility to determine a trigger decision on electron/positron pairs with a p_{T} larger than 2 GeV within 6.5 µs, a study of J/Ψ, Υ[1], and jets is possible. The TRD also provides the possibility to distinguish electrons and pions in the central barrel with momenta above 1 GeV/c. At $p > 3\mathrm{GeV}/c$ a 1% pion efficiency is achieved. Thus, the continuum in the invariant mass spectrum between the J/Ψ and the Υ can be determined. The production of light and heavy vector mesons[2], as well as the dilepton continuum in p-p and lead-lead (Pb-Pb) collisions, will be studied by combining the PID information of the TRD, TPC, and TOF. Together with ITS measurements, a reconstruction of open beauty and open charm in semileptonic decays will be possible [ALI08a].

3.2 Transition Radiation

When a charged particle crosses a boundary between layers of materials with different dielectric constant, transition radiation (TR) can be produced. This is due to the change of the phase velocity of its electromagnetic field. The probability of producing transition radiation increases with the Lorentz factor $\gamma = \frac{E}{m_0 c^2}$, with E being the particle's energy and $m_0 c^2$ its rest energy. Detection of produced TR by the TRD is possible for relativistic particles with $\gamma \geq 1000$. Their produced radiation lies in the region of x-rays, for which the TRD is sensitive. The transition radiation's spectral dependency $\frac{\mathrm{d}^2 W}{\mathrm{d}\omega \mathrm{d}\Omega}$ is given by Equation 3.1 [And]:

$$\frac{\mathrm{d}^2 W}{\mathrm{d}\omega \mathrm{d}\Omega} = \frac{\alpha}{\pi^2} \left(\frac{\theta}{\gamma^{-2} + \theta^2 + \xi_1^2} - \frac{\theta}{\gamma^{-2} + \theta^2 + \xi_2^2} \right)^2 . \tag{3.1}$$

In this equation W denotes the intensity of the emitted radiation, ω its frequency, and θ the angle in which the photon is emitted with respect to the particle trajectory. α represents the fine structure constant $\alpha = 1/137$ and $\hbar$ the Planck constant. $\xi_{1/2}$ are functions of the plasma frequencies $\omega_{1/2}$ of the two different media and fulfill the relation $\xi_{1/2} = \frac{\omega_{1/2}^2}{\omega^2} \ll 1$.

[1] The Upsilon (Υ) particle is a meson consisting of a bottom quark and a bottom antiquark.
[2] Vector mesons are mesons with total spin 1 and odd parity.

Given Equation 3.1 the predominant amount of photons are emitted within a small cone of angle $1/\gamma$ with respect to the direction of motion of the particle.
The overall emitted intensity W of the transition radiation, upon crossing of a single surface, is roughly proportional to γ [ESA00], [PRSZ04]:

$$W = \frac{\alpha\hbar}{\pi}\frac{(\omega_1 + \omega_2)^2}{\omega_1 + \omega_2} \cdot \gamma. \tag{3.2}$$

3.3 Design and Working Principles of the TRD

The TRD is located between TPC and TOF at a radial interval of 2.9 m - 3.7 m with full azimuthal coverage. It is inserted in a mechanical support structure, the so-called space frame, that supports its overall weight of about 30 t. In φ direction, the TRD is segmented in 18 super modules. The readout chambers are arranged in five stacks in beam direction and six layers in radial direction in each super module. Altogether the TRD comprises 522 readout chambers[3] [Ems10]. Figure 3.1 shows a schematic view of the TRD.
Figure 3.2 shows the super module support structure and side panels. The five different stacks, consecutively numbered from 0 to 4 as they get closer to the muon arm, can be seen. Also the six rails on each side panel, the so-called chamber ledges, are depicted. The readout chambers are mounted on these ledges. They are an indicator for the six layers, numbered consecutively from 0 at the bottom to 5 at the top of a super module.

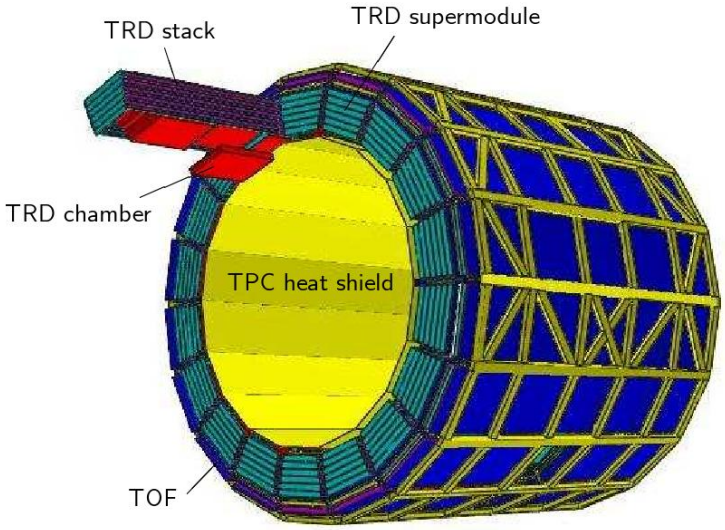

Figure 3.1: *Schematic view of the ALICE TRD [ALI08b].*

[3] In principle each super module comprises 30 readout chambers. The three stacks at $\eta = 0$ of the super modules in sector 13, 14 and 15 (see Figure 3.14) are located in front of PHOS and therefore left empty to minimize radiation length.

For mechanical support, vertical frames are inserted between the different stacks. Stack 0 and stack 1, as well as stack 3 and stack 4, are separated by an individual vertical frame, the so-called stair frame, on each layer. Stack 2, the innermost one, is separated from the others by two vertical frames made of one piece.

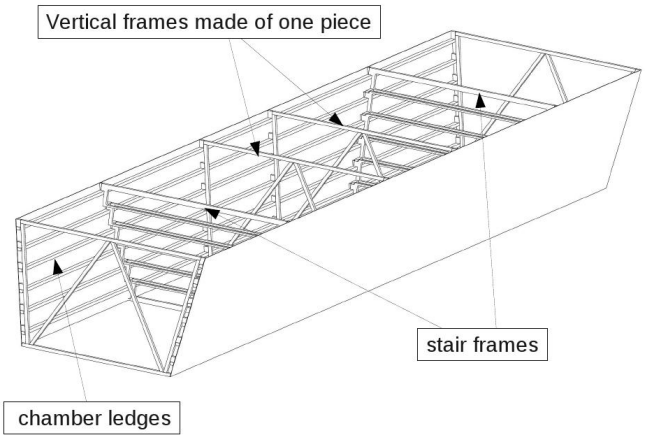

Figure 3.2: *Sketch of the hull and inner support structure of a super module (c.f. [ALI01]).*

3.3.1 The Readout Chambers

The readout chambers are, together with the integrated frond-end electronics, the central pieces of the TRD. The transition radiation is produced and detected in the same chamber.

Layout of the Readout Chambers

Each TRD chamber consists of a multi wire proportional drift chamber, a radiator, and readout electronics.
The radiator is a sandwich consisting of two 0.8 cm thick outer foam plates made of Rohacell HF71 and a filling of polypropylene fiber mats of 3.2 cm thickness in total. The selection of the material was based on good TR performance, as well as chemical and mechanical stability. Mechanical stability is important, as the Radiator serves as top cover of the readout chamber. Hence, it has to be stable against pressure to prevent a deformation of the chamber.
The drift chamber is installed next to the radiator. It consists of a 30 mm drift region and a 7 mm amplification region and is filled with a Xe/CO_2 (85/15) mixture. The drift region starts right after the radiator with a drift cathode set to -2.1 kV. A grounded cathode wire plane divides drift and amplification region and provides a homogeneous drift field. As depicted in Figure 3.3, the anode wires, set to a potential of +1.5 kV, are centered between the readout pad plane and cathode wire plane. The readout pads are

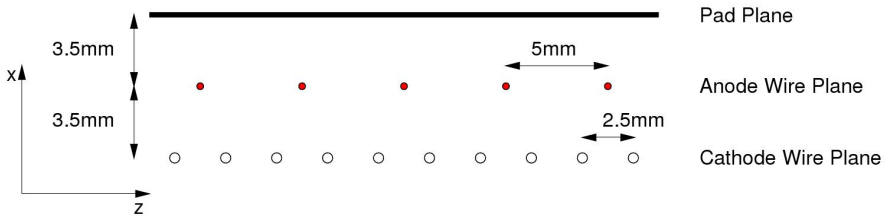

Figure 3.3: *Geometry of the TRD readout chamber wires in local tracking coordinates (see Section 3.5.2) [ALI01].*

larger in z-direction (parallel to the beam axis), than in y-direction (perpendicular to the beam axis), as can be seen in in Figure 3.4. On top of the readout chamber the readout electronics are located. Cooling devices are mounted directly on the electronics.

Two different types of readout chambers are used: C0 and C1 chambers. The main difference between these chamber types are the number of ADC pads, hence readout channels (see Section 3.3.2). C0 chambers are installed in stack 2 at η=0, whereas the C1 chambers are installed in the other four stacks. The shape of the super modules leads to an unequal size of the different readout chambers. Only C0 chambers have the same length of 1080 mm in all layers. The size of the other chambers increases with growing layer number. Their length varies between 1220 mm - 1450 mm. Also the width of all chambers, including the C0 chambers, rises from 922 mm to 1144 mm.

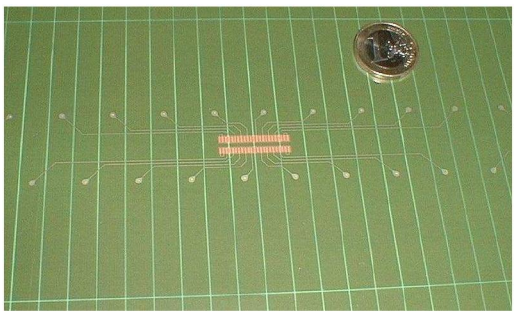

Figure 3.4: *Picture of the pad plane [pad09].*

Signal Generation in the Readout Chambers

When a charged particle crosses the drift chamber, it ionizes the gas atoms along its way. In this process, primary electron clusters and positively charged gas ions are generated (see top left panel of Figure 3.5). Drifting along the lines of the electric field of 700 V/cm, applied between drift cathode and cathode wires, the electrons travel through the drift region at constant velocity of a few cm/µs. After entering the amplification region, they

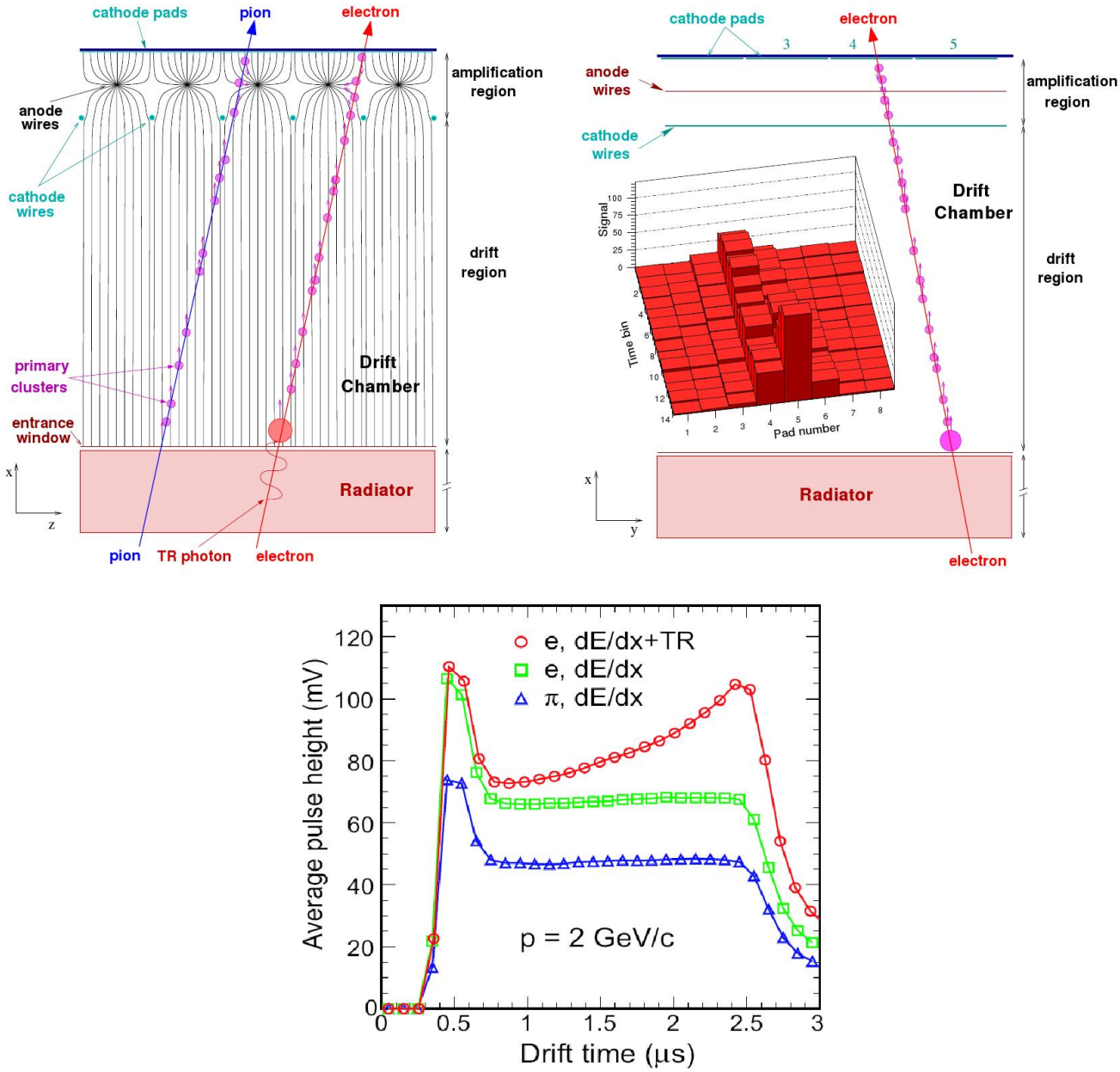

Figure 3.5: *Top left panel: Sketch of the cross section of a readout chamber crossed by a pion and an electron in local tracking coordinates (see Section 3.5.2). Only the electron creates a transition radiation photon in the radiator. Top right panel: Illustration of the resulting signal over* 14 *time bins in the drift region for different pads of one chamber. Bottom panel: Average pulse height of electrons with TR (red), electrons without TR (green), and pions (blue) as a function of drift time [ALI08b].*

are accelerated and thus gain enough energy to ionize gas atoms close to the anode wires. This leads to an avalanche of electrons. As those electrons are created close to the anode wires, they are collected by them in less than a nano second [ALI01]. Because the mobility[4] of the gas ions is 100 to 1000 times lower than the one of the electrons, they remain much longer in the vicinity around the anode wire. Thus, they effectively lower the intensity of the field of the anode wire. This effect leads to a decrease of the gas gain and is in general called space charge effect. Because the electrons are created close to the anode wire, they induce a very small signal. Most of the signal is induced by the slowly moving ions.
The time evolution of the signal is shown in the bottom panel of Figure 3.5. The characteristic peak around 0.5 µs is created due to the signal in the amplification region. The blue triangles in the pulse height plot in the bottom panel of Figure 3.5 indicate a signal produced by pions with a Lorentz factor of $\gamma \approx 10$. This is the case for pions in ALICE. Due to the large absorption cross section of xenon, transition radiation photons are absorbed shortly after entering the drift region. This leads to an additional electron cluster reaching the anode wires at the end of the drift time, which results in a peak in the deposited charge, as depicted by the red circles in the bottom panel of Figure 3.5. The green squares indicate the pulse height for electrons which have not produced transition radiation.
The top right panel of Figure 3.5 shows the detected signal on adjacent readout pads over different time bins. As can be seen, the time bins correspond to the x-positions of the particle track, while the pad numbers correspond to the y-position (in the local tracking coordinate system, see Section 3.5.2).

Gas Gain in the Readout Chambers The gas gain g can be determined as the ratio of the number of secondary electrons produced in the avalanche ($\#e^-_{\text{sec}}$) and the number of primary electrons ($\#e^-_{\text{prim}}$):

$$g = \frac{\#e^-_{\text{sec}}}{\#e^-_{\text{prim}}} \tag{3.3}$$

In order to draw conclusions from the detected energy deposited on the readout pads the gas gain has to be determined. Therefore, it has to be taken into account how the gain is influenced by various parameters. The detector gas composition, temperature and pressure, as well as the anode voltage, directly influence the number of electrons produced in the avalanche. Hence, they have a significant influence on the gas gain. Also mechanical deformations of the chamber, for example due to wire tension, wire sag or the difference in pressure inside and outside the gas volume, have a noticeable effect on the gas gain.
Moreover, due to the space charge effect, the measured gas gain depends on the incident angle of the track with respect to the axis perpendicular to the anode wire plane: The amount of deposited energy of the particle is higher at a large angle. Figure 3.6 shows

[4]The mobility μ is the ratio of the drift velocity V_{d} of ions and the electric field E they are exposed to. It is defined as $\mu = V_{\text{d}}/E$.

the relative gas gain for different angles between track and anode wire plane and different absolute gains. The dependence of the gain on the incident angle can clearly be seen. A compromise has to be found between the required high gain and the desired small influence of the angle. A gas gain of 10000 (see midsection of Figure 3.6) was chosen for the ALICE TRD [ALI01].
In Section 3.4 a more detailed introduction to gas amplification in multi wire proportional chambers is given.

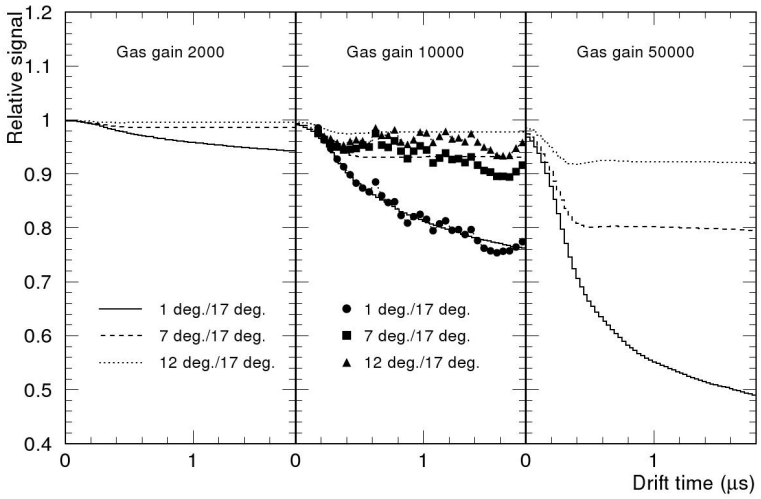

Figure 3.6: *Results of electrostatic calculations of the relative gas gain as a function of the drift time. The three different areas mark the different absolute gas gains 2000, 10000, and 50000 for which the relative gain was determined. For comparison all relative gains are normalized to a gain of* 1 *at* 17°*. The different lines and symbols correspond to the angle between track and anode wire plane: solid line/circle:* 1°*; dashed line/squares:* 7°*; dotted line/triangle:* 12° *[ALI01].*

Pad Response Function The **P**ad **R**esponse **F**unction (PRF) can be used to determine the precise position of a particle crossing the TRD by analyzing the charge distribution on the pads.
The PRF is the quotient of the charge Q_{single} induced on a single pad and the totally induced charge Q_{total}. In the TRD three pad clusters are assumed, therefore it is defined as

$$PRF = \frac{Q_{\mathrm{single}}}{Q_{\mathrm{total}}} = \frac{Q_{\mathrm{i}}}{Q_{\mathrm{i-1}} + Q_{\mathrm{i}} + Q_{\mathrm{i+1}}}, \tag{3.4}$$

where Q_{i} denotes the charge on the examined pad and $Q_{\mathrm{i-1}}$ and $Q_{\mathrm{i+1}}$ the charge on its left and right neighbor pads. As can be seen in Figure 3.7, the PRF (black dots) shows a nearly Gaussian shape (red fit). By taking this into account a function to determine a precise

y-position within one time bin, in dependence on the pad width W, can be approximated to

$$PRF \approx Ae^{-\frac{y^2}{2\sigma^2}}, \tag{3.5}$$

with A representing the amplitude of the Gaussian function and σ its variance.
Transformation of Equation 3.5 leads to the following function to determine the precise y-position on a pad [Wul09]:

$$y = \frac{W}{Q}\frac{\ln(Q_{\mathrm{i}+1}/Q_{\mathrm{i}-1})}{\ln(Q_{\mathrm{i}}^2/Q_{\mathrm{i}-1}Q_{\mathrm{i}+1})} \tag{3.6}$$

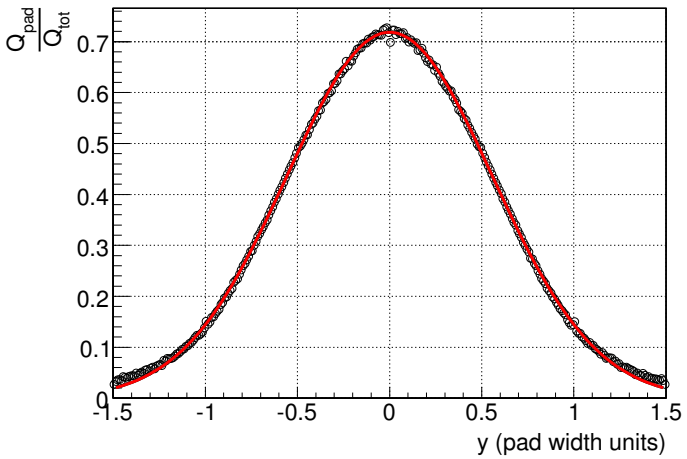

Figure 3.7: *Pad Response Function plotted vs. the pad width. The black dots represent the mean of the measured PRF. A Gaussian fit is indicated by the red curve [Wul09].*

Time Response Function The time response function describes the signal of a detector to a given charge as a function of time (Figure 3.8). Within the TRD, the slowly moving ions lead to a long ion tail of the signal extending over several micro seconds. As this ion tail provides a signal in subsequent time bins on the same pad, the signal of the following time bins is influenced by superposition and its quality is declined.
Moreover, the performance of the preamplifier/shaper in the multi chip modules influences the signal (see Section 3.3.2).

3.3.2 The Frond-End Electronics

The TRD **F**rond-**E**nd **E**lectronics (FEE) are subdivided into the **F**ront-**E**nd **R**ead**O**ut Electronics (FERO), which comprise all electronics mounted directly on the readout chamber, and the **G**lobal **T**racking **U**nit (GTU). The FERO includes the **D**etector **C**ontrol

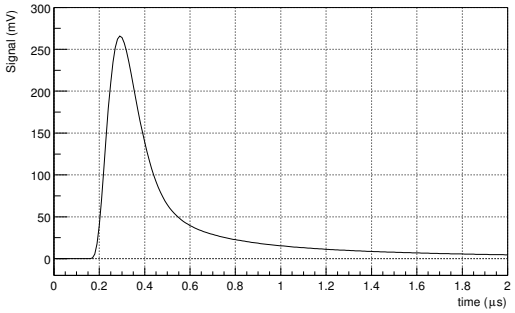

Figure 3.8: *Time Response Function of the TRD created by a MAGBOLTZ/GARFIELD simulation [ALI01].*

System board (DCS board), **M**ulti **C**hip **M**odules (MCMs), which read out the cathode pads, and **O**ptical **R**eadout **I**nterface boards (ORI boards), which transfer the determined data from the readout chambers to the GTU. The MCMs and ORI boards are controlled and configured by the DCS board. The **S**low **C**ontrol **S**erial **N**etwork (SCSN) interface, which is controlled by the FEE-Server, is used for this communication [Wes09].
One of the main tasks of the TRD is to trigger on high p_{T} electrons. As the contribution of the TRD to the trigger decision of ALICE has to be made within 6.5 µs, the determined data has to be processed at an early stage after the collision. Therefore, a first analysis is performed locally in the MCMs.
The **P**re **A**mplifier and **S**h**A**per (PASA) and the **TRA**cklet **P**rocessor (TRAP) compose the MCM. The TRAP chip itself consists of the **T**racklet **P**re **P**rocessor (TPP), an **A**nalog to **D**igital **Converter** (ADC), an event buffer, and four **M**ultiple **I**nstruction **M**ultiple **D**ata **C**entral **P**rocessing **U**nits (MIMD CPU). 18 pads are read out by one MCM. In order to process data at the border channels, the MCM also receives information from adjoining MCMs about three neighbor pads. Altogether data is received by the MCM via its 21 ADC channels. Therefore, the 144 pads in each column are managed by eight MCMs.
The incoming signal is individually shaped and amplified by the PASA and transmitted to the ADC that converts it to a digital signal. The conversion rate of the ADC is 10 MHz with a resolution of 10 bits. Subsequently, the raw or filtered data is stored in the event buffer for potential further readout after a positive L1 trigger decision. The amplified signal is then filtered and the TPP looks for possible hits. Thereby, the clusters are parametrized and the fit registers filled. Over a range of several time bins, this information is used by the MIMD CPUs to determine the so-called tracklet, which is a straight line fit through the clusters presumably belonging to a particle track segment within one readout chamber. Information about the tracklets is then shipped via optical fibers to the GTU with a rate of 216 GB/s [Wal10]. Figure 3.9 gives an overview of the online data processing schema.
In the GTU, the tracklets of individual readout chambers within one stack are combined

in the following way: Information about the position and angle of each determined tracklet within a small time window are projected to a virtual middle plane. A sliding window algorithm is performed to determine tracklets that might be produced by the same particle. Those tracklets are than fitted to a single track through all six layers [ALI01].

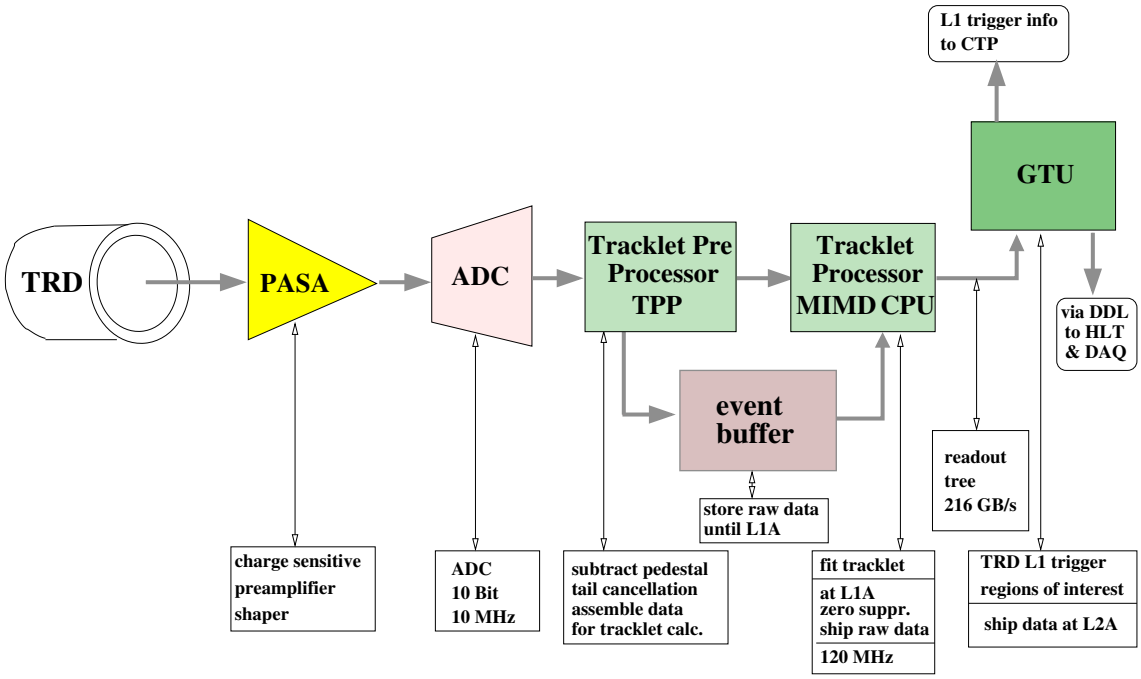

Figure 3.9: *Schema of the TRD data processing tree [ALI01].*

3.4 Gas Gain in the TRD Readout Chambers

3.4.1 Energy Deposit in Gas

When a charged particle traverses the TRD, it ionizes gas atoms along its way and thereby deposits parts of its energy in the gas.
The average energy loss of a charged particle by ionization per unit length traveled $\frac{dE}{dX}$ is given by the semi-phenomenological relativistic Bethe-Bloch equation. In the electrostatic unit system it denotes [Sau77]:

$$\frac{dE}{dX} = -\frac{2\pi N z^2 e^4}{mc^2} \cdot \frac{Z}{A}\frac{\rho}{\beta^2}\left\{\ln\left(\frac{2mc^2\beta^2 E_{\mathrm{M}}}{I^2\cdot(1-\beta^2)}\right) - 2\beta^2\right\}. \tag{3.7}$$

In this Equation N depicts the Avogadro number, m the mass of the electron and e its charge. c denotes the speed of light. ρ indicates the density of the medium, A the atomic number and m the mass of the particles of the medium. I stands for its effective ionization

potential. z represents the charge and β the velocity (in units of the speed of light c) of the projectile. E_{M} denotes the highest possible energy transfer in each interaction:

$$E_{\mathrm{M}} = \frac{2mc^2\beta^2}{1-\beta^2}. \tag{3.8}$$

The particle's velocity has a dominant influence on the mean energy loss. At low velocity the average energy loss per unit length decreases proportionally to $1/\beta^2$.
Figure 3.10, determined after Equation 3.7, shows the average energy loss per length unit traveled in air for different particles. As can be seen, for energies above about 10^3MeV all particles lose nearly the same amount of energy. In this region it is difficult to distinguish particles, such as electrons and pions, by their energy loss [Sau77].
At even higher velocity, the energy loss finally saturates for all particles at around the same value.

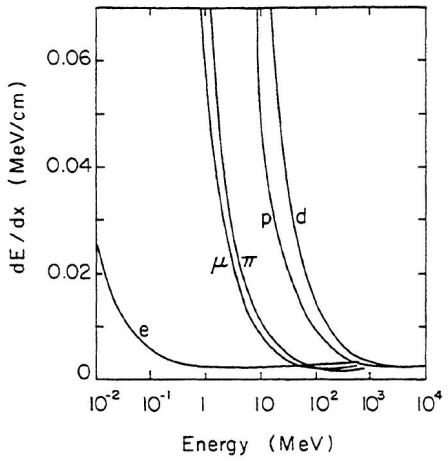

Figure 3.10: *Energy loss per length unit traveled in air for different particles as a function of particle energy [Sau77].*

3.4.2 Amplification of the Signal

Given Equation 3.7, about 850 electron/ion pairs are created by each ionizing particle in the drift region of the readout chambers. The readout pads have a capacity of 20 pF, which leads to an amplitude of the signal of about 2.36 µV [Bai08]. Since this is too small to be analyzed, an amplification of the signal is necessary. Therefore, the amplification region was implemented in the readout chambers.
The TRD is operated as multi-wire proportional counter, which can be described as an array of independent proportional counters. Figure 3.11 illustrates a single cylindrical coaxial

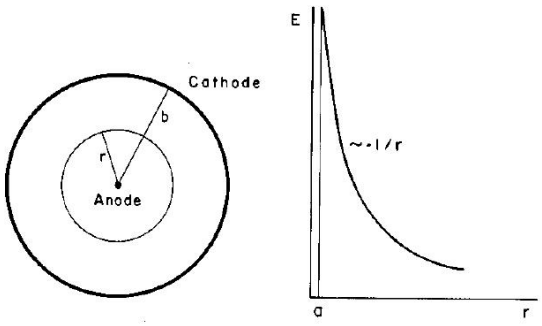

Figure 3.11: *Left: Cross-section of a coaxial cylindrical proportional counter with thin anode wire. Right: Electric field E as a function of the radius r [Sau77].*

proportional counter and the strength E of the electrical field it generates depending on the distance r to the anode. E is described by

$$E(r) = \frac{\lambda}{2\pi\epsilon_0}\frac{1}{r}, \tag{3.9}$$

with λ being the linear charge density and ϵ_0 the vacuum permittivity. For the desired strong electrical field, a thin anode wire is required. This is realized by an anode wire radius of 20 µm for the ALICE TRD [ALI01]. With a sufficient electric field, the electrons accelerate and ionize gas atoms. Hence, an avalanche is created. The original deposited charge is amplified. The resulting signal is proportional to the original deposited charge, and the amplification factor is called gain factor.

In order to achieve a high gas gain even in the presence of a comparatively low electric field, most gas detectors are operated with a noble gas. This way the absence of additional degrees of freedom compared to more complex molecules such as CO_2 is provided. The fewer the number of degrees of freedom is, the lower are the chances that the energy of an electron is absorbed before it ionizes a gas atom. As the noble gas is not only ionized but also excited by the particle crossing the chamber, it emits photons when returning to the ground state. These photons might produce a second avalanche by ejecting electrons out of the metal electrodes. In order to prevent this, a gas which can easily absorb the emitted electrons is needed. This so-called quenching gas (e.g. CO_2), whose molecules provide various degrees of freedom, is added to the noble gas.

When operating the chamber in proportional mode, the amplification factor can be determined from the first Townsend coefficient α. α is a function of the reduced electric field strength $S = E/\rho$, with E being the electric field and ρ the particle density. In general α depends on the gas type and electric field [Dav06]. The number N_e of electrons at a given position increases by dN_e depending on α after a path dr:

$$dN_\mathrm{e} = N_\mathrm{e}\alpha dr \tag{3.10}$$

The mean free path between ionization processes corresponds to the inverse of α.
Integrating Equation 3.10 gives the amplification factor g, thus the gas gain:

$$g = \exp\left(\int_{r_0}^{r_a} \alpha(r)\mathrm{d}r\right) = \frac{N_e(r_a)}{N_e(r_0)} \tag{3.11}$$

It equates to the ratio of electrons $N_e(r_a)$ collected at the surface of the anode wires with radius r_a and the number of initial electrons $N_e(r_0)$ at the starting point r_0 of the avalanche. In the case of the TRD, this corresponds to the number of secondary and primary electrons [Sau77].
For moderate gas gain, the dependence of the Townsend coefficient on the energy of the electrons is nearly linear. Hence, the gas gain depends exponentially on the anode voltage. An increase of the anode voltage of about 3.6% from 1400 V to 1450 V would result in an increase of the amplification factor of over 70% [ALI01]. Hence, variations of the anode voltage over time have to be avoided. Therefore, a sensitive power supply is used, which allows to control the anode voltage with a precision better than 1 V [Bai08]. It was shown for the TRD, that for a rise of 1 V of the anode voltage, the gas gain increases only about 1% [Alb10].
The gas gain depends not only on the anode voltage, but also on the gas density ρ. ρ depends on the absolute pressure p and the temperature T:

$$\rho \sim \frac{p}{T}. \tag{3.12}$$

An increase of 1% of the density leads to a decrease of the gas gain of about 6% - 7% [ALI01].
Moreover, a difference of pressure inside and outside of the detector chamber has an effect on the gas gain. With a higher pressure inside, the chamber tends to bend outwards. Thus, the cathode pads bend away from the anode wires, which leads to a decrease of the gas gain. The opposite effect happens for lower pressure inside the readout chamber [Alb10].

3.4.3 Fluctuation of Energy Loss

In a thin layer of gas, only a small number of interactions take place. As the possible energy transfer for each interaction is widely spread, the total energy loss fluctuates and is statistically distributed in the shape of a Landau function:

$$f(\lambda) = \frac{1}{\sqrt{2\pi}} \cdot e^{-\frac{1}{2}\left(\lambda + e^{-\lambda}\right)}. \tag{3.13}$$

In this equation λ denotes the normalized deviation of the most probable energy loss $(\Delta E)_{\mathrm{mp}}$

$$\lambda = \frac{\Delta E - (\Delta E)_{\mathrm{mp}}}{\langle E \rangle}, \tag{3.14}$$

with ΔE being the actual energy loss of a given particle and $\langle E \rangle$ the average energy loss for a given path in the gas volume.
Figure 3.12 shows the normalized Landau distribution. The long tail at higher λ is due to rare processes with a high energy transfer. In the TRD this corresponds to high energy δ-electrons which can ionize further gas atoms, thus producing additional drift electrons. The average energy loss is represented by the mean value of the distribution. Due to the asymmetrical shape of the distribution, it does not reflect the most probable value (MPV). As a result of large fluctuations, any calculations of the gas gain that are based on the dE/dX spectra have to be performed with high statistics [Bai08].

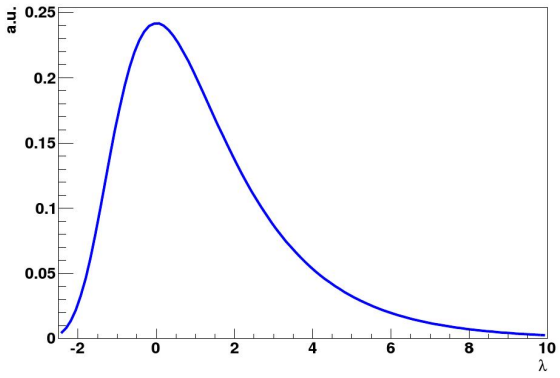

Figure 3.12: *The Landau distribution as a function of the normalized deviation λ of the most probable energy loss [Alb10].*

3.5 Conventions of Coordinate Systems and Numbering within ALICE

Various coordinate systems and numbering conventions exist within ALICE for different tasks, some of them covering the whole experiment, others only parts of the detectors. The most important conventions concerning the subject of this thesis are explained in the following.

3.5.1 The Global ALICE Coordinate System

The global ALICE coordinate system, which is also referred to as lab frame, is a right-handed Cartesian coordinate system which can be seen in Figure 3.13. Its z-axis follows the beam direction into the opposite direction as the muon arm, the y-axis is pointing up, and its x-axis is pointing to the LHC-center. The intersection point of the TPC central membrane and the z-axis defines the origin, which thereby is located close to the vertex.

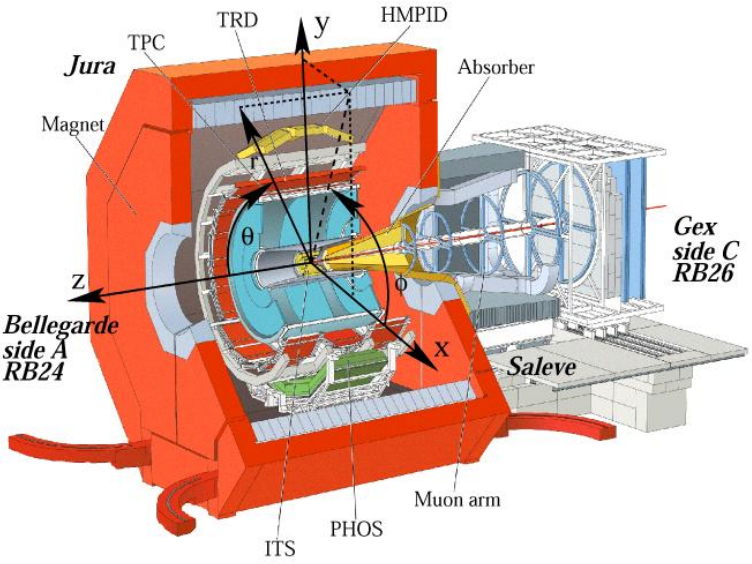

Figure 3.13: *Sketch of the ALICE detector system showing its global coordinate system using the Cartesian coordinates x, y and z, or the polar coordinates z, r and θ or respectively Φ [BC03].*

Each position within ALICE might also be described in a polar coordinate system, consisting of z, r and either θ or ϕ. The z-axes of both global coordinate systems are congruent and point in the same direction. r is equivalent to the radius. ϕ is the angle around which r is rotated counter-clockwise around the z-axis, whereas θ describes the rotation around the x-axis. The origin of this coordinate system is also located at the intersection point of the TPC central membrane and the z-axis.

3.5.2 The Local Tracking Coordinate System of the TRD Super Modules

For the local tracking inside of one TRD super module, its position within the ALICE detector does not matter. Therefore, an individual Cartesian coordinate system, the local tracking coordinate system of the TRD super modules, was introduced. It is the same for each individual TRD super module and consists of an x-, y-, and z-axis, which share the origin with the global ALICE coordinate system. z is the same in the local tracking coordinate system as in the ALICE global coordinate system. x rises with increasing layer number, which can be seen in the right panel of Figure 3.14. It also shows the positions of the different super modules within the cylindrical arrangement of the TRD. As can be seen, by a counter-clockwise rotation around the z-axis of $(10^o + s \cdot 20^o)$, with s being a

factor between 0 and 17 corresponding to the installation slot number, the local tracking coordinate system of each super module can be converted into the global ALICE coordinate system. The super modules in Münster are software wise operated in the position of a 10^o rotation, which corresponds to slot 0.

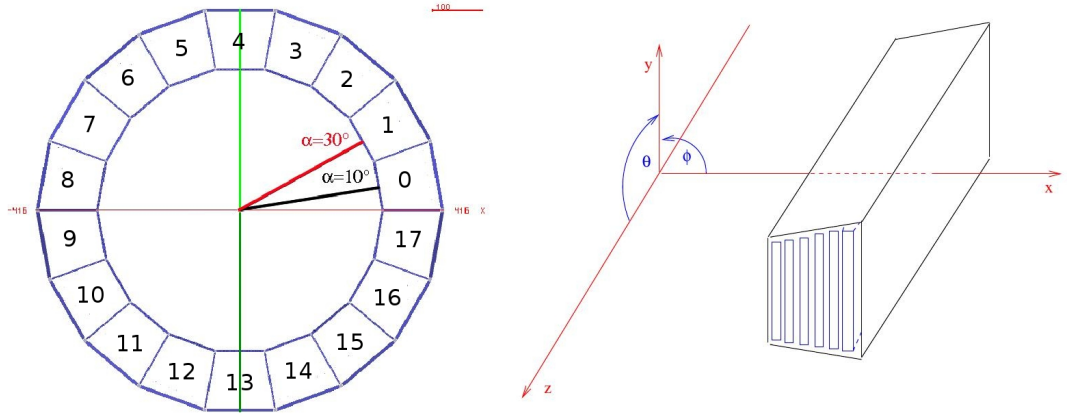

Figure 3.14: *Left panel: Outline of the installation slots for different TRD super modules. Right panel: Outline of the local tracking coordinate system of TRD super modules (c.f. [Sic09]).*

3.5.3 The Local Alignment Coordinate Systems of the TRD

The local alignment coordinate systems of the ALICE TRD are Cartesian coordinate systems using the coordinates r, z, and Φ_r (Figure 3.15). For each volume which is to be aligned, an individual local alignment coordinate system is introduced.
When aligning individual chambers of a super module, the local alignment coordinate system is defined as follows:
Each chamber of the super module has its own alignment coordinate system with the chamber midpoint as origin. The r-axis is congruent to the x-axis and the Φ_r-axis to the y-axis in the local tracking coordinate system. But whereas the r- and x-axis point in the same direction, Φ_r points in the opposite direction of y. When not stated otherwise, the coordinate systems in this thesis refer to the local tracking coordinate system.

3.5.4 TRD Super Module Numbering Convention

Two different numbering conventions exist for the TRD super modules, one used for already installed super modules at ALICE, the other mostly for data taken during the assembly and first calibration procedure.
The super modules installed in the ALICE TRD are labeled according to the sector they are inserted in counterclockwise from 0 to 17 starting with the position right above

3 o'clock.
During assembly the numbering is related to a consecutive roman serial number, representing the order of first assembly. Table 3.1 shows both conventions for the super modules already installed at ALICE, Table 3.2 indicated the conventions for the super modules to be installed.

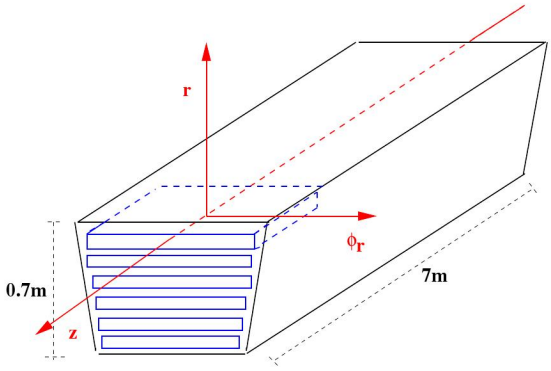

Figure 3.15: *Draft of the local alignment coordinate system used for aligning individual TRD chambers [Sic09].*

Numbering corresponding to insertion into the space frame	0	1	7	8	9	10	17
Numbering corresponding to first assembly	II	VI	III	I	IV	VII	V

Table 3.1: *Numbering conventions of TRD super modules installed at ALICE as of 12.08.2009 (c.f. [sec10]).*

Numbering corresponding to insertion into the space frame	2	3	4	5	6	11	12	13	14	15	16
Numbering corresponding to first assembly	X	XIII	XIV	XV	XII	IX	XVI	XVII	XVIII	XI	VIII

Table 3.2: *Numbering conventions of TRD super modules to be installed at ALICE (c.f. [sec10]).*

4. Calibration Setup for TRD Super Modules in Münster

As part of the assembly procedure in Münster, several million cosmic-ray events are recorded with each super module. With these data, the correct performance of the super modules can be verified. Moreover, the determination of a first set of calibration parameters, such as the drift velocity, the relative gas gain, and the position and orientation of the readout chambers, can be performed.

4.1 Cosmic Radiation

As an omnipresent source of high energy particles, cosmic radiation (abbrev: "cosmics") provide an ideal possibility to test and calibrate the TRD super modules without the need of an accelerator.
Cosmic radiation is subdivided into primary and secondary cosmic radiation. Primary cosmic radiation consists of particles from outer space entering the terrestrial atmosphere. The products of the interactions of primary cosmics with the terrestrial atmosphere are called secondary cosmic radiation.

4.1.1 Primary Cosmic Radiation

Primary cosmic radiation consists of high energy particles created as products of stellar nucleosynthesis and electrons accelerated by cosmic sources. The predominant constituents are protons ($\approx 79\%$) and helium ions ($\approx 15\%$). Moreover, electrons and atoms of iron, carbon, and oxygen, the majority of which are completely ionized, are part of cosmic radiation, with their exact composition depending on their energy. Primary cosmic particles have their origin either in solar flares or outside the solar system. The earth's magnetic field influences the trajectory of the primary particles. Thereby, the flux of primary cosmic radiation is modified close to the earth [Gre66].

4.1.2 Secondary Cosmic Radiation

The decay or reaction of primary cosmic particles with the earth's atmosphere results in the production of secondary cosmic rays at an altitude of 15 km to 20 km. As depicted in Figure 4.1, this interaction can lead to an electromagnetic shower or a hadron shower. When a primary cosmic particle hits a nucleus, such as oxygen or nitrogen, this can lead

to the production of hadrons such as pions, protons, neutrons, and fragments of nuclei. These particles can further interact. π^+ and π^- decay, thereby neutrinos, antineutrinos, muons, and antimuons are created. π^0 can initiate an electromagnetic shower resulting in electrons and positrons.
Most secondary cosmic particles are absorbed in the atmosphere before they reach sea level.

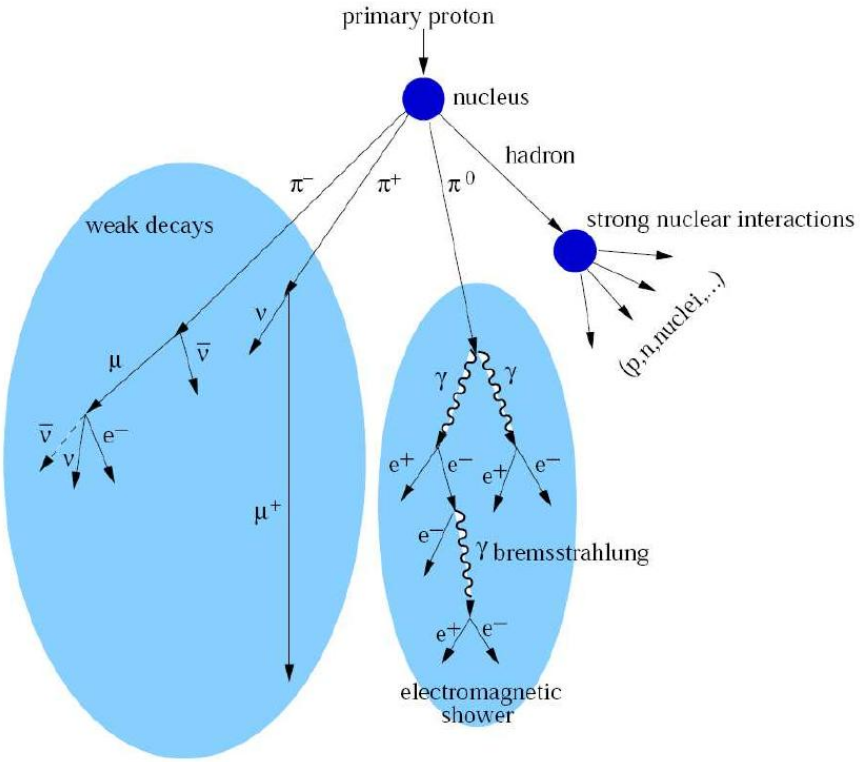

Figure 4.1: *Illustration of produced secondary cosmic radiation and the resulting particle shower ([Alb10] based on [Hop04]).*

4.1.3 Cosmic Radiation at Sea Level

Cosmic rays at sea level are used for calibration of the TRD super modules in Münster and, besides collision data, in ALICE.
The most common cosmic-ray particles at sea level are muons (79%) with a mean energy of about 4 GeV. Most of those muons are created in the atmosphere at a height of about 15 km. Muons have a half-life of $\tau_\mu = 2.197 \cdot 10^{-6}$ s. Due to a relativistic boost of their mean velocity most of them still reach sea level [A$^+$08].

4.2 Cosmic Trigger

In Münster, the setup for the TRD super modules is different from the setup at ALICE. The super modules are operated in stand-alone mode, meaning that each super module is operated as a self-contained detector. The data is taken by the measurement of cosmic rays.
For trigger purposes, two layers of organic scintillators and photo multipliers are installed below and above the super module. The layer beneath the module covers the whole active area of the super module, whereas the layer above is smaller. It covers the whole range in y-direction, but only parts of the z-direction (see Figure 4.2). Therefore, the upper trigger is movable across all stacks of the module (see Figure 4.3), which also gives the option to trigger mostly on particles crossing a specific stack.

The trigger can be operated in different modes, the most important ones being coincidence of the top and bottom scintillator layer ("coincidence") and a combination of the GTU and the bottom scintillator layer("bottom+GTU"). In the coincidence mode, a trigger

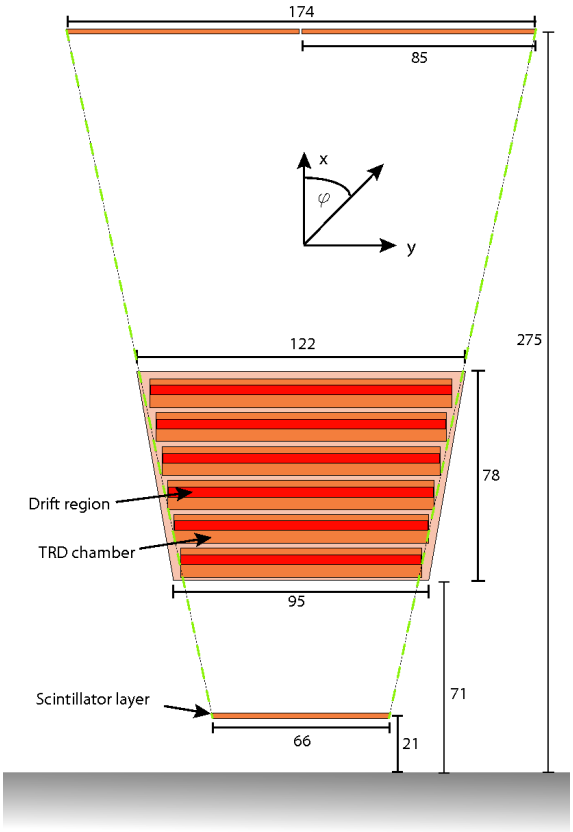

Figure 4.2: *Design of the cosmic trigger setup in Münster in front view. Numbers correspond to centimeter, the coordinate system refers to local tracking coordinates [Bat07].*

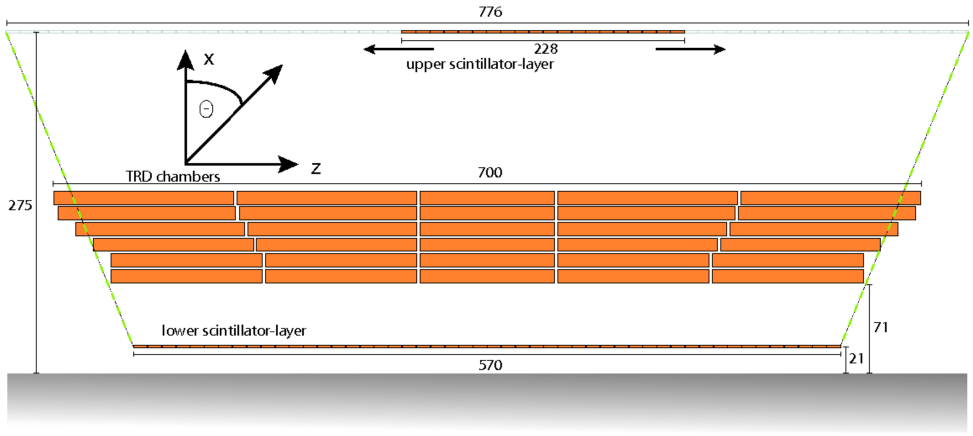

Figure 4.3: *Side faced sketch of the cosmic trigger setup in Münster. Numbers correspond to centimeter, the coordinate system refers to local tracking coordinates [Bat07].*

signal, leading to a full read out of the super module, is given when a particle is detected in the upper and lower trigger within a time interval of 20 ns. In this mode, most of the particles are detected in the stack below the upper trigger.
In the bottom+GTU mode, each hit of the bottom scintillator trigger leads to a pre-trigger signal. Thereafter, the data of the readout pads is processed online (see Section 3.3.2). If tracklets are found in at least four layers of one stack, a trigger signal is sent and the whole super module is read out.

4.3 Gas System

Not only the trigger setup, but also the gas system in Münster differs from the setup of the overall ALICE TRD detector system, where a Xe/CO_2 (85/15) mixture is used. The noble gas xenon is rare in nature and therefore expensive. Argon, which is the most common noble gas on earth and thus cheaper, also provides good characteristics for particle tracking with the ALICE TRD. In order to be able to compare data recorded in Münster with results of CERN surface tests, the same mixture of Ar/CO_2 (82/18) is used in both cases [ALI01].
The exact mixture of the gas has to be adjustable. For example, the characteristics of CO_2 as a quencher can be used, when testing the drift chamber's high voltage. For this purpose, the chambers are flushed with pure CO_2 during the first high voltage test. In order to adjust the gas mixture and flow during assembly, four different gas lines are used. The three so-called mix lines share a common gas input and are each connected to two subsequent layers. Thus, the same gas mixture is chosen for these layers. The flow in each mix line, which directly influences the pressure inside the chambers, can be chosen individually for each line. In addition, a flush line, serving as stand-alone gas input for one

super module layer, is used during the assembly.
For either one or two layers connected to each other, the pressure inside the readout chambers can be influenced by connecting a fan to the gas output of a layer.
The composition of the gas mixture can be determined from mass spectrometer attached to each input line. In addition, the amount of oxygen inside the readout chambers, as well as the pressure and temperature, can be determined for one input line at a time by a gas sensor (ORBISPHERE 510) [Gri09].

4.4 Calibration Parameters of TRD Super Modules in Münster

4.4.1 Alignment

Alignment describes the spatial adjustment of an object relative to other objects. Its goal for the TRD is to match the geometry used during reconstruction and simulation as close as possible to the real geometry.
Due to a limited accuracy during production and assembly of the TRD of about 1 mm, detectors and detector parts are not placed at their exact design position. Also, time driven deformations lead to an imprecise knowledge of these positions. Hence, the final geometry of the TRD does not resemble the ideal design geometry. If the detected signals are interpreted and analyzed only on base of the ideal geometry, an imprecise result will be obtained. In order to minimize this influence and achieve a more precise spatial resolution and vertex reconstruction, the differences in ideal and real geometry of the detector parts have to be identified and taken into account when analyzing the data [Sic09]. The alignment procedure, during which those differences in geometry are determined, is described in more detail in Chapter 5.2.4.

4.4.2 Drift Velocity

The drift velocity of the electrons is a key factor on the determined x-position of a particle track. The x-position is determined as a function of the time t by

$$|x(t)| = \int_{t_0}^{t} v_{\mathrm{d_E}}(t) \cdot \mathrm{d}t. \tag{4.1}$$

In this equation t_0 denotes the start time, which corresponds to the time the particle reached the pad plane. v_{dE} is the drift velocity of the electrons.
In the drift region with homogeneous electric field, the drift velocity has a constant value. Thus, the position can be reconstructed from the drift time as

$$|x(t)| = v_{\mathrm{d_E}} \cdot (t - t_0). \tag{4.2}$$

As can be seen in Equation 4.2, a precise knowledge of the drift velocity is crucial to achieve the design value of the position resolution [Bai08]. In Chapter 5.2.3 the procedure to calibrate the drift velocity will be explained.

4.4.3 Gas Gain

Exact knowledge of the relative gain factors is required for a good particle identification [Wil10]. The procedure to determine the gas gain is described in Chapter 5.2.6.
Precisely determined gain factors are not only important for reconstruction purposes, but also for the usage of the TRD as a trigger. In order to be most functional, it is necessary that each ADC-channel (corresponding to one readout pad) of one MCM has the same overall gas gain. To achieve a uniform gain, in a first step the gain has to be determined as accurate as possible. Based on this knowledge, gain correction factors can be determined and stored in the MCMs, leading to a uniform gain for all of the following data taking [Alb10].

5. The Calibration and Alignment Procedure

During the calibration and alignment procedure of the TRD, deviations between detector values and expected values for several parameters are determined. For the calibration of the super modules in Münster, these parameters are the drift velocity of the electrons, the gas gain, and the orientations and positions of the readout chambers.

5.1 Software Architecture

In order to process the data of the ALICE experiment, the analysis framework AliRoot is used for simulation, reconstruction, and analysis. The code of AliRoot is written in the C++ language using the ROOT system as framework. AliRoot contains special information and parameters for ALICE [roo10], [Ali10a].

5.1.1 The Offline Conditions Data Base - OCDB

The `Offline Conditions Data Base` (`OCDB`) is the place where the calibration and alignment parameters are stored. These parameters are for example the drift velocity, the gas gain, and the deviations between real and ideal geometry. The `OCDB` can be used during simulation and reconstruction, which leads to a better description of the detector. The `OCDB` is not a relational database, such as for example MySQL [myS10]. It comprises a set of entries in an AliEn[1] file catalog containing pointers to the ROOT files with calibration parameters. During simulation and offline reconstruction, the database can be accessed in order to use the determined alignment and calibration parameters instead of the default values [OCD10].
The determined calibration and alignment parameters are stored in files labeled `RunW_X_Y_Z.root`, with `W_X` being the run[2] range in which the calibration object is valid, `Y` the version, and `Z` the subversion number of the files. The `OCDB` of the TRD is stored in a subfolder labeled `TRD` with the actual parameters being stored in subfolders, such as `TRD/Calib/ChamberGainFactor/`, `TRD/Calib/LocalGainFactor/` and `TRD/Align/Data/`.

[1] **Ali**ce **En**vironment (AliEn) is an open source grid framework, which uses a combination of a Distributed Agent Model and a Web Service [Ali10b].
[2] The term run will be explained in Section 5.2.1.

In addition to the `OCDB` on AliEn with the official parameters, a "`local OCDB`" can be created to store parameters temporarily. This option is used for work and progress of detector experts. After verification of the determined parameters, they can be submitted to the official OCDB.

Super Module Integration OCDB - SMint OCDB

For parameters concerning data taken right after the integration of the super module, a special database, the `Super Module integration OCDB (SMint OCDB)`, was created. It contains the determined calibration and alignment parameters for each super module, such as the drift velocity of the electrons within the TRD, and information about the gas gains and the misalignment of the readout chambers.
Moreover, information about various parameters concerning the super module and its environment during data taking can be stored, such as:

- electronic configurations
- trigger setup
- voltage and current of the anode and drift electrode
- pressure and temperature inside the readout chambers[3]
- oxygen content of the readout chambers[3]
- exact gas mixture[4]
- information about the drift velocity[5]

5.1.2 The ALICE Geometry

For tracking, reconstruction, and visualization, knowledge about the geometry of the ALICE detectors is needed. The class `TGeo` can be used to represent this geometry. It is organized in a tree-like structure at the level of shapes with a mother-daughter concept. This means every volume can be a mother volume, hence subdivided into smaller daughter volumes, which can be mother volumes themselves. For example the mother volume TRD consists of 18 super module branches which are its daughter volumes. Each super module

[3] The pressure and temperature inside the readout chambers, as well as their oxygen content, can be determined with a gas sensor for one layer at a time (see Section 4.3).

[4] As part of the gas system a mass spectrometer is installed. Soon it will be possible to determine more accurate information about the gas mixture inside the super modules.

[5] In the near future a **G**as pr**O**portional c**O**unter **F**or dr**I**fting **E**lectrons (GOOFIE) will be installed to become part of the quality assurance during super module assembly.

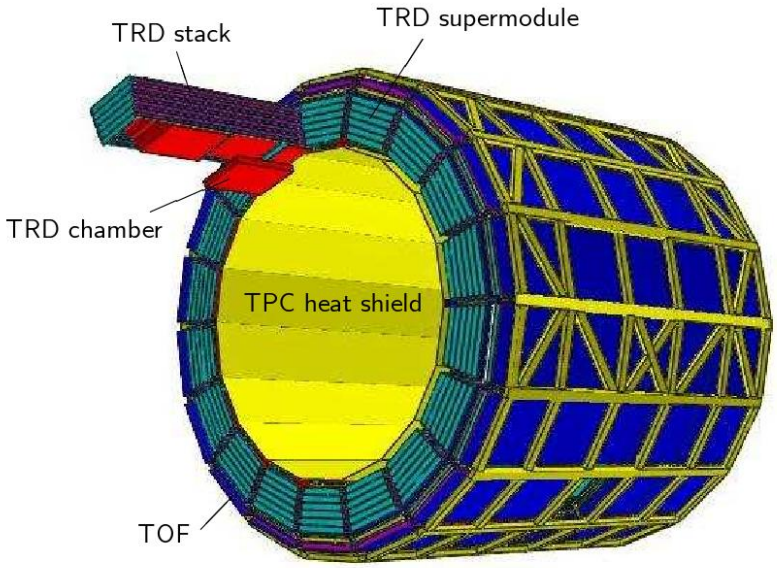

Figure 5.1: *Schema of the ALICE TRD depicting the different volumes TRD, super module, stack, and chamber.[ALI08b].*

can be seen as a mother volume with its five stacks being daughter volumes. These daughter volumes themselves serve as mother volumes to their comprising layer (see Figure 5.1). Every volume can be identified by its volume path, which is going from the outermost mother volume to the innermost daughter volume. A '/' is used for separation purpose of the different volumes. For example `TRD/sm01/st3/pl2` would be the chamber of layer 2 in stack 3 of the super module which is inserted in slot 1. In addition, each volume can be identified by its unique volume ID, a five digit decimal number [TGe10].

5.2 Different Steps of the Calibration and Alignment Procedure

The calibration and alignment procedure is performed iteratively. In a first step, expected values of the calibration and alignment parameters are applied during the reconstruction, the so-called pass0 reconstruction. A drift velocity of 1.5 cm/µs, a uniform relative gain of 1 for each readout pad, and the ideal geometry are used.
The output of this pass0 reconstruction is used for the drift velocity calibration. The determined values of this calibration are stored in the `SMint OCDB`. As the drift velocity used during reconstruction is crucial for the performance of the reconstruction, a second reconstruction, the so-called pass1, is carried out. The previously created OCDB entry is accessed during this reconstruction. The output of pass1 is then used for the alignment

procedure and the gain calibration. The parameters for the chamber positions and the gas gain, which are determined during alignment and gain calibration, are also stored in the `SMint OCDB`. A pass2 reconstruction can be performed with the determined parameters of the gas gain and the chamber positions. Afterwards, the resolution of pass1 and pass2 can be determined.

5.2.1 Reconstruction of the Data

After a positive L1 trigger decision, a full read out of the TRD is performed. Therefore, the data collected by the FERO is shipped to the GTU, as explained in Section 3.3.2. This data consists mostly of the digitized signals measured by the readout pads, i.e. the ADC counts.
A set of data recorded between enabling and disabling the detector electronics for data taking is called run. A run usually covers several events (see below). Within each run the electronic configurations and the applied anode and drift voltages do not change.
A positive trigger decision starts the readout of the so called event. During a cosmic run, this is due to the assumption of a particle crossing the ALICE detector, respectively the TRD in stand-alone data-taking. During a collision, it is possible to trigger on specific particles created in the collision.
A reconstruction can be performed on the data. Thereby, the data is converted into various objects during the different steps of the analysis:
Within each time bin, signals which were most likely generated by the same particle and are therefore adjacent in space, build a cluster.
After the clusters are identified, the position where the particle has crossed the sensitive plane, the so-called space point, is determined. It consists of the three coordinates, their errors, and the index of the subdetector in which the space point was found.
From these space points, the possible trajectory of a particle, the so-called track, is reconstructed. Straight tracks are defined by five parameters, which are the three coordinates of one point of the track and its angles θ and ϕ in the global ALICE coordinate system. Tracks with a helix shape are defined by their curvature, slope, phase, and the coordinates of one point of the track. In addition, the covariance matrices are determined.
The output of the reconstruction is saved in objects of type `Event Summary Data` (`ESD`) and stored in a file called `AliESDs.root`. Additional information, such as the clusters associated with the track, are stored in the file `AliESDfriends.root` .
During the reconstruction a data stream labeled `TRD.DebugTracker.root`, containing information about cluster, tracklets, and tracks, can be created. This data stream can for example be used to determine the detector resolution [Sic09] [His06].

5.2.2 Granularity Settings for the Calibration of Drift Velocity and Gas Gain

The values of the drift velocity and the relative gas gain can be determined for different granularities of the detector. Adjacent pads are summarized to calibration groups and their mean drift velocity or gas gain is determined. The size of the calibration group depends on two parameters. The number of columns in one calibration group is defined by nz and the number of rows by $n\Phi_\mathrm{r}$ (corresponding to z and Φ_r of the alignment coordinate system). nz and $n\Phi_\mathrm{r}$ are not the actual numbers of pads in each direction within one group. The settings are described below.
The largest possible granularity is the overall ALICE TRD, which is received with a setting of $(nz, n\Phi_\mathrm{r})$=(100,100). The calibration parameters of one individual super module can be determined with $(nz, n\Phi_\mathrm{r})$=(10,10). By setting the software to $(nz, n\Phi_\mathrm{r})$=(0,0), the calibration parameters of each single readout chamber are determined. For the smallest possible granularity, a pad-by-pad calibration, the settings $(nz, n\Phi_\mathrm{r})$=(4,6) can be used.
In Table 5.1 and Table 5.2 an overview of the possible calibration settings for a single chamber is given.
Figure 5.2 depicts the calibration group numbering for a C1 chamber with settings of $(nz, n\Phi_\mathrm{r}) = (2, 2)$. Thereby, every readout chamber is divided into 16 calibration groups.

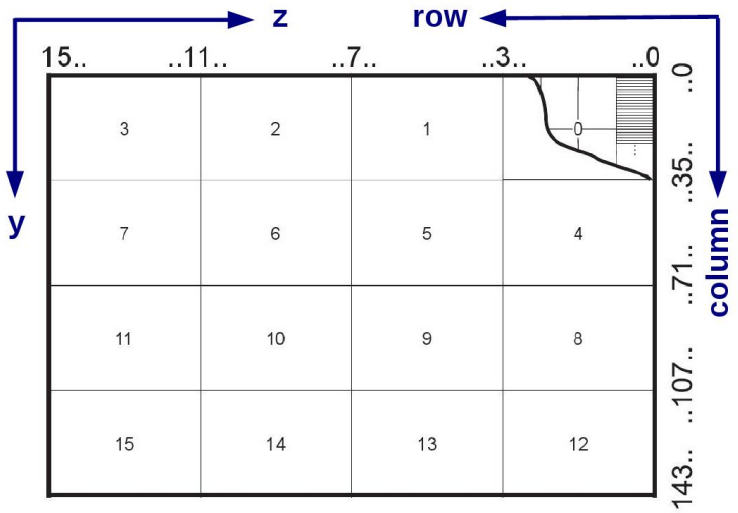

Figure 5.2: *Outline of the calibration groups of a C1 readout chamber with* $(nz, n\Phi_\mathrm{r}) = (2, 2)$ *settings. Here one calibration group comprises* 144 *pads (*4 *rows ·* 36 *columns). The MCMs and individual readout pads are indicated in the more detailed part in the upper right corner (c.f. [Alb10]).*

$n\Phi_r \hat{=}$ settings in column direction	number of calibration groups in column direction	number of columns per calibration group
0	1	144
1	2	72
2	4	36
3	8	18
4	16	9
5	36	4
6	144	1

Table 5.1: *Overview of calibration groups' dependence for one readout chamber on $n\Phi_r$ (cf. [Bai08]).*

$nz \hat{=}$ settings in row direction	number of calibration groups in row direction		number of rows per calibration group	
	C1 chamber	C0 chamber	C1 chamber	C0 chamber
0	1		16	12
1	2		8	6
2	4		4	3
3	6	8	2	
4	12	16	1	

Table 5.2: *Overview of calibration groups' dependence for one readout chamber on nz (cf. [Bai08]).*

5.2.3 Drift Velocity Calibration of TRD Super Modules

The drift velocity used during reconstruction has a direct influence on the determined x-position of a particle. A falsely assumed drift velocity leads to a wrong reconstruction of the x-position (see Equation 4.2). Therefore, using a precisely determined drift velocity during reconstruction is essential for further analysis performed on this run.

In the first step of the calibration procedure, the pulse height spectra are filled for each calibration group. Afterwards, the values of the drift velocity are determined from them.

Filling of the Pulse Height Spectra

After choosing the granularity, nz and $n\Phi_r$ are passed to a macro called `runTask2.C`. This macro then starts the macro `AliAnalysisTaskTRDCalib.cxx`. The pulse height spectra are filled for each calibration group of the detector by using the class `AliTRDCalibraFillHisto`. Figure 5.3 depicts an example of those spectra. The y-axis shows the time in µs. The x-axis corresponds to the calibration groups. Projecting the spectra to the x-axis gives the pulse height plot. A file named `TRDCalibration.root` contains the determined spectra, which comprise all information needed to determine the drift velocity.

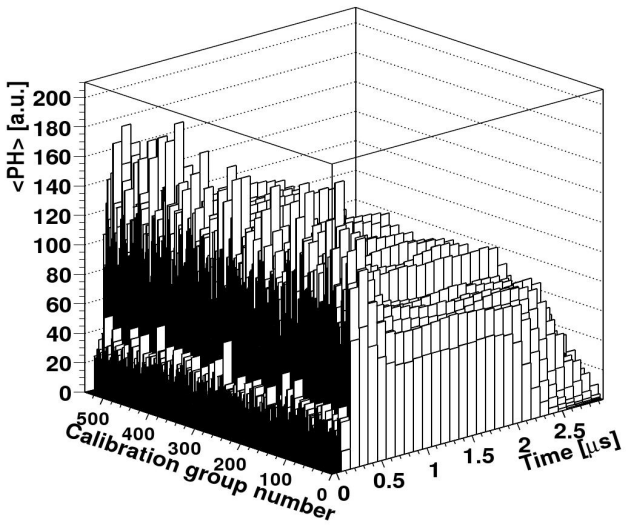

Figure 5.3: *Simulation of the average pulse height $\langle PH \rangle$ for the whole TRD. In this plot each calibration group corresponds to one readout chamber [Bai08].*

Determination of the Drift Velocity

A macro called `determineCoeff.C` is used to determine the values of the drift velocity from the spectra stored in `TRDCalibration.root`. The classes `AliTRDCalibraFit`, `AliTRDCalibraVector`, and `AliTRDCalibraMode` are used during this procedure.

The mean drift velocity can be calculated by dividing the length of the drift region Δs by the time it takes the electrons to travel through this region Δt:

$$V_{\text{drift}} = \frac{\Delta s}{\Delta t} = \frac{3 \text{ cm}}{t_{\text{D}} - t_{\text{A}}}. \tag{5.1}$$

In this equation, Δs corresponds to the distance between drift electrode and cathode wires. t_{A} denotes the time at which the signal is not due to electrons in the amplification region any more, but to electrons in the drift region. t_{D} represents the time at which the signal is not created by electrons in the drift region any more.

The times corresponding to the start and end of the amplification and drift region can be identified in the pulse height spectra in the following way:

- The first peak in the spectra is due to the signal of ionization electrons from both sides of the anode wires. Thus, it indicates the amplification region, which starts with the starting of the signal at a time t_0.
  The precise knowledge of t_0 is not obligatory for a calculation of the drift velocity. Nevertheless, it is used in the following as one of the criteria to determine the success of the calibration.
- The amplification region ends with the maximum of the peak at the time t_{A}. The part of the amplification peak after its maximum is an effect of the time response of the detector and does not belong to a signal created in the amplification region.
- Thereafter, a flat plateau corresponds to the drift region, which ends at the time t_{D}. As the result of the time response function, a long ion tail can be seen at the end of the signal.

t_0, t_{A}, and t_{D} have to be determined with a precision better than 1 time bin. Therefore, the time bins which contain them are determined first. Afterwards, their values are interpolated between time bins by using Lagrange polynomial functions. For n points consisting of the time and its corresponding pulse height $(t_i, \langle PH \rangle(t_i))$, only one polynomial function $P(t)$ of degree $n-1$ exists, which goes through the points:

$$P(t) = \sum_{i=1}^{n} \langle PH \rangle(t_k) \cdot \prod_{i \neq k} \left(\frac{t - t_i}{t_k - t_i} \right). \tag{5.2}$$

$P(t)$ is calculated for three points around t_A and for four points around t_0 and t_D each. To derive t_A, the maximum of the polynomial has to be determined by calculating the point, at which the polynomials first derivative has a value of zero. t_0 and t_D are identified by the point, at which the first derivative of the polynomial has its maximum, respectively minimum. Hence, the second derivative has a value of zero at this point.

Figure 5.4 shows a simulation of the average pulse height $\langle PH \rangle$ for $\pi^\pm$ at 1 GeV. The red lines indicate the determined t_0, t_A, and t_D.

It was found that this procedure does not always succeed. Therefore, the following criteria have been implemented to assure a reasonable result for the determined values of the drift velocity:

- The statistical error of the signal $E(\langle PH \rangle(t))$ has to be smaller than the actual variation of the signal. Hence, the signal within one time bin has to be larger than or equal to the signal in the previous (or following) time bin plus its error. This leads to conditions like the following:

$$\langle PH \rangle(t_\mathrm{A}) \geq \langle PH \rangle(t_\mathrm{A} - 1\mathrm{timebin}) + E(\langle PH \rangle(t_\mathrm{A} - 1\mathrm{timebin})) \tag{5.3}$$

$$\langle PH \rangle(t_\mathrm{A}) \geq \langle PH \rangle(t_\mathrm{A} + 1\mathrm{timebin}) + E(\langle PH \rangle(t_\mathrm{A} + 1\mathrm{timebin})). \tag{5.4}$$

- t_0 and t_D should not be the limit of the signal (first and last time bin), as the interpolation would fail.

- The start of the signal should not coincide with the end of the amplification region:

$$t_0 < t_\mathrm{A}. \tag{5.5}$$

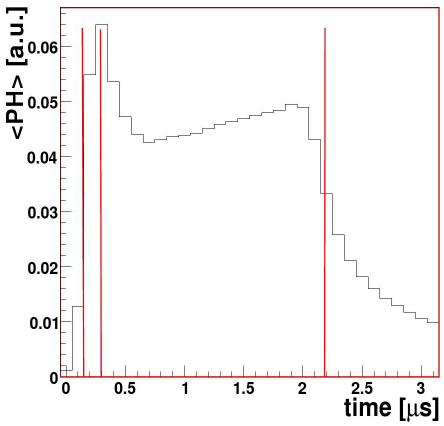

Figure 5.4: *Simulation of the average pulse height $\langle PH \rangle$ for $\pi^\pm$ at 1 GeV. The vertical red lines represent the determined t_0, t_A, and t_D [Bai08].*

For each pad, the drift velocity is stored in an OCDB, as described in Section 5.1.1. If the statistics were not sufficient or the determination of the values did not succeed, the default value of 1.5 cm/µs is assumed for the pads of the group.

5.2.4 Alignment of TRD Super Modules

Alignable Volumes

As described in Section 5.1.2, the geometry of ALICE uses a mother-daughter concept. Each daughter volume can be aligned with respect to its mother volume. For the TRD this means that, for example, every chamber can be aligned to its mother stack. The whole stack can then be aligned to the super module, which can be aligned to the overall detector system. Moreover, different daughter volumes can be aligned to each other within the mother volume, i.e. different stacks can be aligned to each other within the super module.
The super modules are assembled "one at a time" and are operated in a stand-alone mode, before being installed in ALICE. With the cosmic-ray data recorded after assembly, alignment of chambers within one stack can be performed. The alignment of the whole super module to the overall ALICE detector system has to be performed after installing the modules in ALICE.

Alignment Constants

The alignment procedure determines the deviations between the ideal geometry and the real position of the alignable volumes. In order to be able to describe every possible position and orientation of the detector components, six parameters, the alignment constants, are required. These constants are determined in the global ALICE coordinate system, using three shifts along the axes x, y, and z and three rotation angles ψ (for the rotation around the x-axis), ϑ (for the rotation around the y-axis), and φ (for the rotation around the z-axis). Afterwards, they are converted to the local alignment coordinate system, which is introduced in Section 3.5.3 and uses the axis Φ_r, z, and r.
The three shifts along these axis and the three tilts around these axes are depicted in Figure 5.5.

Alignment Procedure

As described before, during the alignment procedure, the daughter volumes are aligned to their mother volume. After assembly, the super modules are operated in stand-alone mode detecting cosmic rays in Münster. With these data, an alignment of chambers within one stack is performed iteratively. Thereby, the super module stacks serve as mother volume. The readout chambers within a stack are aligned one at a time.

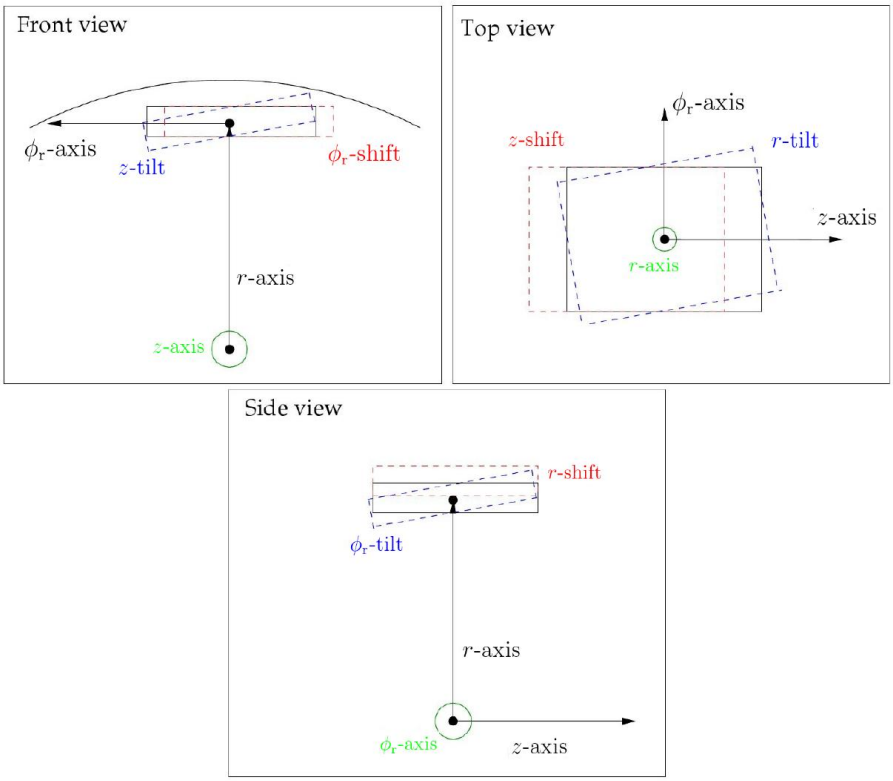

Figure 5.5: *Sketch of the alignment constants. Upper left panel: Front view of alignable volume indicating Φ_r-shift and z-tilt. Upper right panel: Top view of alignable volume indicating z-shift and r-tilt. Bottom panel: Side view of alignable volume indicating Φ_r-tilt and r-shift [Sic09].*

For alignment purposes, the tracks are converted into a set of space points and stored in an `AliTrackPoint` array. A macro called `PointSelector.C` is used for this purpose. The PointSelector not only converts the reconstructed data, but also allows to select the space points by different criteria. For example, cuts on the minimum number of tracklets associated with a track or the maximum allowed difference between the angles of a tracklet and its track can be performed.

Afterwards, the actual alignment can be performed by using a macro called `align_volume.C`. For each set of space points, a track is fitted through all space points, except the one located in the chamber that is about to be aligned. The difference between the position of the space point inside this chamber and the fitted track is determined for each set of space points. These differences are then minimized by varying the position and orientation of the chambers. The new position and orientation are described by the six alignment constants with respect to the ideal geometry. After these parameters are determined for each chamber, the second iteration is performed: Anew, tracks are fitted through the five chambers. But this time, alignment constants determined in the previous

step are taken into account when fitting the space points. Again, the differences in position are determined and thereby improved alignment constants are derived.
To prevent the stack from rotation or tilting, all alignment constants of layer 0 and layer 5 are fixed to a value of zero.
As shown in [Sic09], 30 iterations using 2000 tracks each, are needed to provide stable results of the alignment. After 30 iterations with 2000 tracks the constants reach saturation. Hence, these values are used during the alignment analysis performed as part of this thesis.
The used datasets are improved by cuts, performed by the `PointSelector`. Only tracks containing six tracklets were used. Moreover the difference in angle between the tracklet and track has to be less than 5° [Sic09].

5.2.5 Verification of the Alignment and Drift Velocity Calibration

The success of the alignment and drift velocity calibration procedure leads to an improvement of the detector resolution. The more precise the calibration parameters used during reconstruction are, the better the position resolution will be.
An improvement of the resolution can be seen in an increase of the cluster resolution. This resolution is determined by calculating the width of the distribution of deviations between clusters and the track they belong to. The cluster resolution depends not only on the precision of the tracking procedure, but also on the intrinsic detector resolution.
The sensitivity of the cluster resolution varies for the different calibration parameters and the different directions of the resolution. The resolution in x-direction (perpendicular to the pad plane) is sensitive to the value of the drift velocity, which is applied during reconstruction (see Section 4.4.2). Hence, the accuracy of the drift velocity can directly be monitored by changes in the resolution in x-direction.
As described in Section 3.3.1, the readout pads are much larger in z-direction than in y-direction. The resolution in z-direction is less significant for the detector performance and therefore not monitored in the following analysis. The resolution in y-direction is dominated by the precision of the presumed detector position, and therefore depends strongly on the alignment [Sic09].

Calculation of the Cluster Resolution in x- and y-Direction

In first approximation, the cluster resolution in x-direction σ_{x} is not influenced by the inclination of the track. In contrary, the cluster resolution in y-direction $\sigma_{\mathrm{y\text{-}combined}}$ is a

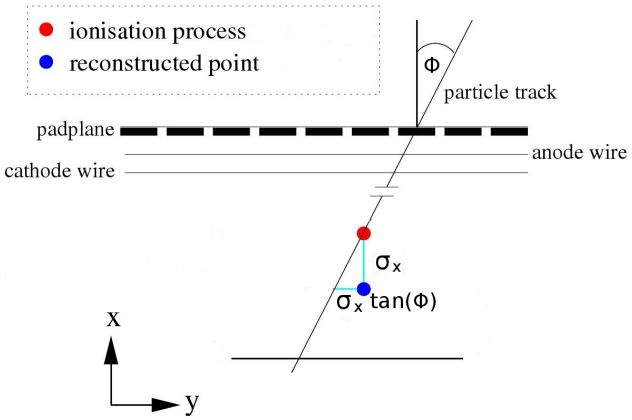

Figure 5.6: *Influence of σ_x on the resolution in y-direction, depending on the angle ϕ (c.f. [Wul09]).*

function of the angle ϕ. $\sigma_{\text{y-combined}}$ depends on the cluster resolution in y-direction at $\phi = 0°$ (σ_{y}) and on σ_{x} [Sic09]:

$$\sigma_{\text{y-combined}}(\phi) = \sqrt{\sigma_{\text{x}}^2 \cdot \tan^2 \phi + \sigma_{\text{y}}^2}. \tag{5.6}$$

The Influence of σ_{x} and the track angle ϕ on the resolution in y-direction is shown in Figure 5.6.

By obtaining the function $\sigma_{\text{y-combined}}(\phi)$, σ_{x} and σ_{y} can be calculated. The function $\sigma_{\text{y-combined}}(\phi)$ is obtained in the following way:
The cluster resolution in y-direction can be determined from the distribution

$$dy = y_{\text{cluster}} - y_{\text{track}}. \tag{5.7}$$

The width of this distribution is the same as $\sigma_{\text{y-combined}}$ integrated over all track angles. To obtain detailed information about the cluster positions a TTree[6] `MakeSeeds1`, stored in a file called `TRD.DebugTracker.root`, can be used. `MakeSeeds1` is generated at an early stage of reconstruction. At this stage, the tracking efficiency is relatively high, as many tracks are rejected at later steps of the reconstruction. Hence, the usage of `MakeSeeds1` allows to apply customized cuts on the unfiltered cluster. In the following analysis, these cuts are a maximum allowed curvature of the track of 0.05 m^{-1} and a number of six tracklets attached to each track [Sic09].

Figure 5.7 shows the residuals of dy. Projections to the vertical axis are performed for each bin within a given slice of ϕ. One of these projections is depicted in Figure 5.8.

[6] TTree is a tree data structure used by the ROOT framework. A tree is a data structure, which emulates a hierarchical tree structure containing of a list of independent branches that each have their own definition and list of buffers [ttr10].

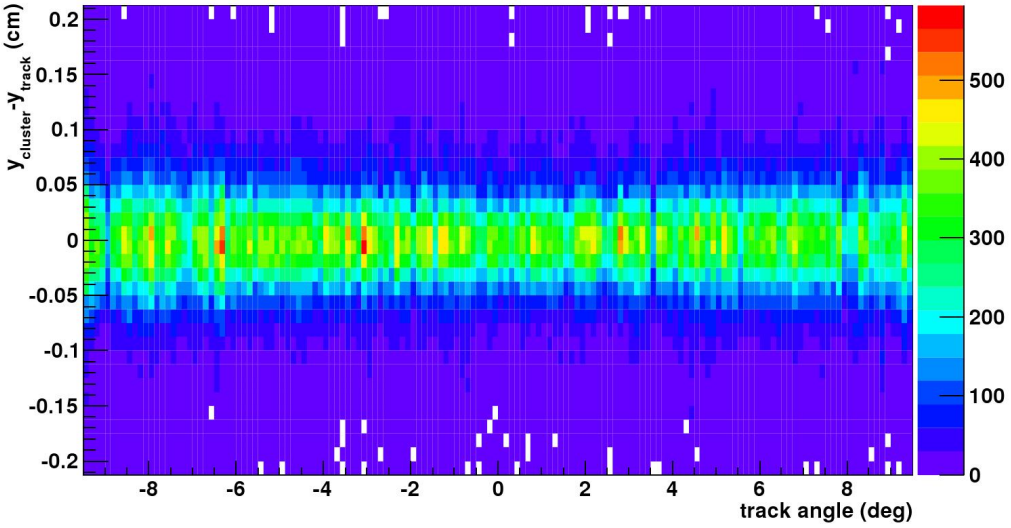

Figure 5.7: *Distribution of* $dy = y_{cluster} - y_{track}$ *as a function of the track angle* ϕ *for super module VI, run 1705.*

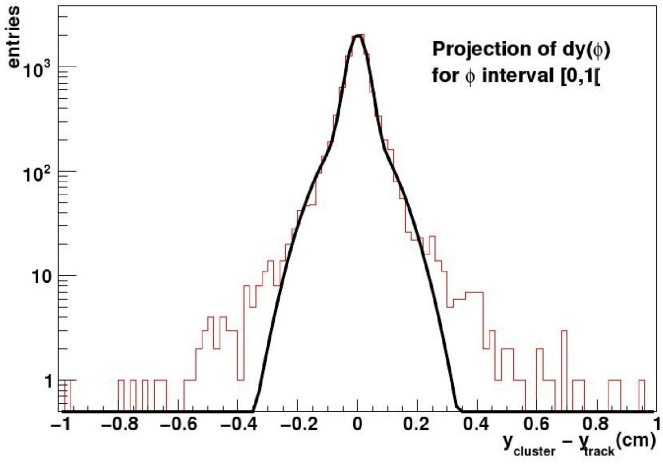

Figure 5.8: *Projection of dy to the vertical axis within the range of* ϕ*=[0,1[.*

These distributions are fitted with two Gaussian functions. The clusters belonging to the track are fitted with the first Gaussian function. As falsely attached clusters are not yet rejected, a second, broader Gaussian function is fitted to the background of the spectrum. The width of the inner Gaussian functions, representing $\sigma_{\text{y-combined}}$, are then plotted as a function of ϕ (see Figure 5.9). σ_{x} and σ_{y} are determined from this distribution. Therefore, Equation 5.6 is fitted to it, with ϕ being the argument and σ_{y} and σ_{x} the fit parameters. For the absence of a magnetic field, the minimum of the distribution should be located around 0^{o}.

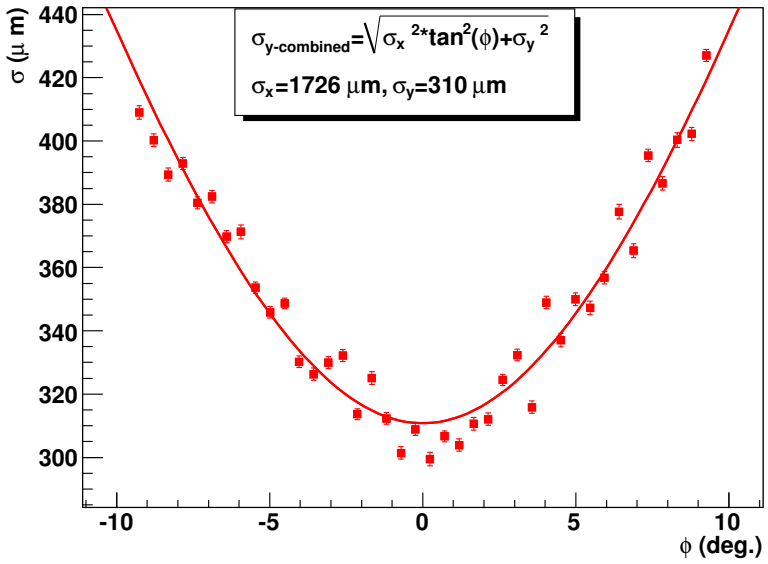

Figure 5.9: *$\sigma_{y\text{-}combined}$ as a function of ϕ for super module VI, run 1705.*

5.2.6 Gain Calibration of TRD Super Modules

Precise knowledge about the gas gain of the TRD is crucial for an efficient performance of the detector. After assembly, the gas gain can be determined with cosmic data recorded in Münster.
The gain calibration is performed iteratively and determines the relative gain either in comparison to the ideal gain factor of $g = 1$, or to previously determined gain factors. This approach allows to monitor changes in the gain over time. Moreover, a suppression of systematic errors and uncertainties is achieved.

The first step of the calibration procedure is to fill the dE/dx spectra for each calibration group. Afterwards the relative gain factors can be retrieved from it.

Filling of the dE/dx Spectra

As with the drift velocity calibration, the chosen values of nz and $n\Phi_r$ are passed to `runTask2.C`, which then starts `AliAnalysisTaskTRDCalib.cxx`. First the dE/dx distribution is filled for each calibration group. For this purpose, the energy loss per unit length traveled is determined from information stored in the ESDs during reconstruction. The class `AliTRDCalibraFillHisto` is used for this purpose. Figure 5.10 shows a dE/dx spectrum with granularity settings of $(nz, n\Phi_r)$=(0,0) for one super module.
As outlined in Section 3.3.1, the angle of the particle with respect to the sensitive plane influences the amount of energy loss. Within ALICE, this means particles with a flat polar angle θ, for example when crossing stack 0 or stack 4, deposit more energy in the gas, as they traverse a larger distance in the detector. This is taken into account by determining the track angle and correcting the dE/dx spectra.
Gain factors of either the default `OCDB` values or previously determined ones are taken into account when reconstructing the data. These gain factors influence the output of the reconstruction. As the calibration is performed on the basis of this output, the used gain factors have to be considered. Therefore, a path to the `OCDB` which was used during reconstruction has to be declared during the calibration.
The determined spectra contain all further information needed (see Figure 5.10). The y-axis corresponds to the calibration group, the x-axis shows the energy loss distribution. Projecting the spectra to the x-axis gives the dE/dx distribution. As with pulse height spectra of the drift velocity, the determined spectra for the gain calibration are stored in a file called `TRDCalibration.root`.
It is possible to determine a slightly different dE/dx spectrum by considering only time bins belonging to the drift or to the amplification region, when a second or third calibration is performed. Nevertheless, for a first calibration after pass0, as performed in this thesis, the whole signal is taken into account.

Determination of the Relative Gain Factors

As with the drift velocity calibration, `determineCoeff.C` processes `TRDCalibration.root` to calculate the gain factors. Again, the classes `AliTRDCalibraFit`, `AliTRDCalibraVector`, and `AliTRDCalibraMode` are used.
As outlined in Section 3.4.3, the distribution of the energy loss is Landau shaped. The gas gain can be characterized by its Most Probable Value (MPV). The MPV is, in contrast to the mean of the distribution, little influenced by the long ion tails.
Various methods, differing in accuracy and needed CPU time, are implemented for the gain calibration. After verification with simulated data, weighted mean was chosen as default method. It provides the second best accuracy together with shortest CPU time needed and moreover best stability. In this method the dE/dx distribution is transfered

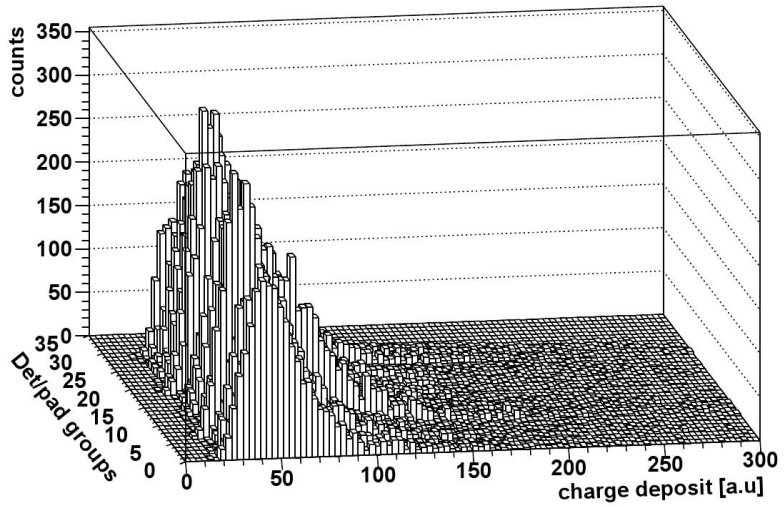

Figure 5.10: *Plot of the dE/dx spectra of super module II run 1899 with each chamber being one calibration group [Alb10].*

to a function $N(\Delta E)$. Here $N(\Delta E)$ represents the number of tracks which corresponds to the number of particles that have deposited the energy ΔE in the chamber. The weighted mean M_{w} is defined as:

$$M_{\mathrm{w}} = \frac{\int_0^{\Delta E_{\max}} f_{\mathrm{w}}(\Delta E) \cdot N(\Delta E) \cdot \Delta E \cdot \mathrm{d}\Delta E}{\int_0^{\Delta E_{\max}} f_{\mathrm{w}}(\Delta E) \cdot N(\Delta E) \cdot \mathrm{d}\Delta E} = \frac{\sum_i f_{\mathrm{w}}(\Delta E_i) \cdot N(\Delta E_i) \cdot \Delta E_i}{\sum_i f_{\mathrm{w}}(\Delta E_i) \cdot N(\Delta E_i)}. \tag{5.8}$$

In this equation $\Delta E_{\max}$ denotes the highest energy deposition in the gas and $f_{\mathrm{w}}(\Delta E_i)$ the positive weight function with $0 \leq f_{\mathrm{w}}(\Delta E_i)$. Due to the definition of the weighted mean, only the relative values of the weight function influence the value of M_{w}. Thereby, $k \cdot f_{\mathrm{w}}(\Delta E)$, with k being a positive constant, leads to the same results of M_{w} as $f_{\mathrm{w}}(\Delta E)$. The mean energy loss is given by M_{w} if $f_{\mathrm{w}}(\Delta E)$=const=1.
The weight function has to be determined once from a typical dE/dx spectrum in the following way:
A function $f_r(\Delta E)$ is parametrized with 5 values a, b, c, d, and e to

$$f_{\mathrm{w}}(\Delta E) = a + b \cdot f_r(\Delta E) + c \cdot (f_r(\Delta E))^2 + d \cdot (f_r(\Delta E))^3 + e \cdot (f_r(\Delta E))^4. \tag{5.9}$$

$f_r(\Delta E)$ is defined as

$$f_r(\Delta E) = \frac{\int_0^{\Delta E} N(\Delta e)\mathrm{d}\Delta e}{\int_0^{\Delta E_{\max}} N(\Delta e)\mathrm{d}\Delta e} = \frac{\sum_{i=bin(0)}^{bin(\Delta E)} N(\Delta e_i)}{\sum_i N(\Delta e_i)} \tag{5.10}$$

and can have values between 0 and 1.
An energy loss value ΔE is chosen. The number of particles depositing an amount of energy lower or equal this value is determined and divided by the total number of particles. This

is done for all possible energy deposits ΔE (see Equation 5.10). $f_r(\Delta E)$ in Equation 5.9 is then substituted by Equation 5.10. The result of this finally substitutes $f_{\mathrm{w}}(\Delta E)$ in equation 5.8. The parameters a, b, c, d, and e are then adjusted to achieve the same result of M_{w} as for MPV with a convolution of Landau distribution and Gaussian fits.
This weighted mean function has been determined and is stored in an AliRoot class. In order to achieve an acceptable error for the determined gain factors of $\sigma_{\mathrm{rel}} < 2\%$, at least 1000 tracklets have to be reconstructed for each calibration group.
The gain factors determined by `determineCoeff.C` are then stored for each pad in an `OCDB`, as described in Section 5.1.1 [Bai08], [Alb10].

6. Executing the Calibration and Alignment Procedure

All macros and objects needed for the calibration and alignment procedure are located in a folder named `run_calibration` on a computer cluster called MAF, which is used by the university of Münster. This folder contains subfolders for the different tasks such as `pass0`, `pass1`, `pass2`, `v_drift`, `alignment`, `gas_gain`, and `resolution`. It also includes a subfolder `fake_objects` comprising objects needed during the calibration. Moreover, in a subfolder `default_OCDB`s several OCDBs with different drift velocities or general information for each run, i.e. about the starting time of a signal (`ChamberT0`), are stored. The `SMint OCDB` is also located in the folder `/data8/run_calibration` on a data disk called `data8`.
The calibration and alignment of a super module should be performed in the following order:

1. Pass0 reconstruction
2. Calibration of the drift velocity
3. Pass1 reconstruction, during which the determined drift velocity is applied
4. Calibration of gas gain and determination of alignment constants
5. If necessary for further analysis: pass2 reconstruction, during which all determined parameters are applied

In the following, the calibration procedure will be described using the example of run 2410 of super module VIII. The output of the calibration procedure is stored in a folder `/data8/run_calibration/SMs`. The folder `SMs` contains subfolders for the different super modules (`/data8/run_calibration/SMs/SM8`[1]) and runs (`/data8/run_calibration/SMs/SM8/run2410`).

6.1 Pass0 Reconstruction

The first step of the calibration procedure is the pass0 reconstruction. A folder named `/data8/run_calibration/pass0` contains all macros needed for the reconstruction of pass0.

[1]The number 8 refers to the numbering convention corresponding to the order of first assembly, even though Arabic numerals are used at this point.

Before starting the reconstruction, settings in the macro `start_pass0.sh` have to be adjusted to the specific run which is about to be reconstructed. In the first lines of the macro the super module number (`sm=8`) and the run number (`run=2410`) have to be changed. Moreover, it can be selected how many files of the run will be reconstructed (`file=1`, `fileend=10`). After applying the correct values, the reconstruction can be executed with the command **./start_pass0.sh**.

Subfolders for the super module, the run, pass0, and the files which are about to be reconstructed (`/data8/run_calibration/SMs/SM8/run2410/pass0/file001`) are created, if they do not yet exist.
The reconstruction is performed on intervals of 2500 events each. To reconstruct a whole file, the events 0-2500, 2500-5000, and so on are reconstructed, until the end of the file is reached. For each interval, `start_pass0.sh` creates a job by submitting an executable macro to the batch server[2]. Among other tasks, this macro executes the actual reconstruction macro.
The resolution of the detector will be determined from the first two files of a run. Therefore, the macro submitted for these two files is slightly different as the macros submitted for the other files.
From file number three on, `start_pass0.sh` submits the macro `pass0_tmp.sh`. It creates a folder for its interval (`/data8/run_calibration/SM8/run2410/pass0/file001/05000to07500`) and starts the actual reconstruction, using the reconstruction macro `rec.C`. The standard output and standard error[3] are recorded in the files `outREC.bz2` and `errREC.bz2`. All output of the reconstruction is stored in the folder of the interval.
For the files 0 and 1 a macro named `pass0_resolution_tmp.sh` is submitted for each interval of these two files. A folder is created in the same way as with `pass0_tmp.sh`. The reconstruction macro `rec_residuen.C` is then executed. It performs a reconstruction similar to `rec.C`, but additional information about clusters are streamed to a file `TRD.DebugTracker.root`. Standard and error outputs created by `rec_residuen.C` are streamed to the files `outRES.bz2` and `errRES.bz2`. After the reconstruction is finished, the distribution $dy = y_{\text{cluster}} - y_{\text{track}}$ is determined. A macro called `cluster_track_func_improved.C` is used for this purpose. The obtained distribution is stored in a file called `hwzgood.root`. Files labeled `outCTF.bz2` and `errCTF.bz2` contain the standard output and standard error of `cluster_track_func_improved.C`.

[2]Macros submitted to the batch server are stored until they are executed once, at a time when enough CPU is available by the computer cluster.
[3]The standard output (error) is a stream of the text output (or error messages) of a program.

The reconstruction of one interval of the first two files takes roughly 1 hours 40 minutes, which leads to about 4 CPU-days per file. The reconstruction of one interval without recording informations concerning resolution measurements takes about 1 hour 20 minutes, hence a whole file is reconstructed in about 3.5 CPU-days.

6.2 Drift Velocity Calibration

After all data is reconstructed, the drift velocity can be determined. The macros needed for this procedure are located in the folder `/data8/run_calibration/v_drift`. Before executing the calibration, settings in the macro `start_vdrift.sh` have to be adjusted to the specific run that shall be analyzed. The settings for the super module number (`sm=8`), the run number (`run=2410`), and the files which will be analyzed (`file=1`, `fileend=10`) have to be the same as in `start_pass0.sh`. Moreover, the granularity settings can be adjusted (`nz=0`, `nPhi_r=0`). As described in Section 5.2.3, for pads in calibration group with too low statistics, the default value $V_{\text{drift}} = 1.5$ cm/µs is stored in the OCDB. This default value might have a large difference to the actual value of the drift velocity. As the values stored in the OCDB are used during the pass1 reconstruction, it is recommended to use a granularity that ensures sufficient statistics in every calibration group. A chamberwise calibration (settings `nz=0`, `nPhi_r=0`) has been proven reasonable.
After the values of the macro are adjusted, the calibration procedure can be started with the command **./start_vdrift.sh**.

The macro `vdrift_tmp.sh` is submitted to the batch server. First, a list named `run2410.txt` of all `AliESDs.root` and `AliESDfriends.root`, which were successfully created during pass0, is created. A macro `CreateTextFileESD.C` is used for this purpose. This list is then passed to `runTask2.C`, which fills the pulse height spectra and stores them in the file `TRDCalibration.root`. The standard and error output are stored in files labeled `outRT.bz2` and `errRT.bz2`. Afterwards, the macro `determineCoeff.C` retrieves the values of the drift velocity by processing `TRDCalibration.root`. The files `outDC.bz2` and `errDC.bz2` contain the standard and error output of this procedure. The determined values are stored in a local OCDB.
All output of the drift calibration, including the created OCDB, is moved to a newly created folder `/data8/run_calibration/SMs/SM8/run2410/v_drift`. A copy of the OCDB entry is stored in the SMintOCDB.

6.3 Pass1 Reconstruction

The determined drift velocity values allow for an improved reconstruction, the so-called pass1. The macros for this reconstruction are located in a folder named `/data8/run_calibration/pass1`. Before starting the procedure, the same parameters have to be adjusted in the macro `start_pass1.sh`, as previously in `start_pass0.sh`. Thereafter, the reconstruction can be executed with the command **./start_pass1.sh**.

Subfolders for pass1 and the different files, which are about to be reconstructed, are created (`/data8/run_calibration/SMs/SM8/run2410/pass1/file001`). All output of pass1 will be stored in these subfolders. The reconstruction procedure is similar to the one of pass0. As the only difference, not the default drift velocity of 1.5 cm/µs, but the values previously stored in the `SMint OCDB` are used.

6.4 Gain Calibration

During the gain calibration procedure dE/dx spectra are created, from which the gain factors are determined. As the reconstructed x-position is highly dependent on the drift velocity, the gain calibration should only be performed with the output of the pass1 reconstruction. The macros which perform the gain calibration are located in a folder named `gain_calibration`. First, settings of the macro `start_gain.sh` have to be changed. The super module number (`sm=8`) and the run number (`run=2410`) have to be altered. Moreover, the desired shape and size of the calibration groups has to be chosen by the settings which control the numbers of rows and columns in each group (`nz=3`, `nPhi_r=4`). Section 5.2.2 gives an overview of the possible settings. Thereafter, the calibration procedure can be started with the command **./start_gain.sh**.

The job submitted to the batch server is `gain_tmp.sh`. By using the macro `CreateTextFileESD.C`, the paths to all `AliESDs.root` and `AliESDfriends.root`, which were successfully created during pass1, are stored in a list named `run2410.txt`. This list is passed to `runTask2.C`, which determines the dE/dx spectra. These spectra are saved in a file `TRDCalibration.root`. Standard and error output of `runTask2.C` is streamed to files named `outRT.bz2` and `errRT.bz2`. In a next step, `determineCoeff.C` extracts the gain factors and stores them in a local OCDB. The files `outDC.bz2` and `errDC.bz2` contain the standard and error output of this step of the analysis. All output of the gain calibration is moved to a folder `/data8/run_calibration/SMs/SM8/run2410/gain`. In addition, the OCDB entry for the gain factors is copied to the `SMint OCDB`.

6.5 Alignment Procedure

As with the alignment procedure, the precision of the drift velocity, which is applied during reconstruction, influences the outcome of the alignment. Therefore, data of pass1 is processed in the alignment procedure.
The alignment procedure comprises two tasks. First the data has to be prepared for the alignment. Afterwards, the alignment constants can be determined by performing the actual alignment procedure.

6.5.1 Preparation for the Alignment: PointSelector

All macros needed for this step of the analysis are located in the folder `/data8/run_calibration/alignment/point_selector`. The settings of `start_selector.sh` have to be altered, to have them match the settings of `start_pass1.sh`. The procedure is started with the command **./start_selector.sh**.

A folder for the alignment and a subfolder named `/data8/run_calibration/SMs/SM8/run2410/alignment/point_selector`, in which all output of the current procedure will be stored, are created. For each file, a macro called `selector_tmp.sh` is submitted to the batch server. It executes another macro called `analyse_cut_intern.C`, which processes the macro `PointSelector.C` for each intervall of events.. Thereby, information about the tracks are determined from the `ALIESDfriends.root` and `AliESDs.root`, which were created during reconstruction. After applying several cuts, the tracks are converted into a set of space points. These space points are stored in an `AliTRackPoint` array and saved in a file called `AliTrackPoints.root`. The standard and error output of `analyse_cut_intern.C` is saved in the files `outANA.bz2` and `errANA.bz2`.

6.5.2 Determination of the Alignment Constants

In a second step, the alignment constants can be determined. For this purpose, macros located in `/data8/run_calibration/alignment/determine_constants` are used. Before executing the procedure, the settings in `start_constants.sh` have to be changed to the settings of `start_pass1.sh`. Afterwards the alignment constants can be retrieved by executing **./start_constants.sh**.

A folder `/data8/run_calibration/SMs/SM8/run2410/alignment/constants` is created and a macro `align_tmp.sh` is submitted to the batch server. This job first merges all the previously determined `AliTrackPoint` arrays together and stores the output in

a file `AliTrackPoints_complete.root`. This file is then processed by a macro called `align_intern.C`. The standard and error output is streamed to the files `outINT.bz2` and `errINT.bz2`. the macro `align_intern.C` executes 30 iterations of `align_volume.C` for each stack and stores the determined alignment constants in a file called `const_run2410.root`. The standard and error output of this procedure is saved in files labeled `outVOL.bz2` and `errVOL.bz2`. To create an entry in the `SMint OCDB` for this run, `create_alignment_OCDB.C` is executed. Files named `outOCDB.bz2` and `errOCDB.bz2` contain the received standard and error output. In the last step of the alignment procedure, a macro named `plot_align.C` creates a histogram of the determined alignment constants, and stores it in the file `constants_histo.root`. The created standard and error output of `plot_align.C` is streamed to files labeled `outPLOT.bz2` and `errPLOT.bz2`.

6.6 Pass2 Reconstruction

If it is intended to perform further analysis with a run, a pass2 reconstruction is recommended. During this reconstruction all previously determined parameters are taken into account. This pass2 reconstruction can be performed with the macros located in the folder `/data8/run_calibration/pass2`. Therefore, settings in the first lines of `start_pass2` have to be adjusted the same way as previously for the pass1 reconstruction. With the command **./start_pass2** the reconstruction procedure is initiated.

A folder `/data8/run_calibration/SMs/SM8/run2410/pass2`, which will contain the output of the pass2 reconstruction, is created. Thereafter, the procedure resembles the reconstruction procedure of pass0. But this time the determined drift velocity, alignment parameters, and gain factors are extracted from the `SMint OCDB` and used during reconstruction.

6.6.1 Comparison of the Resolution of pass1 and pass2

After the data is reconstructed, its resolution can be determined. The folder `/data8/run_calibration/resolution` contains macros for this purpose. First the settings of `start_resolution.sh` have to be adjusted. The number of the super module and the run number have to be changed. The resolution measurement can then be executed with the command **./start_resolution**.

A folder `/data8/run_calibration/SMs/SM8/run2410/resolution` is created. All output of the resolution procedure will be moved to this folder at the end. The macro `resolution_tmp.sh` is submitted to the batch server. In a first step, the information, which was stored in `hwzgood.root` during reconstruction of pass1 and pass2, is merged

together and stored in the respective files `hwzgood_pass1.root` and `hwzgood_pass2.root`. Macros called `Draw_w1.root` and `Draw_w2.root` then determine the residuals for different track angles by processing those files. The retrieved information is stored in a histogram in files labeled `plot_pass1.root` and `plot_pass2.root`. The standard and error output of `Draw_w1.root` and `Draw_w2.root` is streamed to files named `outDRAW1.bz2` and `errDRAW1.bz2` and `outDRAW2.bz2` and `errDRAW2.bz2`, respectively. For better visualization, the resolutions are plotted in one histogram. The is done by `read.C`, which also stores this histogram in the file `resolution.root`. Files called `outREAD.bz2` and `errREAD.bz2` contain the standard and error output, which were created while processing `Draw_w.root`.

7. Results of Calibration and Alignment

7.1 Results of the Drift Velocity Calibration

In this section, the influence of the applied anode voltage on the drift velocity and its effect on the residuals in x-direction are investigated.

As outlined in Section 4.4.2, the accuracy of the drift velocity, which is assumed during reconstruction, has an impact on the residuals in x-direction. This was investigated by analyzing run 2018 of super module I. The run was reconstructed 17 times, each time using a different drift velocity. Figure 7.1 shows the determined σ_{x} plotted vs. the used drift velocity. The expected dependence can clearly be seen. The extracted fit function is $y = 4893 \cdot x^2 - 25734 \cdot x + 39572$. The minimum of this function $x_0 = 2.6$ corresponds to the actual drift velocity 2.6 cm/µs of the electrons.

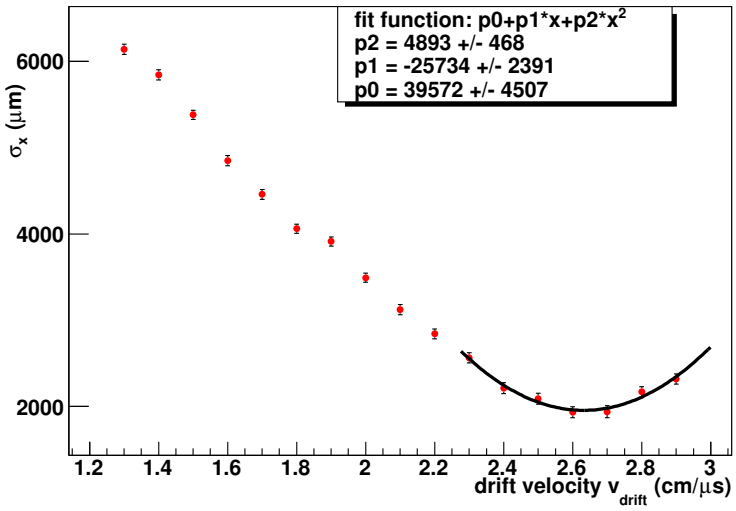

Figure 7.1: *σ_x as a function of the drift velocity, determined with data from super module I, run 2018. The error bars correspond to the error of the fit parameter σ_{x} when fitting $\sigma_{\mathrm{y-combined}} = \sqrt{\sigma_{\mathrm{x}} \cdot \tan^2 \phi + \sigma_{\mathrm{y}}^2}$.*

In a second analysis, the drift velocity was determined for runs with different drift voltages. The outcome of this calibration was compared to MAGBOLTZ simulations, which calculate the drift velocity by solving the Boltzmann transport equations for electrons under the influence of an electric field in a gas mixture. The result can be seen in Figure 7.2. The drift velocity is plotted vs. the electric field strength E. The squares correspond to experimentally determined drift velocities, the dots and the linear fits correspond to data simulated with MAGBOLTZ. The exact composition of the gas mixture was changed once. The blue square and the blue dots correspond to a mixture of Ar/CO_2 (83/17). The pink squares and red dots correspond to a mixture of Ar/CO_2 (82/18).

The pressure conditions inside the readout chamber are not exactly known, but estimated in the following way:
Münster lies about 60 m above sea level. The average atmospherical pressure p at the height h can be determined from the international height formula, a modification of the barometric formula [Dem06]:

$$p = 1013\,\text{mbar} \cdot e^{\frac{-h}{8.33\text{km}}} \tag{7.1}$$

$$p = 1013\,\text{mbar} \cdot e^{\frac{-0.060\text{km}}{8.33\text{km}}} \tag{7.2}$$

$$p = 1005,7\,\text{mbar} \tag{7.3}$$

The readout chambers are flushed with gas, which leads to a slightly larger pressure inside. Therefore, an average pressure of 1013,5 mbar was chosen for the simulations. The temperature of the gas was estimated to 300 K.

A linear dependence of the drift velocity on the electric field strength can be seen. The difference between measured and simulated drift velocity could be an effect of the imprecise knowledge of the gas composition. As can be seen, changing the mixture from Ar/CO_2 (83/17) to (82/18) leads to a difference in the drift velocity between 0.1 cm/µs and 0.2 cm/µs in the region of electric field strength, in which the TRD was operated. The results of measurement and simulation only show a difference of abut 0.05 cm/µs. A more detailed analysis of the drift velocity will be available soon in [Pop].

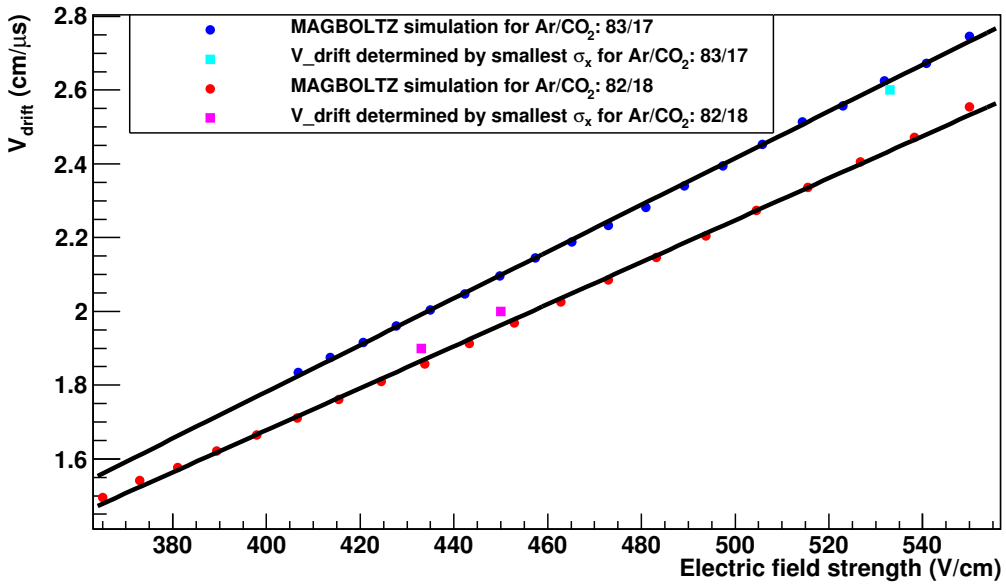

Figure 7.2: *Drift velocity for different electrical filed strengths determined with the smallest-σ_x-methode compared to MAGBOLTZ simulations at a pressure of* 1013.5 *mbar and a temperature of* 300 *K. MAGBOLTZ for AR/CO$_2$ (*82/17*): V_{drift} = 1.49 cm/µs at $E = 365$ V/cm. This corresponds to a drift voltage of* 1095 *V for the TRD.*

7.2 Results of the Alignment Procedure

In this section, the results of the alignment procedure are shown. First, the accuracy of the resolution determined by the method described in Section 5.2.5 is analyzed. Thereafter, the alignment constants are exemplarily depicted for super module VI. Moreover, the effect of the alignment constants on the resolution is investigated for the super modules VI, VII, VIII, and IX. For the super modules for which alignment constants could be derived from the central OCDB, their effect on the resolution is also studied.

7.2.1 Accuracy of Residual Measurements

To investigate the accuracy of the determined resolutions, run 2538 of super module IX was split into ten different datasets of 225000 events. For each dataset, a reconstruction was performed with the same settings and the residuals were determined. $\sigma_{\mathrm{y-combined}}$ will be stated σ in the following plots. Due to misalignment, the minimum of $\sigma_{\mathrm{y-combined}}$ is not located around $\phi = 0°$, but slightly shifted. Therefore, the dataset was fitted with the function $\sigma_{\mathrm{y-combined}} = \sqrt{\sigma_{\mathrm{x}}^2 \cdot \tan^2(\phi - \varphi) + \sigma_{\mathrm{y}}^2}$. Figure 7.3 shows the distribution of these residuals. $\sigma_{\mathrm{y\text{-}combined}}$ is plotted vs. the track angle ϕ.

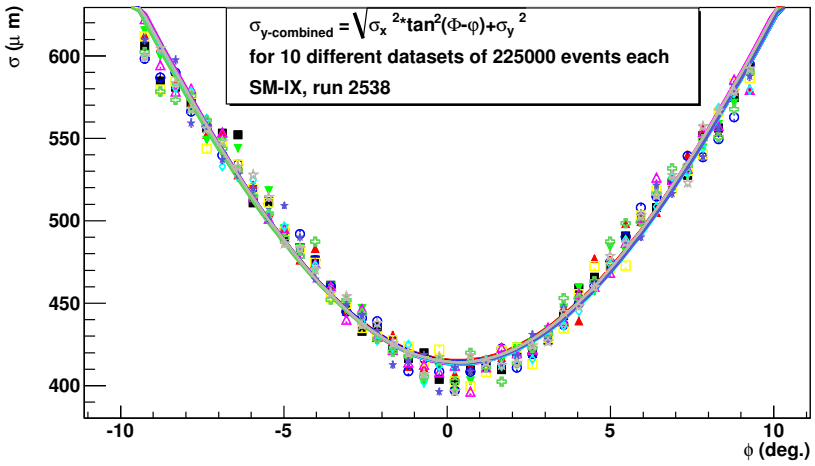

Figure 7.3: $\sigma_{\mathrm{y-combined}} = \sqrt{\sigma_{\mathrm{x}}^2 \cdot \tan^2(\phi - \varphi) + \sigma_{\mathrm{y}}^2}$ *for 10 different datasets, determined with data from super module IX, run 2538.* $\sigma_y = (413.9 \pm 0.75)\mu m$, $\sigma_x = (2746 \pm 11)\mu m$, $\varphi = (0.38 \pm 0.03)°$, *errors determined from RMS of the parameters.*

As can be seen, the results vary only slightly. The different fit values of σ_{y}, σ_{x}, and φ are shown in Figure 7.4.

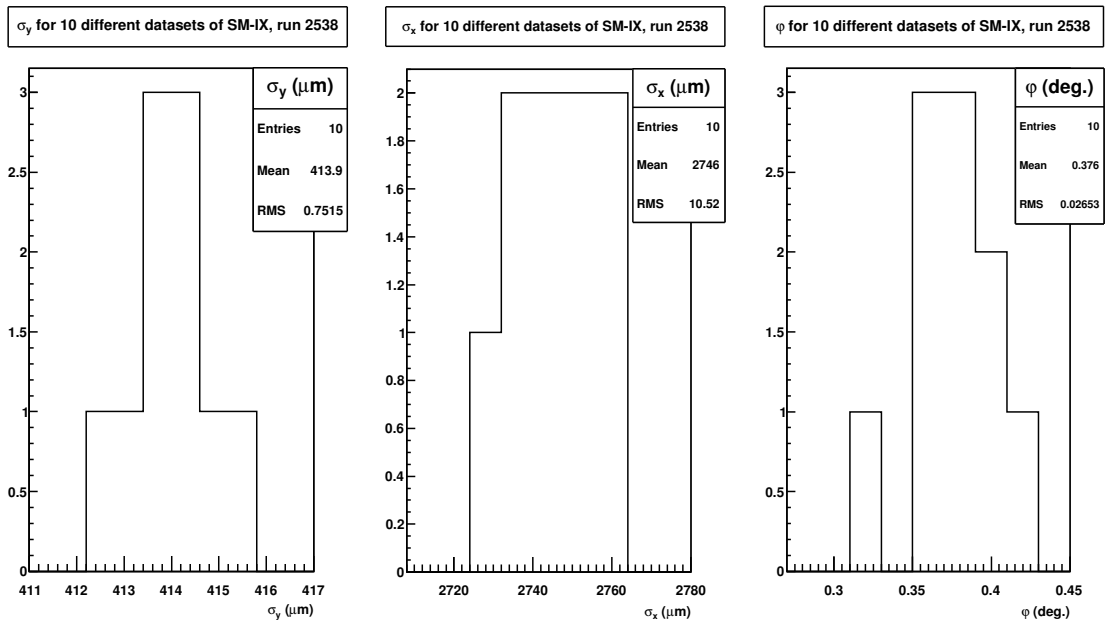

Figure 7.4: *σ_y for 10 different datasets, determined with data from super module IX, run 2538.*

In a next step, the errors ERRσ_y, ERRσ_x, and ERRφ, which were calculated during the fitting procedure, are investigated.
As mentioned above, run 2538 was split into ten different datasets. Even though the data was recorded over several hours, the electronic configurations, the gas mixture and flow, and the high voltage settings have not been changed manually during the run. Therefore, they should vary only slightly over time, and the error of the parameters σ_y, σ_x, and φ can be determined by the root mean square (RMS) of the parameters.
The RMS of the parameters was compared to the errors, that were calculated during the fitting procedure. Thereby, the accuracy of the errors was evaluated. Table 7.1 shows the outcome of those calculations compared to the mean of the fit errors.
It shows that the fit underestimates the error of φ by about 44.4%. σ_y and σ_x are most significant for the detector resolution. Their errors are underestimated by about 33.6% and 23.4%, respectively. Nevertheless, the error of the fit parameters will be used for the residual plots in the following.

RMS(σ_y)	mean of ERRσ_y	RMS(σ_x)	mean of ERRσ_x	RMS(φ)	mean of ERRφ
0.752 µm	0.499 µm	10.52 µm	8.06 µm	0.027°	0.015°

Table 7.1: *RMS of fit parameters and mean of the errors, which were calculated during the fitting procedure.*

7.2.2 Alignment Constants

The super modules I - VII are already installed at ALICE. Alignment constants for these super modules have been determined with data recorded at ALICE and can be accessed in the central OCDB.
As part of this thesis, alignment constants were determined for the super modules VI - IX with data recorded right after assembly in Münster. Figure 7.5 shows the distributions of these parameters at the example of super module VI. In each plot, the values of one alignment constant, e.g. ϕ_{r}-shift in the upper left panel, is plotted vs. the chamber number it was determined for. The chambers are numbered consecutively from 0 to 29, starting from stack 0 layer 4 to stack 4 layer 5. Chamber number 0 corresponds to stack 0 layer 0, chamber number 1 to stack 0 layer 1, chamber number 6 to stack 1 layer 0 and so on. The vertical lines indicate the stack borders. Blue dots correspond to constants determined in Münster, whereas the red squares correspond to constants extracted from the central OCDB. As described in Section 5.2.4, the alignment constants for layer 0 and layer 5 are fixed to a value of zero.
The mechanical construction of the super module limits the realistic range of the alignment constants. Shifts in r-direction should only occur for less than a millimeter. Nevertheless, for the different super modules constants of r-shift up to 4.4 mm were determined (all alignment constants are depicted in Chapter A of the Appendix). Also the peak values of r-tilt = 0.8° and ϕ_{r}-tilt = 0.4° are larger than expected. The reason for these unexpectedly high values is still under investigation. Moreover, the values of ϕ_{r}-tilt are almost always larger than zero, which is not yet understood. Due to these facts, those constants are fixed to a value of zero during the alignment procedure performed with data recorded at ALICE.
Nevertheless, such unrealistic values were allowed during the alignment procedure performed as part of this thesis, as they lead to a better resolution compared to the method performed with data recorded at ALICE (see Section 7.2.3).

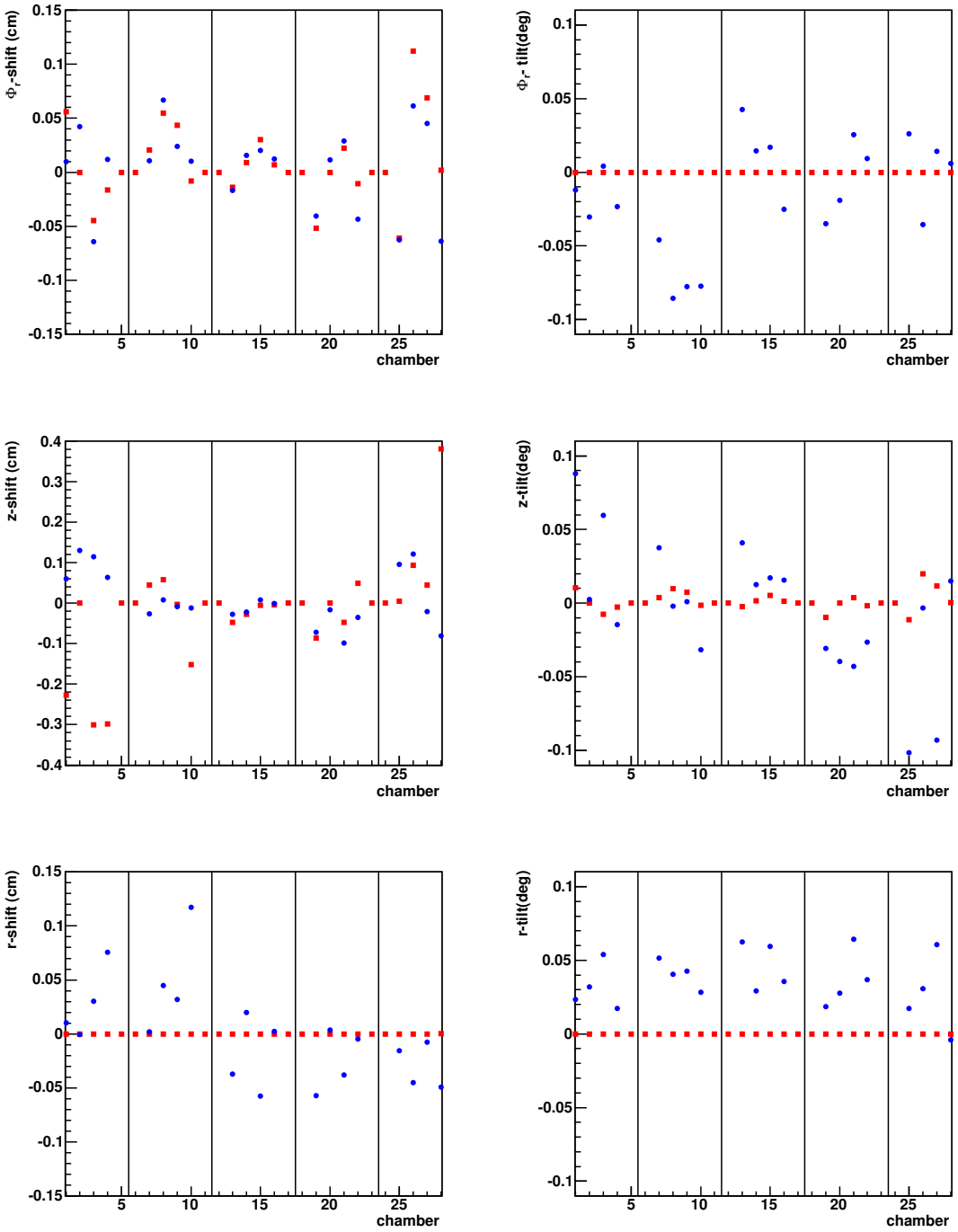

Figure 7.5: *Alignment constants of super module VI. Red squares correspond to constants determined with data taken at CERN. Blue dots correspond to constants determined with data taken in Münster.*

7.2.3 Residuals Before and After Alignment

The Figures 7.6 to 7.9 show the determined residuals for the super modules VI - IX. Black squares correspond to the residuals of pass1, during which no alignment constants were applied. Red triangles correspond to the residuals of a pass2 reconstruction, during which the alignment constants determined from data in Münster were used. The green triangles correspond to the residuals determined from a pass2 reconstruction, in which alignment parameters extracted from the central OCDB were used. The drift velocity determined from pass0 was applied during the reconstructions of pass1 and pass2. In each plot $\sigma_{\text{y-combined}}$ is plotted vs. the track angle ϕ. The residuals of the different passes are fitted with the function $\sigma_{\text{y-combined}} = \sqrt{\sigma_{\text{x}}^2 \cdot \tan^2(\phi - \varphi) + \sigma_{\text{y}}^2}$.
An improvement of the resolution after the alignment procedure can be seen for all four super modules. This verifies the success of the alignment. Figure 7.6 depicts the residuals determined from run 1705 of super module VI. It can clearly be seen that both sets of alignment constants improve the resolution. However, determining values for all six alignment constants leads to a better resolution for this run. The same effect, even if less significant, can be seen in Figure 7.7 for run 2222 of super module VII.
Figure 7.8 shows the residuals determined for run 2410 of super module VIII. For pass1, a shift of the minimum of $\sigma_{\text{y-combined}}$ to 1.03° can clearly be seen. For pass2 this shift nearly vanishes. This behavior is best seen in super module VIII, but occurs as well for the super modules VII and IX (see Figure 7.7 and 7.9). This supports the assumption that the shift is an effect of the misalignment of the chambers.

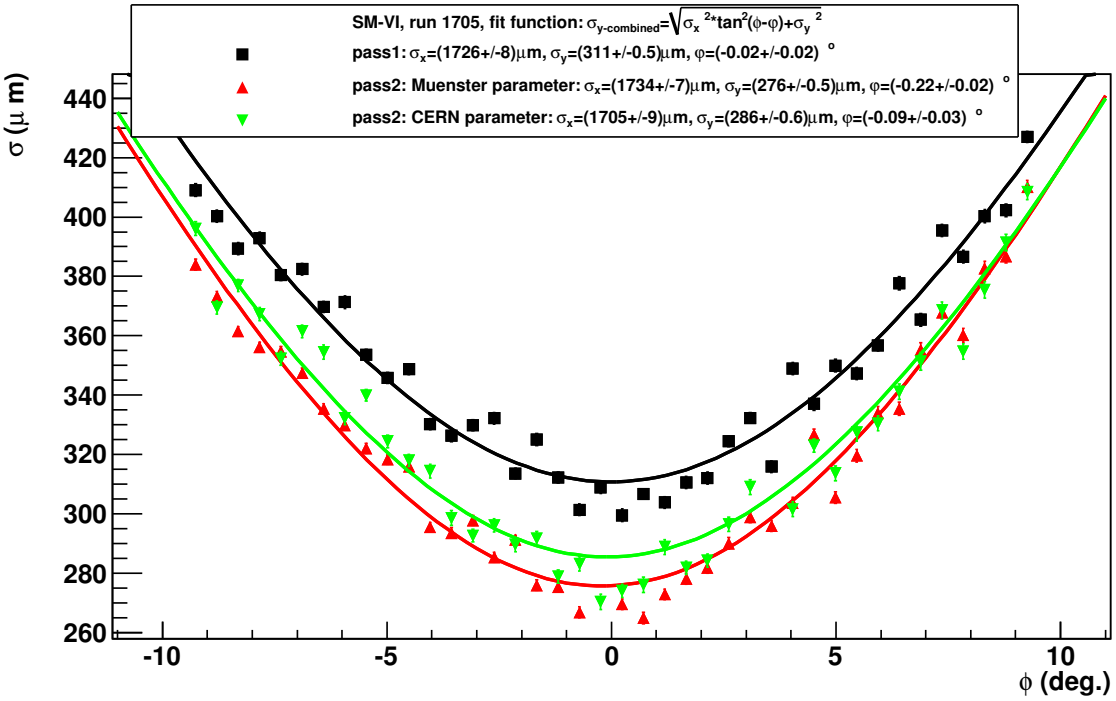

Figure 7.6: *Residuals determined from run 1705 of super module VI before and after the alignment procedure form CERN/MS.*

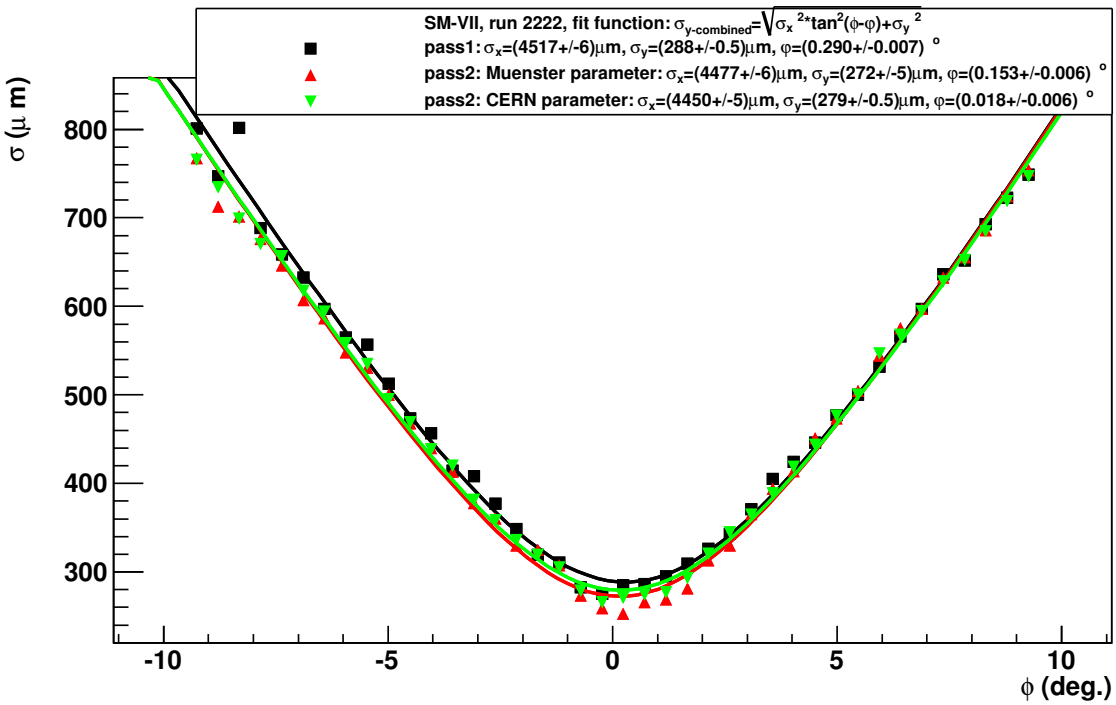

Figure 7.7: *Residuals determined from run 2222 of super module VII before and after the alignment procedure from CERN/MS.*

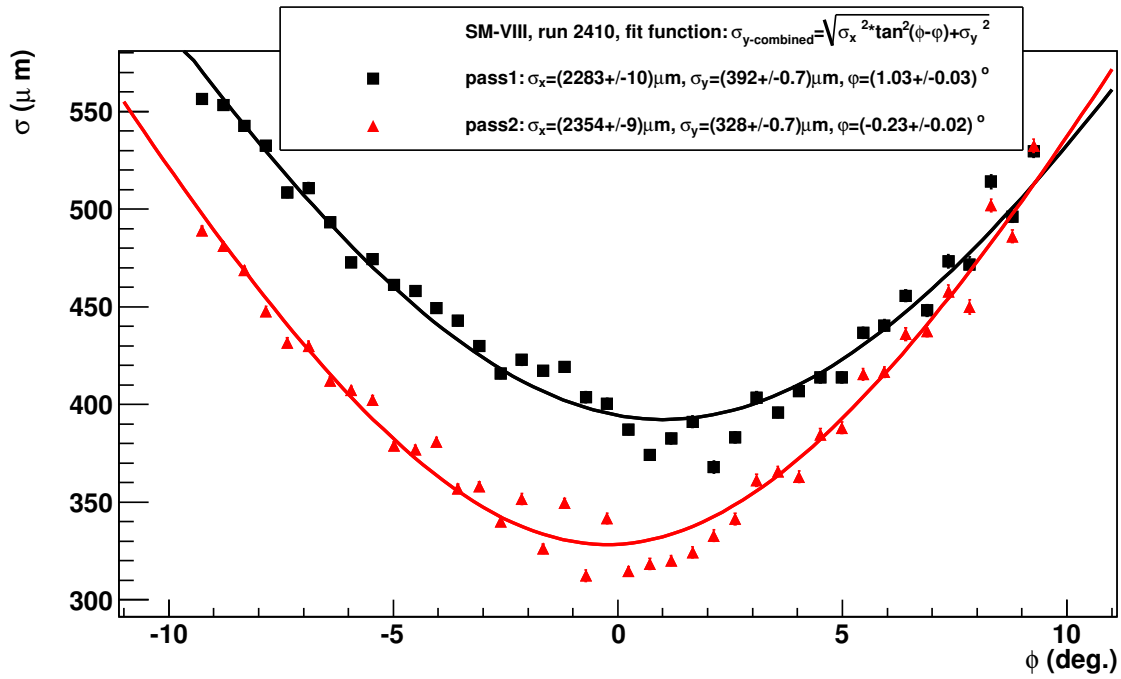

Figure 7.8: *Residuals determined from run 2410 of super module VIII before and after the alignment procedure.*

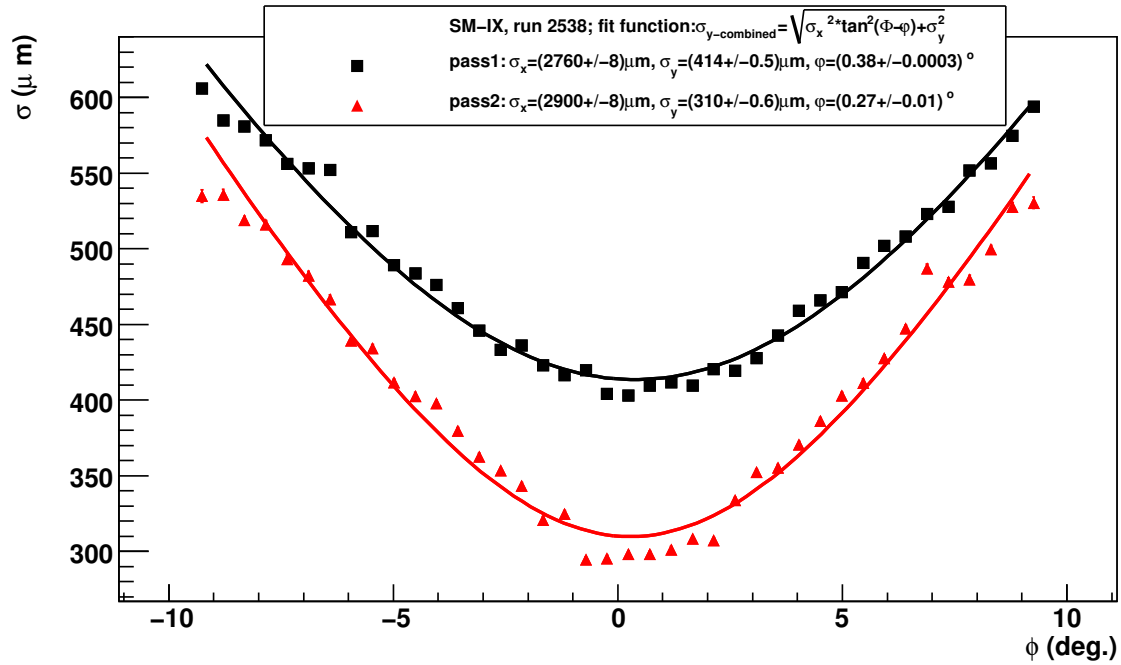

Figure 7.9: *Residuals determined from run 2538 of super module IX before and after the alignment procedure.*

7.3 Results of the Gain Calibration

During the gain calibration, several observations were made. They were most significant for run 1705 of super module VI. Therefore, this run will be used as an example to discuss the results of the gain calibration in the following.

The gain factors are shown for the different layers consecutively from layer 0 to layer 5. Black vertical lines indicate the chamber borders. A setting of $(nz, n\phi\mathrm{r}) = (3, 4)$ was chosen. Thereby, each calibration group comprises two readout pads in row direction and nine readout pads in column direction.
For calibration groups with insufficient statistics, the gain factor cannot be determined. In this case, the default gain of 1 is assumed. This can be seen for example in layer 3 for the columns 0-8 and 134-143 of the rows 0-1.
The shape of the gain profile shows for each chamber a higher gas gain in the chamber middle than on the chamber borders. This can be due to an electrical field that rises towards the center of the chamber, where the field gradient is caused by electrostatic attractions: The positively charged anode wires are drawn towards the grounded pad plane as well as towards the grounded cathode wires. As the pad plane is the most stable element in this ensemble, the anode wire and the cathode wire have the ambition to bend towards the pad plane. This leads to the observed higher gain in the middle of each chamber.
The gain parameters for this run show unexpectedly small values of 0.5 and below. It is not yet verified, if the gas gain was actually this low, or if the values were determined too low systematically. Moreover, the range of the gain factors from 0.5-2.4 in layer 4 stack 3 is overly large and needs further investigation. Such a variation of the gain factors within one chamber should usually only occur for underpressure inside the chamber compared to its surrounding (see Section 3.4.2). However, as the effect occurs only in one chamber and not a whole layer, this cannot be the reason.

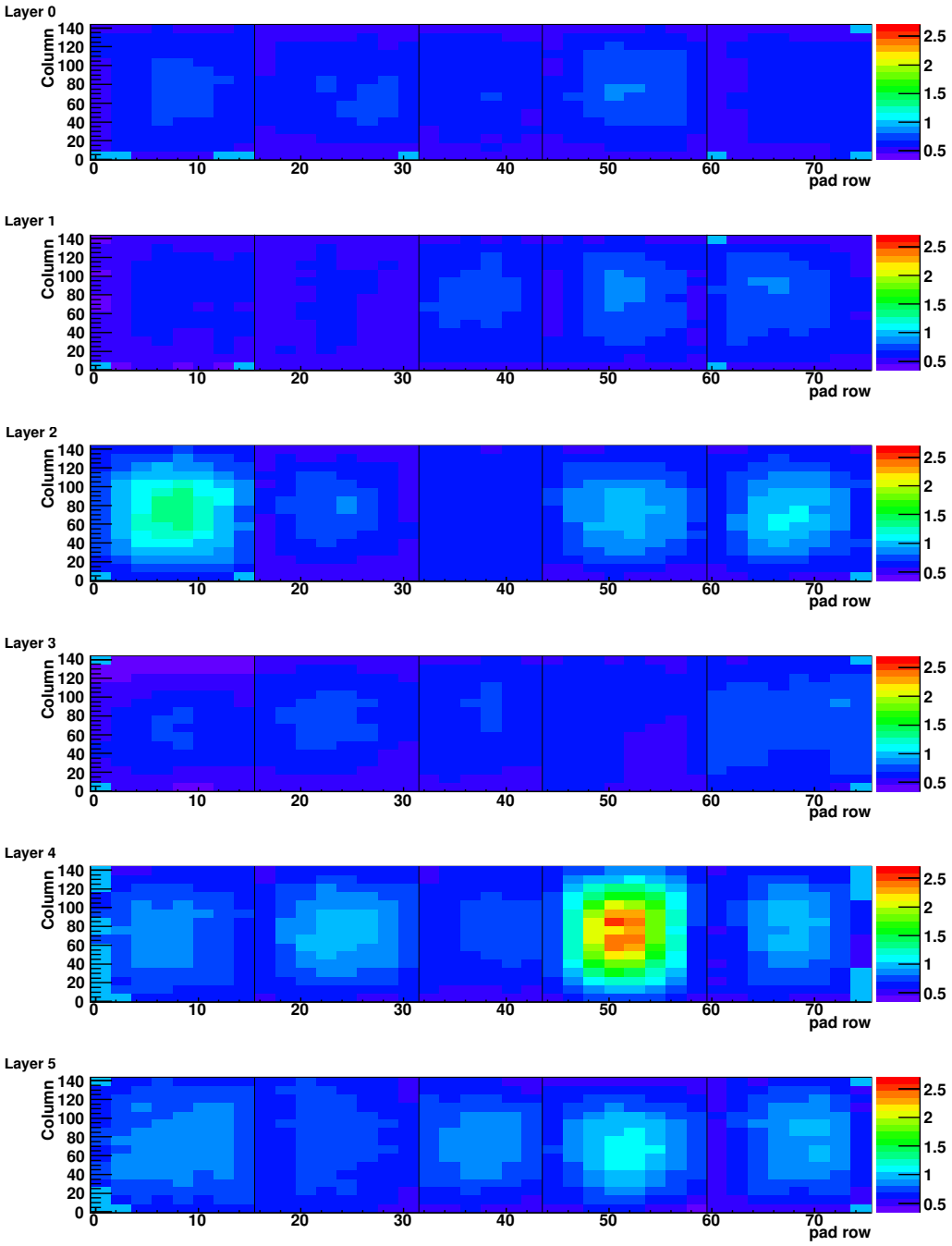

Figure 7.10: *Gain factors determined for run 1705 of super module VI with granularity settings of* $nz, n\phi r = (3, 4)$*, which corresponds to* 2 *rows and* 9 *columns per calibration group.*

8. Summary and Outlook

The main focus of this thesis was the calibration of the Transition Radiation Detector (TRD) of the ALICE experiment at the Large Hadron Collider. ALICE is dedicated to heavy-ion collisions and intends to investigate the quark-gluon phase. The main purpose of the TRD is to provide a fast electron trigger and a good electron pion discrimination. 18 super modules comprise the TRD. Each super module is a gaseous detector, built up of 30 individual detector chambers, which consist of a radiator and a drift region. The final assembly is accomplished at the university of Münster. As part of this procedure, large amounts of data produced by cosmic radiation are recorded. With these data, a first calibration of the detector can be performed.
For particle identification, a precise knowledge of the relative signal amplification, the so-called relative gas gain, is compulsory. The gas gain depends on several criteria, such as the composition of the gas mixture, the applied drift voltage, and temperature and pressure conditions inside the chambers. Therefore, it has to be determined for each set of data individually.
For a good position resolution, a precise knowledge of the drift velocity of the electrons is required. This velocity is sensitive to the same conditions as the gas gain. Hence, it also has to be determined individually for each data set.
Moreover, to achieve a good position resolution, the exact geometry of the detector has to be known. Due to time driven deformations and limited accuracy during assembly, the positions and orientations of the detector chambers do not match the design geometry. These deviations are determined during the alignment procedure.

The calibration of gas gain and drift velocity and the alignment procedure can be performed with software provided by the official AliRoot framework. As part of this thesis, this software was tested and four already assembled super modules were calibrated and aligned.
The effect of an imprecise drift velocity on the resolution was investigated. The expected dependency was confirmed. Moreover, the determined drift velocities were verified by MAGBOLTZ simulations.
The alignment procedure was also performed on those super modules. An improvement of the resolution when applying the determined parameters was seen for all four super modules. Two of these modules are installed at ALICE by now. For those super modules, the deviations of position and orientation determined as part of this thesis were compared to the ones determined from data taken at ALICE. It was found that the resolution is better when the parameters determined with the procedure developed during this thesis

were used, compared to the usage of parameters that were determined with data from ALICE. However, the determined deviations between ideal and real geometry of the super modules were unexpectedly large. This needs to be investigated in more detail in the future.
The performance of the gain calibration was evaluated and the shape of the gain profile meets the expectation. Nevertheless, the gain calibration needs further investigation, since the difference of the gas gain within a readout chamber was in one specific case remarkably high. It is not clear yet, if the determined range of the gas gain reflects the actual gas gain. Moreover, in many cases an unexpectedly low gas gain was determined.

As the main part of this thesis, an overall calibration and alignment procedure was developed and implemented. For the first time, an overall calibration and alignment was performed with data recorded in Münster. This way, the reconstructed data is more accurate, which should lead to an improvement for subsequent analyses.
The implemented procedure can now be used to calibrate and align the remaining nine super modules, which are about to be assembled. Moreover, the determined parameters can be used as a starting point for the calibration and alignment performed at CERN.

Appendix

A. Alignment Constants

A.1 Alignment Constants of Super Module VI

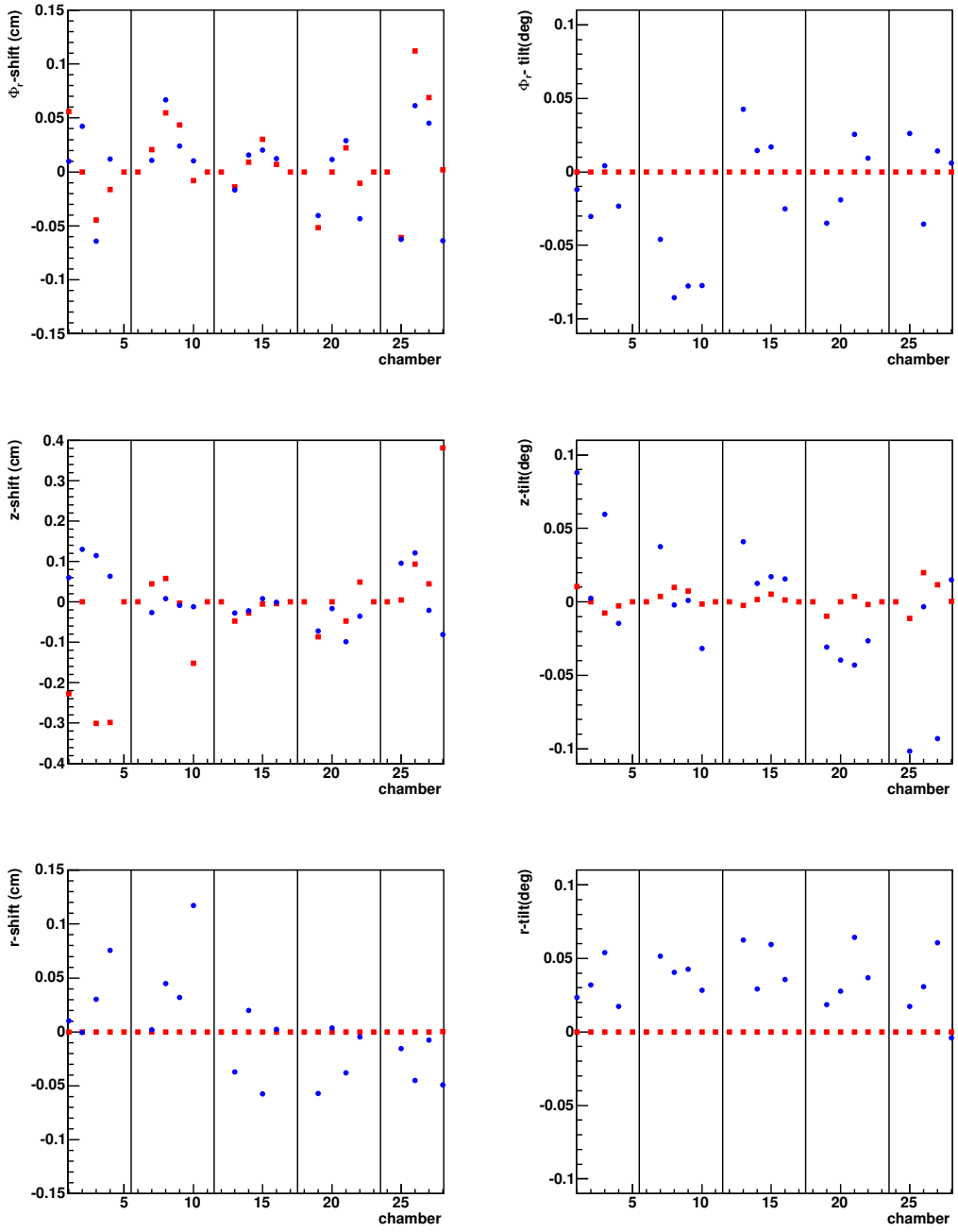

Figure A.1: *Red squares correspond to alignment constants determined with data taken at CERN. Blue dots corresponds to constants determined for super module VI, run 1705.*

A.2 Alignment Constants of Super Module VII

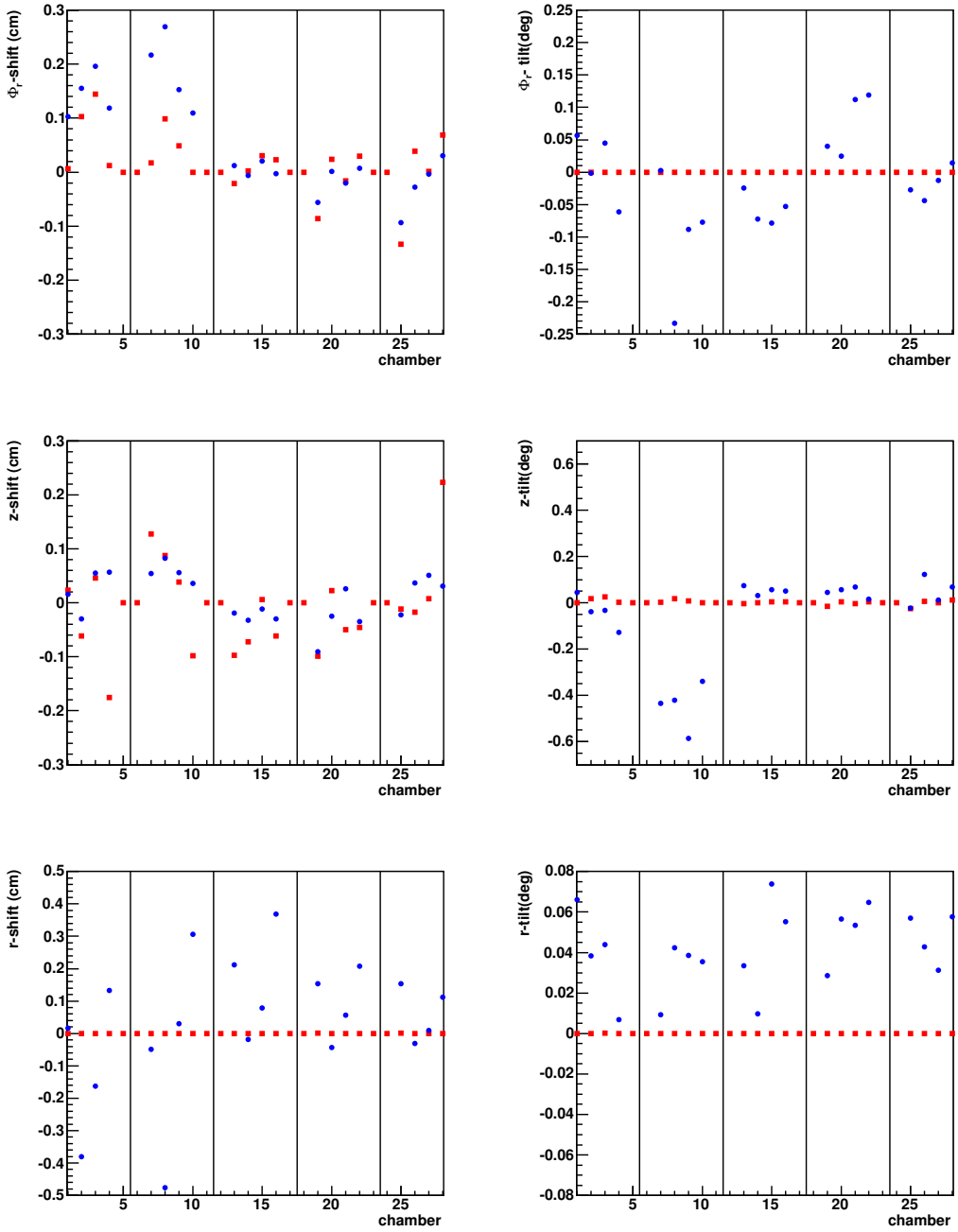

Figure A.2: *Red squares correspond to alignment constants determined with data taken at CERN. Blue dots corresponds to constants determined for super module VII, run 2222.*

A.3 Alignment Constants of Super Module VIII

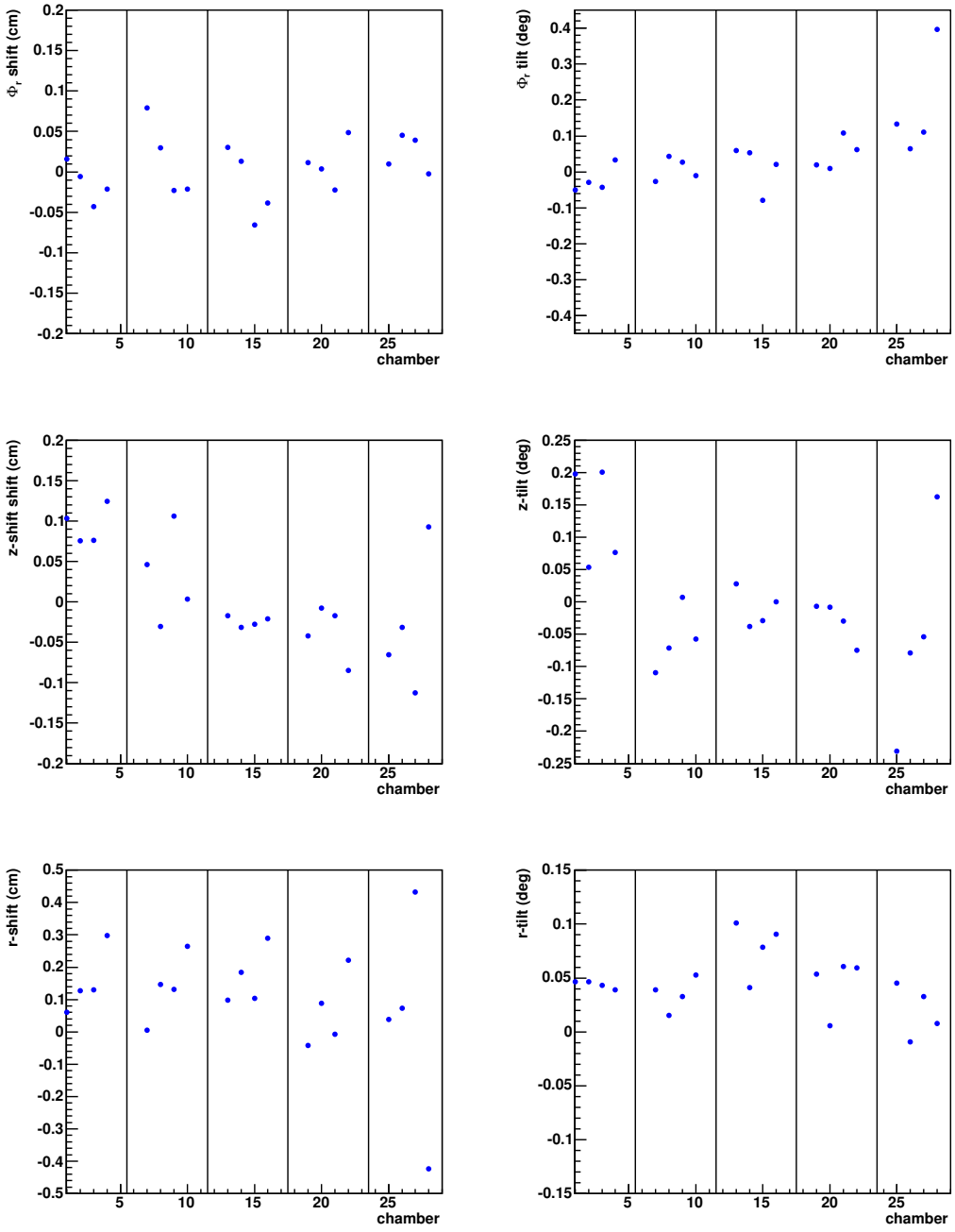

Figure A.3: *Alignment constants determined for super module VIII, run 2410*

A.4 Alignment Constants of Super Module IX

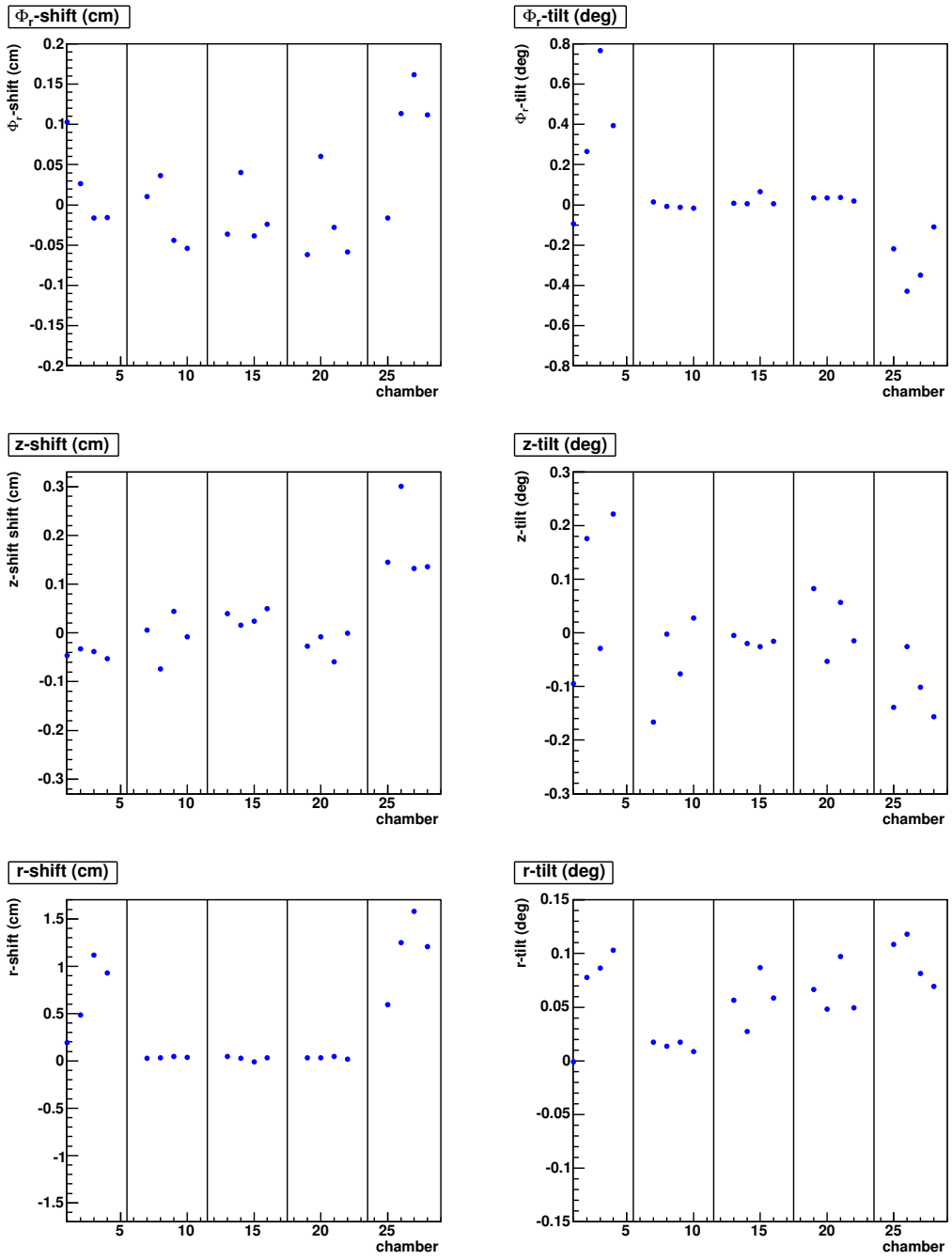

Figure A.4: *Alignment constants determined for super module IX, run 2538*

B. Gain Factors

B.1 Gain Factors of Super Module VI

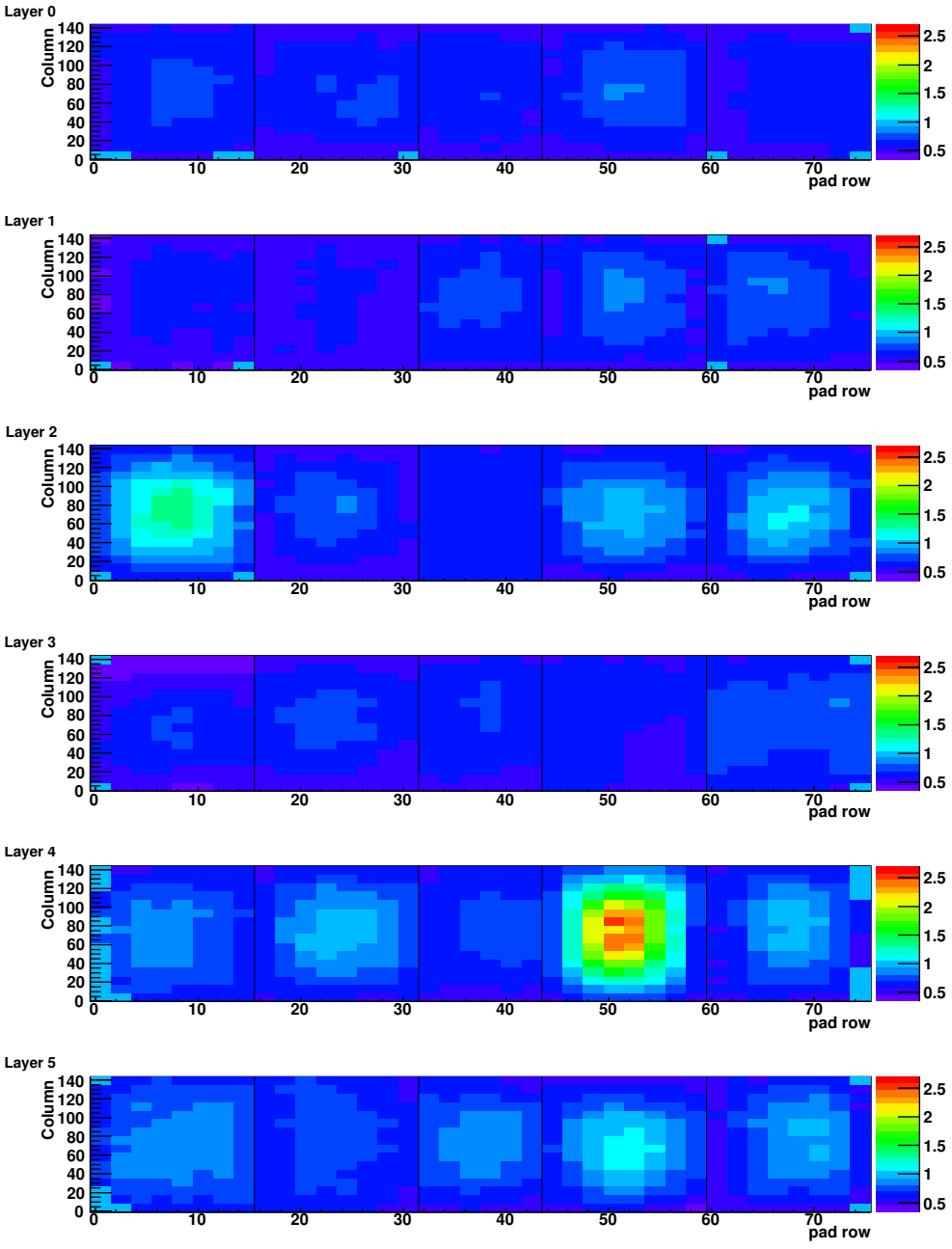

Figure B.1: *Gain factors determined for super module VI, run 1705; granularity settings* $(nz, n\phi r) = (3, 4)$.

B.2 Gain Factors of Super Module VII

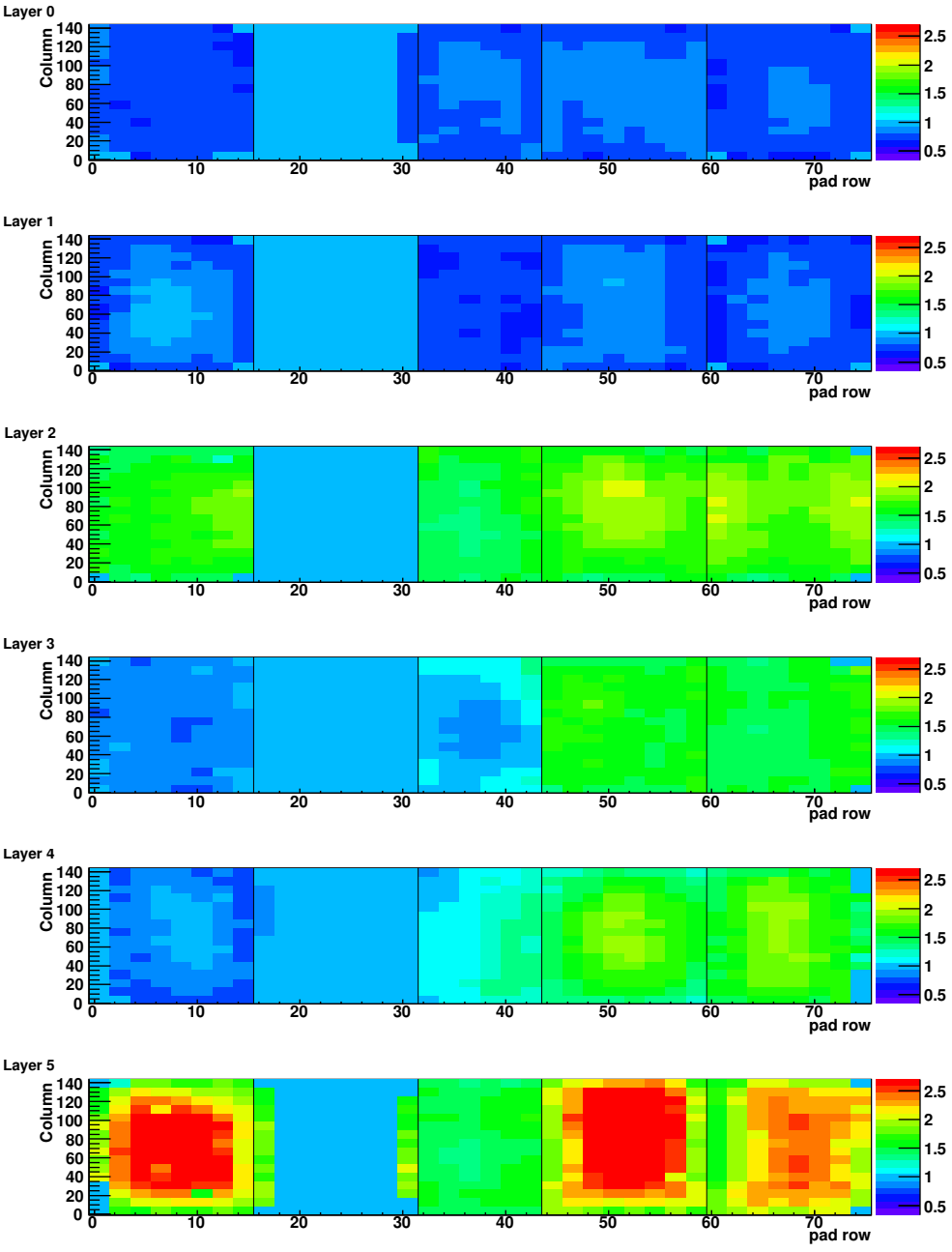

Figure B.2: *Gain factors determined for super module VII, run 2222; granularity settings* $(nz, n\phi r) = (3, 4)$. *For large areas of stack 1 the gain factors could not be determined, therefore the default gain factor of* 1 *is depicted.*

B.3 Gain Factors of Super Module IX

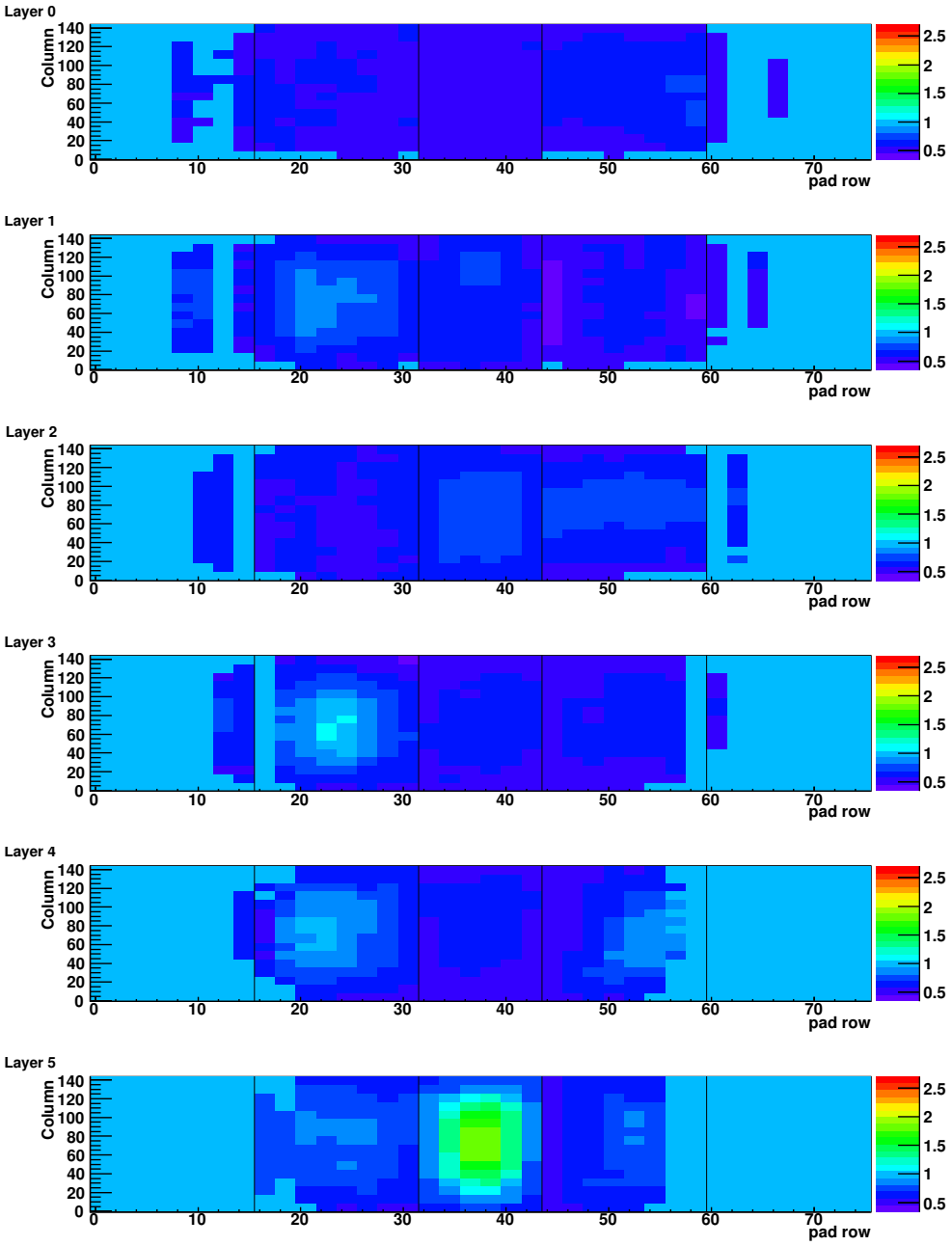

Figure B.3: *Gain factors determined for super module IX, run 253; granularity settings* $(nz, n\phi r) = (3, 4)$. *Trigger mode: coincidence, with upper trigger over stack 2. Light blue areas correspond to the default gain factor value of* 1, *due to insufficient statistics.*

C. Drift Velocity Distribution

C.1 Drift Velocity Distribution of Super Module VI

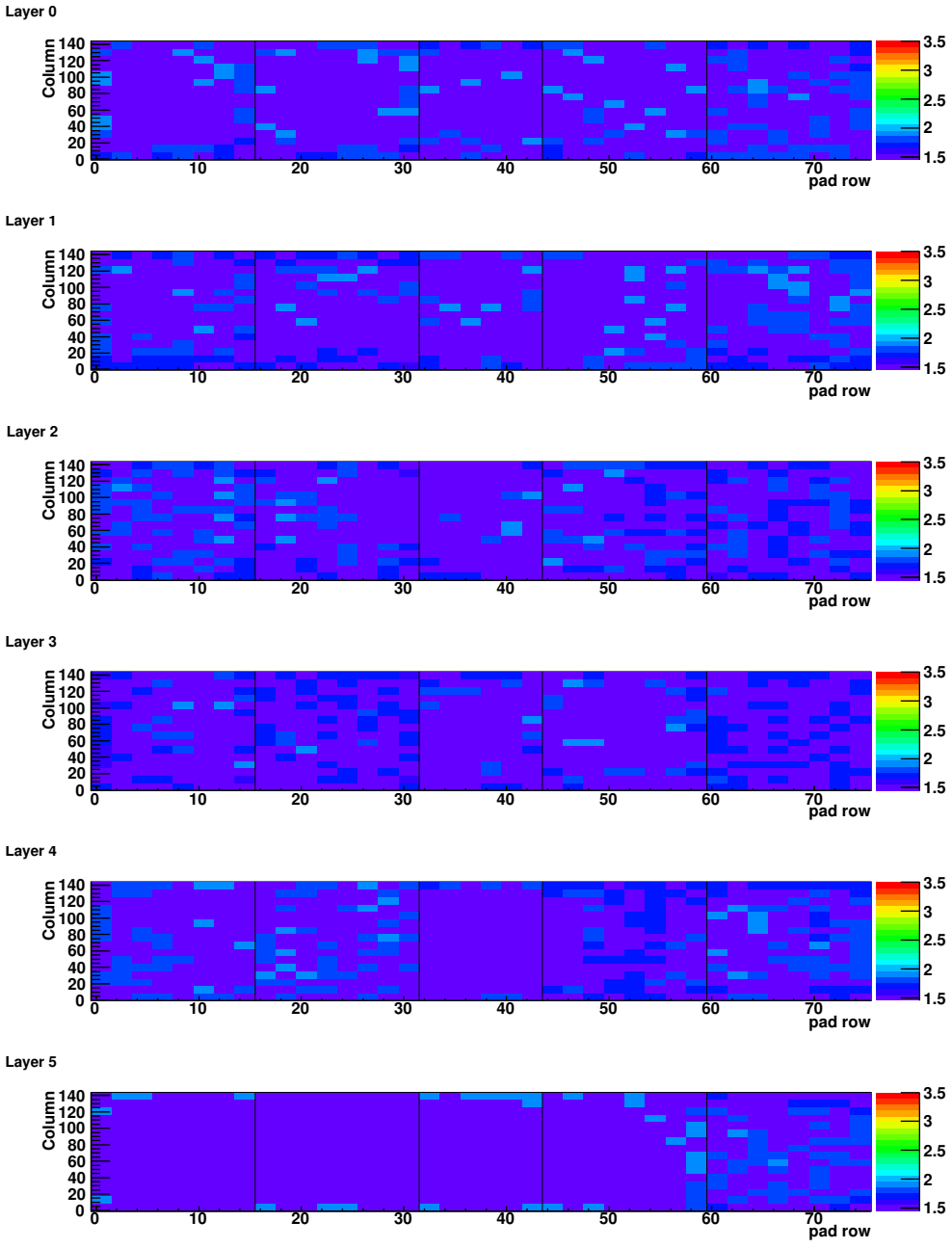

Figure C.1: *Drift velocity distribution determined for super module VI, run 1705; granularity settings* $(nz, n\phi r) = (3, 4)$. *Purple areas correspond to calibration groups with either insufficient statistics, or an unsuccessfully calibration. Therefore, the default drift velocity of* 1.5 $cm/\mu s$ *is presented in these cases.*

C.2 Drift Velocity Distribution of Super Module VII

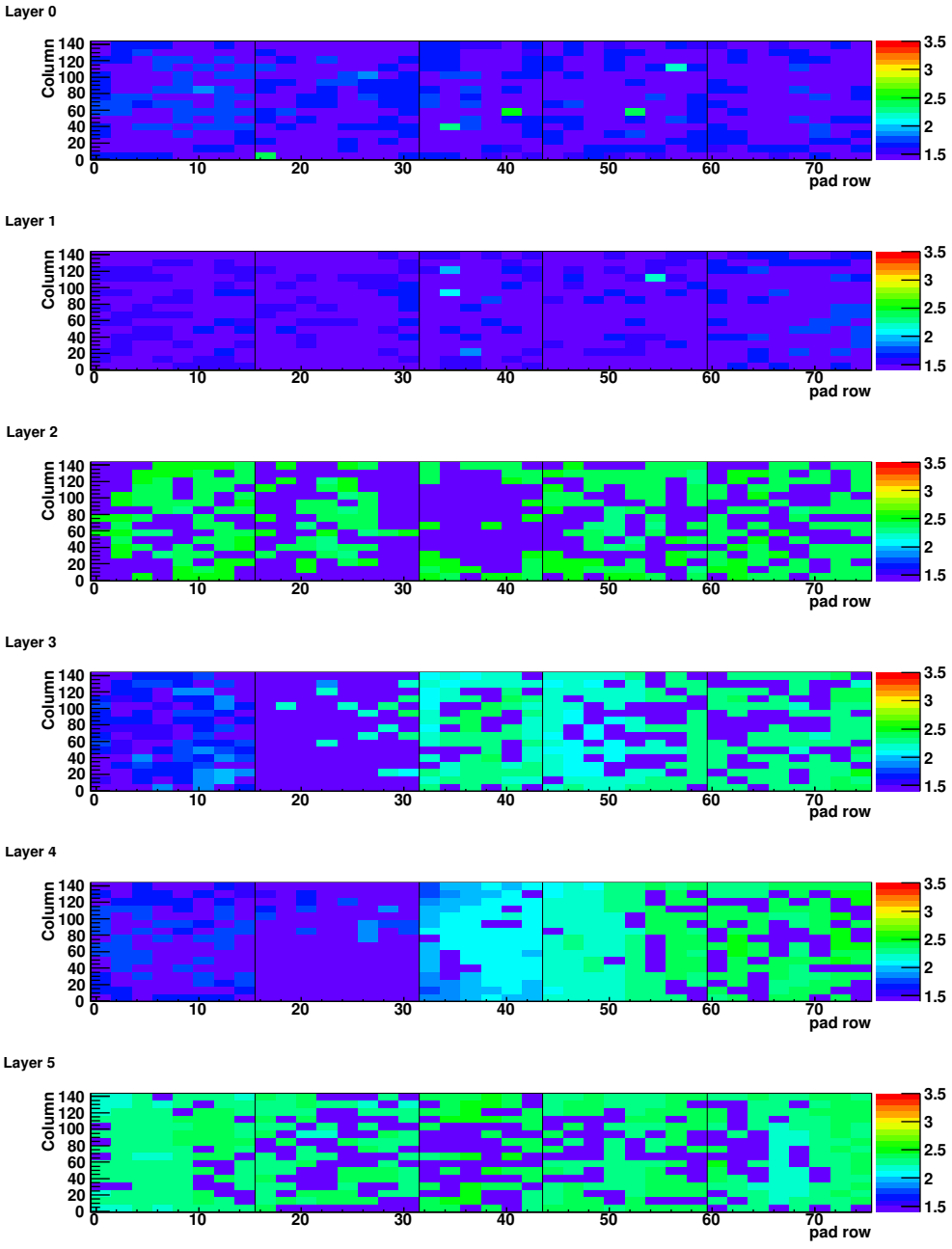

Figure C.2: *Drift velocity distribution determined for super module VII, run 2222; granularity settings* $(nz, n\phi r) = (3, 4)$. *Purple areas correspond to calibration groups with either insufficient statistics, or an unsuccessfully calibration. Therefore, the default drift velocity of* 1.5 $cm/\mu s$ *is presented in these cases.*

C.3 Drift Velocity Distribution of Super Module IX

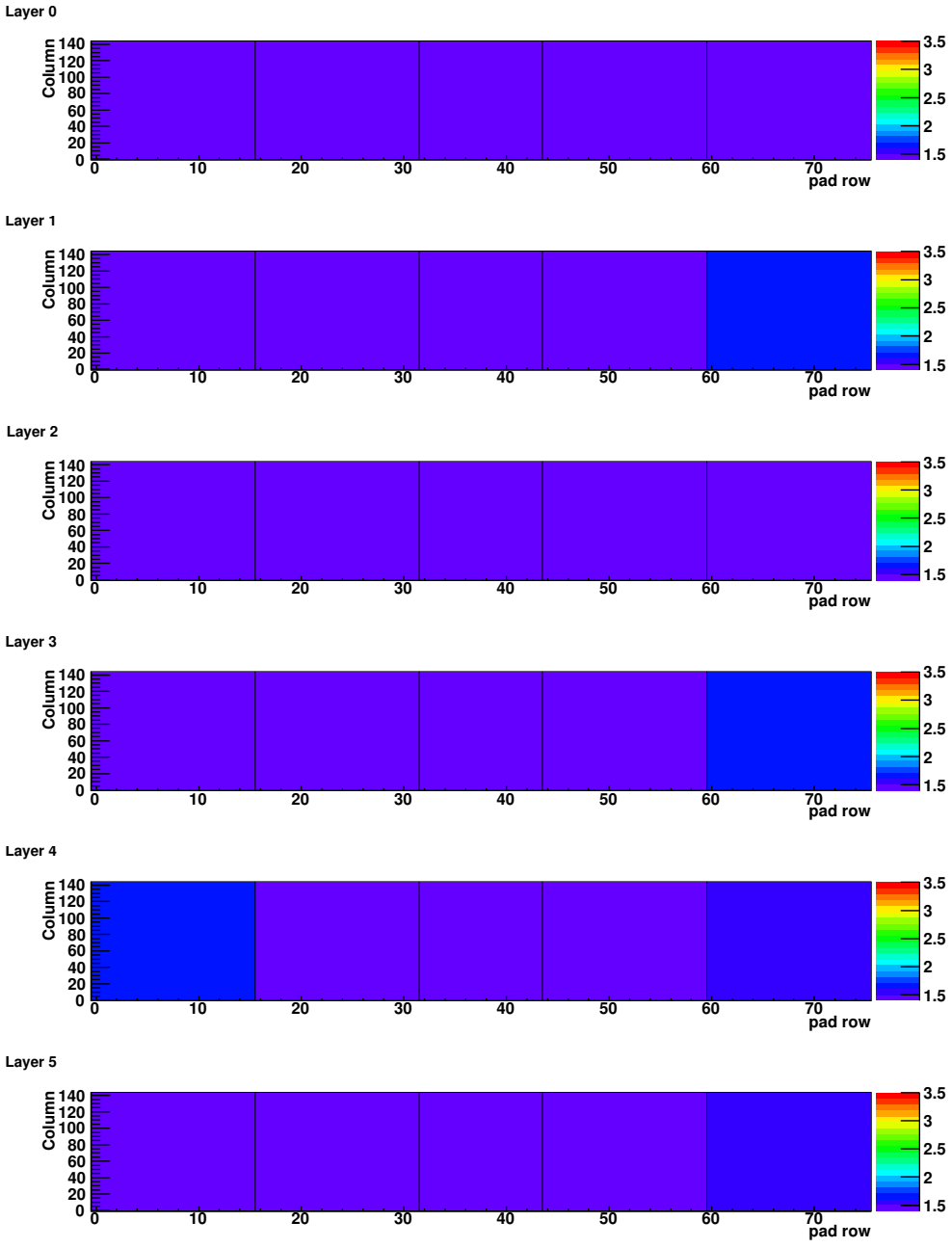

Figure C.3: *Drift velocity distribution determined for super module IX, run 2538; granularity settings* $(nz, n\phi r) = (0, 0)$*. The values of all calibration groups correspond to drift velocities determined during calibration, the default value is not used.*

Bibliography

[A+08] C. Amsler et al. *Physics Letters B*, (667), 2008.

[A+09] C. Amstel et al. *Particle Physics Booklet*, 1 2009.

[Alb10] Björn Albrecht. Gain Calibration of ALICE TRD Modules Using Cosmic Ray Data. Diploma thesis, *Westfälische Wilhelms-Universität Münster*, February 2010.

[ALI01] Collaboration ALICE. *ALICE - Technical Design Report of the Transition Radiation Detector*. CERN, October 2001.

[ALI04] Collaboration ALICE. *ALICE: Physics Performance Report Vol. I + II*. 2004.

[ALI06] Collaboration ALICE. *ALICE, The Electromagnetic Calorimeter - technical proposal*. CERN, April 2006.

[ALI08a] Collaboration ALICE. The ALICE experiment at the CERN LHC. *Journal of Instrumentation*, 2008.

[ALI08b] Collaboration ALICE. *ALICE Technical Paper*. 1, CERN. 2008.

[Ali10a] ALICE Offline Pages. http://aliweb.cern.ch/Offline/, June 2010.

[Ali10b] AliEn. http://alien2.cern.ch/, June 2010.

[And] A. Andronic. Transition Radiation Detector study. *Gesellschaft für Schwerionenforschung*, Darmstadt.

[Bai08] Raphaëlle Bailhache. Calibration of the ALICE Transition Radiation Detector and a study of Z^0 and heavy quark production in pp collisions at the LHC. PhD thesis, *Technische Universität Darmstadt*, December 2008.

[Bat07] Bastian Bathen. Aufbau eines Triggers für Tests der ALICE TRD Supermodule mit kosmischer Strahlung. Diploma thesis, *Westfälische-Wilhelms-Universität Münster*, 2007.

[BC03] L. Betev and P. Chochula. Definition of the alice coordinate system and basic rules for sub-detector components numbering. *ALICE-INT-2003-038*, June 2003.

[BMS07] Peter Braun-Munziger and Johanna Stachel. The quest for the quark-gluon plasma. *NATURE*, 448, July 2007.

[CER08] CERN. *LHC the guide*. 2008.

[CER09] CERN. *press information*. http://press.web.cern.ch, 2009.

[CER10] CERN. *ALICE wiki EMCAL*. May 2010.

[Dav06] Yu. I. Davydov. On the first Townsend coefficient at high electric field. *IEEE Transactions on Nuclear Science*, September 2006.

[d'E09] David d'Enterria. Jet quenching in QCD matter: from RHIC to LHC. *Nuclear Physics*, 2009.

[Dem06] Wolfgang Demtröder. *Experimentalphysik 1, Mechanik und Wärme*. Springer-Lehrbuch, 4 edition, 2006.

[Ems10] David Emschermann. Construction and performance of the alice transition radiation detector. PhD thesis, *The Combined Faculties for Natural Science and for Mathematics of the Ruperto-Carola Universität of Heidelberg*, 2010.

[ESA00] V. Egorytchev, V. Saveliev, and S.J. Aplin. Particle identification via transition radiation and detectors. *Nuclear Instruments and Methods in Physics Research*, A 453, June 2000.

[FK04] Z. Fodor and S. D. Katz. Critical point of QCD at finite T and μ, lattice results for physical quark masses. *Journal of High Energy Physics*, February 2004.

[Gre66] Kenneth Greisen. End to the Cosmic-Ray Spectrum? *PHYSICAL REVIEW LETTERS*, 16(17):748–750, April 1966.

[Gri09] Helge Grimm. Entwicklung eines Gassystems zur Ansteuerung, Überwachung und Qualitätskontrolle eine ALICE TRD Supermodules. Diploma theiss, *Westfälische Wilhelms-Universität Münster*, 2009.

[His06] P. Histrov. *AliRoot Primer*. www.aliweb.cern.ch/secure/Offline/sites/aliweb.cern.ch.Offline /files/uploads/ OfflineBible.pdf, April 2006.

[Hop04] Melanie Hoppe. Aufbau und Inbetriebnahme einer Funkenkammer. Diploma thesis, *Westfälische Wilhelms-Universität Münster*, 2004.

[KB04] C. Klein-Bösing. Production of Neutral Pions and Direct Photons in Ultra-Relativistic Au+Au collisions. PhD thesis, *Westfälische Willhelms-Universität Münster*, 2004.

[Lac09] R. Lacey. Collective phenomena in Heavy Ion Collisions. Lecture notes, *Jyväskylä Summer School*, https://trac.cc.jyu.fi/projects/alice/wiki/lectures/Roy09, August 2009.

[MP90] S. Meyers and E. Picasso. The design, construction and commissioning of the CERN large Electron-Positron collider. *Contemporary Physics*, 31(6), November 1990.

[myS10] MySQL Query Analyzer - Improving SQL Query Performance. http://www.mysql.com, June 2010.

[OCD10] The Offline Conditions DB framework | ALICE offline pages. http://aliweb.cern.ch/Offline/Activities/ConditionDB.html, June 2010.

[pad09] http://www.physi.uni-heidelberg.de/galerie/allpics.php, 2009.

[Per00] D. H. Perkins. *Introduction to High Energy Physics*. Cambridge University Press, 2000.

[Pop] Friederike Poppenborg. Diploma thesis, *Westfälische Wilhelms-Universität Münster*.

[PRSZ04] B. Povh, K. Rith, C. Scholz, and F. Zetsche. *Teilchen und Kerne*. Springer-Verlag Berlin Heidelberg, 2004.

[rhi09] RHIC | Relativistic Heavy Ion Collider. http://www.bnl.gov/rhic/, September 2009.

[roo10] ROOT | A Data Analysis Framework. http://root.cern.ch/drupal/, June 2010.

[Sau77] F. Sauli. Principles of Operation of Multiwire Proportional and Drift Chambers. Lecture notes, *Academic Training Program of CERN 1975-1976*, 1977.

[sec10] http://alice.uni-hd.de/muenster/more/TRDsequencev05.ppt, June 2010.

[Sic09] Eva Sicking. Alignment of ALICE TRD Modules Using Cosmic Ray Data. Diploma thesis, *Westfälische Wilhelms-Universität Münster* , February 2009.

[SPR90] B. Sinha, S. Pal, and S. Raha. Quark-gluon plasma. *Research Reports in Physics*, Springer-Verlag, 1990.

[Tan09] Michael J. Tannenbaum. High-p_T from ISR to RHIC/LHC. Lecture notes, *Jyväskylä Summer School*, https://trac.cc.jyu.fi/projects/alice/wiki/lectures/Roy09, August 2009.

[TGe10] TGeoManager. http://root.cern.ch/root/html/TGeoManager.html, June 2010.

[ttr10] TTree. http://root.cern.ch/root/html/TTree.html, August 2010.

[van09] Dr. Marco van Leeuwen. Direct photon and jet physics. Lecture notes, *Jyväskylä Summer School*, https://trac.cc.jyu.fi/projects/alice/wiki/lectures/mvl09, August 2009.

[Wal10] Matthias Walter. Performance of Online Tracklet Reconstruction with the ALICE TRD. Diploma thesis, *Westfälische Wilhelms-Universität Münster*, February 2010.

[Wes09] Uwe Westerhoff. The FEE Server Control Engine of the ALICE-TRD. Diploma thesis, *Westfälische Wilhelms-Universität Münster*, January 2009.

[Wil10] Alexander Wilk. Particle Identification Using Artificial Neural Networks with the ALICE Transition Radiation Detector. PhD thesis, *Westfälische Wilhelms-Universität Münster*, April 2010.

[Wul09] Elke Svenja Wulff. Position Resolution and Zero Suppression of the ALICE TRD. Diploma thesis, *Westfälische Wilhelms-Universität Münster*, February 2009.

[WW07] C. Weinheimer and J. P. Wessels. Kern und Teilchenphysik II. Lecture notes, *Westfälische Wilhelms-Universität Münster*, 2007.

Danksagung

Abschließend möchte ich mich bei allen bedanken, die zum Gelingen dieser Arbeit beigetragen haben.

Allen voran gilt mein Dank Prof. Dr. Johannes P. Wessels für die Aufnahme in die Arbeitsgruppe, die interessante Themenstellung meiner Diplomarbeit und die Ermöglichung lehrreicher Aufenthalte am CERN, der GSI und der University of Jyväskylä, sowie der Teilnahme an der DPG-Tagung 2010.
Für die Übernahme des Korreferats danke ich Prof. Dr. Christian Weinheimer.

Mein ausgesprochener Dank gilt Dr. Tom Dietel für die Betreuung meiner Arbeit, zahlreiche Anregungen und die Beantwortung vieler Fragen.

Des weiteren möchte ich Dr. Matus Kallisky danken, der mir mit Rat und Tat bei vielen AliRoot bezogenen Problemen zur Seite stand.
Für die stete Unterstützung bei Alignment-Fragen und -Problemen danke ich Dr. Dariusz Miskowiec und Eva Sicking. Für den regen Informationsaustausch und die Beantwortung vieler Fragen in Bezug auf die Gain- und Driftgeschwindigkeits-Kalibration danke ich Dr. Raphaëlle Bailhache und Björn Albrecht.
Friederike Poppenborg danke ich für die Unterstützung bezüglich der Simulationen.
Für die kritische Durchsicht der Arbeit und für stilistische Anregungen möchte ich mich bei Dr. Tom Dietel, Dr. Matus Kalisky, Dr. Christian Klein-Bösing, Dr. David Emschermann, Dr. Alexander Wilk, Dr. Baldo Salmüller, Matthias Walter, Eva Sicking, Svea Sauer, Ulrike Drevenstedt, Sebastian Klamor, Björn Albrecht, Norina Richter, Helene Gossen, Sebastian Kosmeier, Falko Brinkmann, Christian Schmeltzer und Lynsey und Cynthia bedanken.
Björn Albrecht und Matthias Walter danke ich für die tolle Zeit im gemütlichen Reinraum-Büro. Mit euch Beiden macht selbst der Montagmorgen Spaß!
Für ein gutes Laborklima beim Supermodulbaue danke ich Björn Albrecht, Jonas Anielski, Helmut Baumeister, Bastian Bathen, Ingo Burmeister, Dr. Thomas Dietel, Helge Grimm, Georg Hackmann, Markus Heide, Norbert Heine, Dr. Matus Kalisky, Friederike

Poppenborg, Markus Rammler, Eva Sicking, Markus Tegeder, Wolfgang Verhoeven, Matthias Walter, Uwe Westerhoff, Martin Wilde und Svenja Wulff.
Des weiteren möchte ich der gesamten Arbeitsgruppe für die angenehme Atmosphäre danken.
Außerdem möchte ich sämtlichen Freunden und Mitbewohnern die mich in dieser Zeit begleitet und unterstützt haben von Herzen Danken.

Zuletzt möchte ich mich besonders bei meiner Familie bedanken, die mich sowohl moralisch, als auch mit dem einen oder anderen Euro unterstützt und mir somit das Studium ermöglicht hat. Danke!

Eigenständigkeitserklärung

Ich versichere, diese Arbeit selbständig verfasst und keine anderen als die angegebenen Hilfsmittel und Quellen benutzt zu haben.

Münster, 03. September 2010

Henriette Gatz